# 1. Leg 180 Summary: Active Continental Extension in the Western Woodlark Basin, Papua New Guinea[1]

Shipboard Scientific Party[2]

INTRODUCTION

The continuum of active extensional processes, laterally varying from continental rifting to seafloor spreading, in the western Woodlark Basin–Papuan Peninsula region of Papua New Guinea (Fig. F1) provides the opportunity to investigate the mechanics of lithospheric extension and continental breakup. Seafloor spreading magnetic anomalies indicate that during the last 6 m.y. the formerly contiguous, eastward extensions of the Papuan Peninsula (the Woodlark and Pocklington Rises) were separated as a westward propagating spreading center opened the Woodlark Basin (Weissel et al., 1982; Taylor et al., 1995, in press; Goodliffe et al., 1997; Goodliffe, 1998). The present spreading tip is at 9.8°S, 151.7°E. Farther west, extension is accommodated by continental rifting, with associated full and half graben, metamorphic core complexes, and peralkaline rhyolitic volcanism (Smith and Simpson, 1972; Smith, 1976; Davies, 1980; Hegner and Smith, 1992; Davies and Warren, 1992; Hill et al., 1992, 1995; Baldwin et al., 1993; Hill and Baldwin, 1993; Stolz et al., 1993; Lister and Baldwin, 1993; Hill, 1994). Current rifting and spreading are confirmed by kinematic measurements using Global Positioning System (GPS) observations (Tregoning et al., 1998). Earthquake source parameters and seismic reflection data indicate that normal faulting is active at depths above 9 km in the region of incipient continental separation (Figs. F2, F3, F4, F5, F6; Abers, 1991; Taylor et al., 1995, 1996, in press; Mutter et al., 1996; Abers, 1997). A low-angle normal fault emerges along the northern flank of Moresby Seamount, a continental crustal block with greenschist metamorphic basement. Asymmetric basement fault blocks overlain by only minor
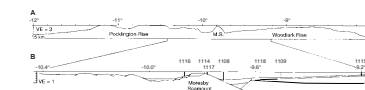
F1. Physiographic features and plate boundaries of Woodlark Basin region, **p. 32**.
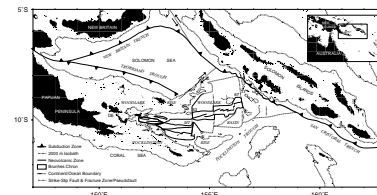
F2. Papuan Peninsula topography and western Woodlark Basin bathymetry showing relocated epicenters and earthquake focal mechanisms (Abers et al., 1997), **p. 33**.
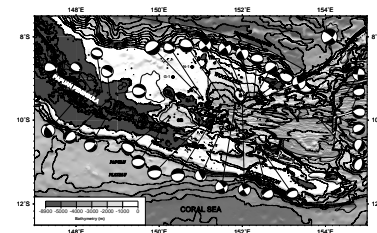
F3. Nested meridional cross sections at 151°34.5′E, **p. 34**.

F4. Depth sections of seismic lines on which Sites 1108, 1112, and 1113 were drilled in the rift basin north of Moresby Seamount, **p. 35**.
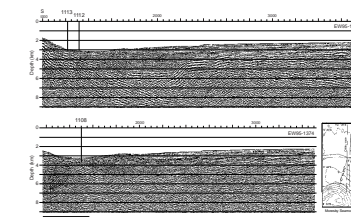
ponded sediments characterize the margin to the south, whereas the margin to the north has a down-flexed prerift sedimentary basin and basement sequence unconformably beneath synrift sediments (Figs. **F3, F4, F5**).

The primary objectives of Ocean Drilling Program (ODP) Leg 180 were to (1) characterize the composition and in situ properties (stress, permeability, temperature, pressure, physical properties, and fluid pressure) of an active low-angle normal fault zone to understand how such faults slip, (2) determine the sedimentology, magnetobiostratigraphy, physical properties, and vertical motion history of the northern margin, including the nature of the forearc basin (and basement?) sequence and hence the prerift history, and (3) determine the internal structure and composition of Moresby Seamount, including the nature of basement (rock type, P-T-t, structural fabric, and deformation history). These parameters will be used as input into regional models for the extensional deformation of continental lithosphere, particularly the mode, timing, and amount of extension prior to spreading initiation.
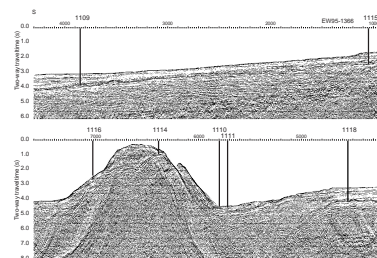
DRILL SITES

During Leg 180 we drilled a transect of sites just ahead of the spreading tip: Sites 1109, 1115, and 1118 on the down-flexed northern margin; Sites 1108 and 1110–1113 into the rift basin sediments above the low-angle normal fault zone; and Sites 1114, 1116, and 1117 on the footwall fault block, Moresby Seamount—Site 1114 near the crest, 1116 on the southern flank, and 1117 into the upper fault face (Figs. **F3, F4, F5, F6, F7, F8;** Table **T1**).

The drill sites are located within a grid of multichannel seismic (MCS) lines and multibeam bathymetry (Figs. **F7, F8**). The northern margin sites (1109, 1115, and 1118), cored to 802, 803, and 927 meters below seafloor (mbsf), respectively, penetrated the synrift latest Miocene–Pleistocene cover sequence and into prerift sections: dolerites at Sites 1109 and 1118, and Miocene forearc clastics at Site 1115. Penetration into greenschist metadolerite beneath the 286-m-thick Pliocene–Pleistocene section and 6-m-thick fault breccia at Site 1114 extended to 407 mbsf. Basement was not reached beneath the 159 m of coarse rift clastics at Site 1116. The planned triple casing reentry hole at Site 1108 was aborted because of hydrocarbon concerns after drilling Hole 1108B to 485 mbsf. The presence of higher molecular-weight hydrocarbons at depth (Site 1108), and the extent of talus proximal to Moresby Seamount where the fault is shallow (Sites 1110–1113, which penetrated 25–174 mbsf), precluded use of the available technology to meet our primary objective. At Site 1117, however, the ~100-m-thick fault zone of gouge, mylonite, and breccia was cored into undeformed gabbro. Sites 1109, 1114, 1115, and 1118 were all logged with triple combo geophysics and Formation MicroScanner (FMS) sonic tool strings, and vertical seismic profiles were obtained at Sites 1118 (complete), 1109 and 1115 (partial), making this one of the most successful ODP logging legs to date.

The primary results are presented first by site and then by theme. In the following section, the site summaries are arranged in geographic order, progressing from north to south along the transect.

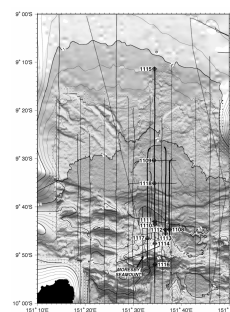F5. Time section of seismic line on which Sites 1109–1111, 1114–1116, and 1118 were drilled, **p. 37**.
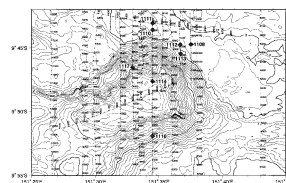

F6. Time section of seismic line on which Site 1117 was drilled, **p. 38**.
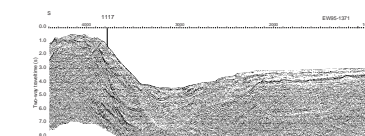
F7. Locations of Leg 180 drill sites and seismic tracks, **p. 39**.

F8. Bathymetric map showing locations of Leg 180 drill sites near Moresby Seamount, **p. 40**.

T1. Leg 180 drill-site locations and coring totals, **p. 75**.

SITE SUMMARIES

Site 1115

Hole 1115A (APC [advanced hydraulic piston corer]):
　　9°11.389′S, 151°34.450′E; 1149.6 mbsl (meters below sea level)
　　0–4.40 mbsf cored; 4.43 m recovered (101%)
Hole 1115B (APC/XCB [extended core barrel]):
　　9°11.382′S, 151°34.437′E; 1148.8 mbsl
　　0–293.10 mbsf cored; 286.84 m recovered (98%)
Hole 1115C (RCB [rotary core barrel]):
　　9°11.383′S, 151°34.422′E; 1148.7 mbsl
　　0–283.5 mbsf drilled without coring; 283.2–802.5 mbsf cored;
　　291.63 m recovered (56%)

The objectives of our study at Site 1115 were to determine the sedimentology, biostratigraphy, and vertical motion history of the Woodlark Rise (the northern, upper plate margin to the Moresby detachment fault), including the prerift history of the Trobriand forearc basin sequence. The site was located ~35 km to the north of Site 1109 (Figs. **F5, F7**) to (1) better characterize the slope sediments and provide widely spaced data from shallower water depths for flexural subsidence models, (2) avoid the thick dolerite that prevented sampling of the prerift forearc sequence at Site 1109, and (3) sample the upper ~150 m of section that has been eroded by a submarine channel further south.

From bottom to top, the sedimentary succession cored at Site 1115 (Figs. **F9, F10**) shows (1) a shoaling and coarsening upward, middle Miocene forearc sequence, unconformably below (2) a late Miocene nonmarine coastal (fluvial?) and lagoonal succession, and (3) a shallow marine, then progressively deepening and fining upward, latest Miocene (5.54 Ma) to Pleistocene sequence related to the subsidence of the margin during the rifting of the Woodlark Basin. The synrift sequence is undeformed, with bedding dips <10° throughout, whereas the forearc sequence below exhibits a few normal, reverse, and strike-slip faults.

We cored the upper ~230 m of the >2-km-thick Trobriand forearc basin sequence. This section was deposited at >135 m/m.y. and is older than 12.1 Ma and younger than 15.1 Ma. The sequence comprises turbiditic sands, silts, and clays derived from calc-alkaline arc sources including distinctive clinopyroxene-phyric basic extrusives. The turbidites below 615 mbsf were deposited in upper bathyal depths (150–500 m). The turbidites above 659 mbsf were joined by redeposited neritic carbonates and deposits marked by sediment instability, possibly related to local channeling and/or regional tectonism. Benthic foraminifers indicate a change to neritic deposition (50–150 m) above 615 mbsf and by 13.6 Ma. The sediments record substantial input of shallow-water carbonate. The upward shallowing of the forearc sequence may be attributed to both filling of the basin and tectonic uplift.

An unconformity and hiatus at 574 mbsf resulted from the emergence of the forearc sequence. The unconformity is seismically imaged throughout the Trobriand forearc basin and is younger than 9.63 Ma at the Nubiam-1 well ~100 km to the northwest. At Site 1115, the unconformity is older than 5.54 Ma, by which time sediments younger than 8.6 Ma had accumulated to 513 mbsf at rates >13 m/m.y. The basal sediments above the unconformity are nonmarine (fluvial?) conglomerate (to 566 mbsf), topped by an organic-rich silty claystone (inner

F9. Lithostratigraphy and correlation of Sites 1108, 1109, 1115, and 1118, **p. 41**.
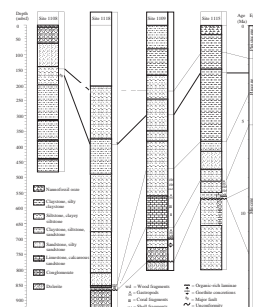
F10. Sedimentation curves based on nannofossil and foraminifer datum events, chron and subchron boundaries, and lithostratigraphic correlations, **p. 42**.
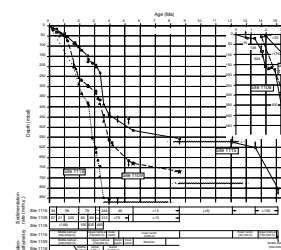
lagoonal), and capped by a siltstone with common to abundant shell fragments (open-marine lagoonal).

Margin subsidence is recorded by inner neritic (<50 m) sandy siltstone (to 475 mbsf) passing upward to silty sandstone (to 417 mbsf) deposited on an open shelf (50–150 m) influenced by traction currents. Sedimentation rates from 4.0–5.5 Ma averaged 45 m/m.y.

From 4.0 to 3.0 Ma, the average sediment accumulation dramatically increased to ~284 m/m.y. This resulted in undercompaction and anomalously high measured porosities between ~420 and ~300 mbsf (Fig. **F11**). Above 417 mbsf, turbidites were deposited in deeper water, upper bathyal (150–500 m), and they fine upward from sandy silty claystone to silty claystone. Volcaniclastic sand and silt horizons, originating from a calc-alkaline arc source, remain little changed throughout the Pliocene section. The pelagic carbonate component increases above 300 mbsf with $CaCO_3$ concentrations increasing from ~20 to ~75 wt% at the seafloor.

Since 3.0 Ma the sedimentation rate markedly slowed, initially to ~79 m/m.y. (to 2.0 Ma) and then ~59 m/m.y. (to 0.5 Ma) and ~34 m/m.y. thereafter. The marked change in the sediment supply to the area corresponds in part to a decrease in the volcaniclastic sand deposited by turbidity currents. Above 169 mbsf (2.58 Ma), the input of fine metamorphic detritus marked by the presence of illite to 520 mbsf also ends. By this time and since then, the sedimentation rate was much slower than the margin subsidence and the surface deepened to upper middle bathyal (500–1150 m) depths. No record of the last 120 k.y. is preserved, and this may be responsible for the low porosities (65%–70%) near the surface. Pleistocene sedimentation was dominated by nannofossil ooze with volcanic ash. The Pleistocene volcanic ash fallout layers and middle–late Pliocene volcanogenic turbidites record a marked increase in explosive Trobriand Arc volcanism since 3.7 Ma.

The thermal gradient determined from five temperature measurements between 26 and 227 mbsf is $28°C·km^{-1}$, yielding a heat flow of $28\ mW·m^{-2}$ given the average thermal conductivity measured on cores from this interval of $1\ W·m^{-1}·°C^{-1}$.

The magnetostratigraphic record of the upper 400 m is very good. The Brunhes/Matuyama/Gauss/Gilbert polarity transitions, and the Jaramillo, Olduvai, and Kaena Subchrons are identified, as are the Cobb Mountain and Reunion events. Very low magnetic susceptibilities characterize the intervals 210–410 mbsf and 480–550 mbsf, without apparent correlation to grain size, lithology, or sedimentation rate. The variation of susceptibility with depth observed at Site 1115 between 120 and 550 mbsf is similar to that observed at Site 1109 between 80 and 705 mbsf, and the susceptibility boundaries at both sites are time correlative (Figs. **F12, F13**).

Hole 1115C was successfully logged above 784 mbsf with triple combo geophysics and FMS-sonic tool strings. The well seismic tool was used to record check shots near the base of the hole, allowing depth correlation with seismic reflection lines.

The longest profile to date of the deep subseafloor biosphere was made at this site (Fig. **F14**). Bacteria were present in the deepest sample analyzed (801 mbsf) and both dividing and divided cells were present to 775 mbsf. The persistence of apparently living microbial life into indurated sedimentary rock ~15 m.y. old and to 801 mbsf extends the limit of the biosphere whose base remains undefined. Methane is present at levels above 1000 ppm from 250 to 450 mbsf and above
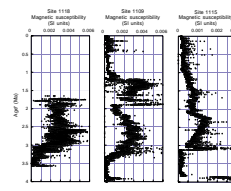
F11. Porosity data for Sites 1108, 1109, 1111, 1114, 1115, 1116, and 1118, **p. 44**.
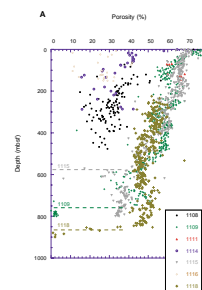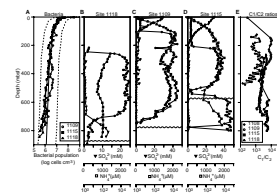
F12. Magnetic susceptibility for Sites 1118, 1109, and 1115 aligned to the top of the Mammoth polarity event, **p. 46**.
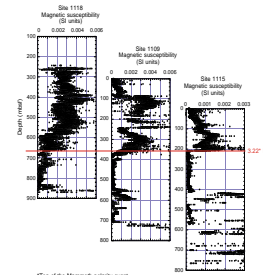
F13. Magnetic susceptibility for Sites 1118, 1109, and 1115 as a function of age, **p. 47**.

F14. Biogeochemical profiles in sediments, Sites 1109, 1115, and 1118, **p. 48**.

20,000 ppm from 572 to 802 mbsf (Fig. F14). The C_1/C_2 ratios generally exceed 1500 and 3000 over the same intervals, and broad maxima in ammonia are found within 200–450 mbsf and at the base of the hole. These observations are consistent with a biogenic origin for the volatile hydrocarbons and the presence of a significant amount of bacteria at depth.

High-resolution pore-water sampling (63 whole rounds) comprehensively documents the interstitial water chemical variations (Fig. F15). In the upper 300 mbsf of the cored section, pore-water variations primarily reflect the oxidation of organic matter and the concomitant early diagenesis of biogenic carbonate (including aragonite) leading to precipitation of dolomite, as well as alteration of detrital, mostly volcanic, matter. Further downhole, most of the pore-water variations are controlled largely by the alteration of volcanic minerals and the formation of clays and zeolites. Silicification appears to be a dominant process below 500 mbsf. The formation of calcite cements is significant in sediments of the forearc sequence.

Site 1109

Hole 1109A (APC):
    9°30.390′S, 151°34.388′E; 2210.9 mbsl
    0–9.50 mbsf cored; 9.96 m recovered (105%)
Hole 1109B (APC):
    9°30.396′S, 151°34.391′E; 2211.1 mbsl
    0–14.80 mbsf cored; 15.14 m recovered (102%)
Hole 1109C (APC/XCB):
    9°30.392′S, 151°34.390′E; 2211.0 mbsl
    0–375.70 mbsf cored; 323.11 m recovered (86%)
Hole 1109D (RCB):
    9°30.380′S, 151°34.355′E; 2211.0 mbsl
   0–352.80 mbsf drilled without coring; 352.80–802.00 m cored;
    299.87 m recovered (67%)

Site 1109 is located on the Woodlark Rise, 11 km north of a major south-dipping normal fault system that is antithetic to the low-angle fault dipping north from Moresby Seamount (Figs. F5, F7). The site was positioned to cross a sequence boundary and an angular unconformity at about 350 and 770 mbsf, respectively, beneath which a lower stratified sequence, interpreted to be prerift forearc basin sediments, dips northward at ~10°.

Four holes were drilled at Site 1109: two short APC holes (1109A and 1109B), one APC/XCB (1109C), and one RCB (1109D). These allowed coring to a total depth of 802 mbsf, complete logging above 786 mbsf with the triple combo geophysical tool, logging two intervals (112–351 and 376–786 mbsf) with the FMS-sonic tools, and conducting a well seismic tool-vertical seismic profile (WST-VSP) with nine receiver locations from 378 to 460 mbsf. The following description uses unit boundaries derived from integrated core-log data interpretation.

Data from Site 1109 show a record of progressive subsidence (from subaerial to lagoonal, then shallow marine and deep water) over a period from latest Miocene to late Pleistocene (Fig. F10). These data provide the information to fulfill one of our primary objectives: to determine the sedimentology, biostratigraphy, and vertical motion history of the synrift sediments on the hanging wall margin to the Moresby low-angle normal fault.

F15. Dissolved Ca^{2+}, Mg^{2+}, and SiO_2 profiles at northern margin (Woodlark Rise) sites, p. 49.
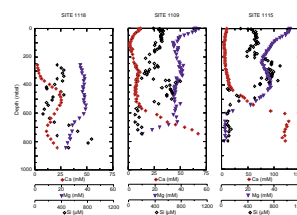
A second objective, to determine the nature of the forearc basin sequence beneath the rift-onset angular unconformity, was thwarted by the unexpected presence of a massive dolerite with ophitic texture from 773 to 802 mbsf, overlain to 730 mbsf by a conglomerate of dolerite7

and some basalt cobbles in an altered clayey silty matrix with nonrecovered interbeds likely similar to the overlying unit (Fig. F9). The dolerite has seismic velocities of 5–6 km·s^{-1}. Culminations observed on reflection seismic sections to be developed locally on the erosional unconformity—previously interpreted as reefs—may be volcanic constructions.

From 713 to 730 mbsf, a very altered, clay-rich siltstone and fine-grained sandstone were recovered, including goethite concretions. A nonmarine, swampy setting is inferred. These sediments contain scattered basalt/dolerite clasts that logging data indicate were derived from discrete conglomerate intercalations. The oogonia of charophyte algae present in Sample 180-1109D-39R-CC indicate a locally freshwater environment at the top of this unit.

We envision deposition in a lagoonal setting of the silty claystone and clayey siltstone encountered between 672 and 713 mbsf. Shell, plant, and wood fragments are common to abundant. The lagoon was alternately brackish and, as indicated by the presence of dolomite, hypersaline. This unit has high natural gamma ray and porosity (45%–50%), low magnetic susceptibility, and velocities ~2 km·s^{-1}.

The first (lower Pliocene: NN13 and N19/20) sediments deposited in a shallow-marine (<150 m water depth) environment occur at 588–664 mbsf and are mixed carbonate-siliciclastic rocks. From 599 to 672 mbsf the lithology consists dominantly of well-cemented, 30%–40% porosity, sandy bioclastic packstone/grainstone. A lower limestone section (643–672 mbsf) with high resistivity (3 Ωm), has low natural gamma ray, 40–80 wt% calcium carbonate, and average velocities of 2.5–3.0 km·s^{-1}. An upper sandstone section with lower resistivity (<2 Ωm), has high natural gamma ray, 20–30 wt% calcium carbonate, and average velocities of 2.0–2.5 km·s^{-1}. Above this is an interval (570–599 mbsf) of calcareous (bioclastic) sandstone with 40–50 wt% calcium carbonate and 45%–50% porosity. The entire sequence reflects relatively shallow-water sediments derived from both volcanic-related and neritic carbonate source materials that accumulated before 4 Ma at >70 m/m.y.

A succession of clay-rich siltstones and silty claystones, interlayered with thin (1–10 cm) medium- to fine-grained sandstones, at 390–570 mbsf was rapidly deposited (312 m/m.y.) in upper bathyal (150–500 m) water depths until ~3.35 Ma. Porosity increases (to 60%) as calcium carbonate decreases (to 25 wt%) upsection to ~480 mbsf, whereas velocities steadily decrease from 2.0 to 1.8 km·s^{-1} up the unit, and magnetic susceptibilities are constantly low above 540 mbsf. These are hemipelagic carbonate muds with turbiditic sand interbeds from a dominantly unaltered basalt-andesite volcanic source with minor neritic carbonates, deposited on a well-oxygenated and extensively bioturbated slope.

Above 380 mbsf, significantly greater magnetic susceptibilities that continue to 83 mbsf correspond to the influx of clays and silts from an additional source terrane, characterized by altered calc-alkaline volcaniclastic material and metamorphic detritus with mixed-layer, and probably smectite, clays. Between 330 and 390 mbsf (~3.07–3.35 Ma) the silty claystone is nearly devoid of sandy interbeds. The lower portion (up to 353 mbsf) has a high frequency of layers with unaltered volcaniclastics. The section from 295 to 330 mbsf was deposited at 69 m/m.y. between 2.57 and 3.07 Ma. Seismic reflection data show that this compressed

section is part of a conformable slope sequence that substantially thickens downslope toward the rift basin to the south (i.e., there is a regional "onlap" relationship of flat basin turbidites laterally continuous with conformable slope deposits).

The margin continued to subside with an accumulation rate of 66 m/m.y. between 3.07 and 1.95 Ma (295–255 mbsf), and above 285 mbsf was at middle bathyal (500–2000 m) water depths. Distal silt-clay bioturbated turbidites with volcanic, terrigenous, and biogenic components rapidly onlapped the margin (225 m/m.y.) from 1.95 Ma until 1.0 Ma (~42 mbsf). These include a significant component of reworked slope sediments, as evidenced by dominantly upper Pliocene biota in the younger section. Volcaniclastic sands are most frequent from ~100 to 170 mbsf. Silt to coarse-grained sand interbeds are common from 170 to 247 mbsf, including a poorly recovered sand from 218 to 233 mbsf. These sands are remarkable for their high thorium and potassium contents, producing high natural gamma-ray counts, and lower porosities (40%–50%) and higher velocities (2 km·s^{-1}) than adjacent intervals (60%–70% and 1.7 km·s^{-1}, respectively).

Between 1.0 and 0.46 Ma the site was relatively sediment starved and/or intermittently eroded (the site is located in a submarine valley), with net accumulation rates of 21 m/m.y. of calcareous clayey silt and silty clay with some thin volcanic ash layers. Since 0.46 Ma, nannofossil-rich, calcareous sand, silt, and clay with volcaniclastic sand and volcanic ash, were deposited at 67 m/m.y. Only the surface sediment has a lower bathyal (>2 km) benthic fauna.

Extensional deformation is very weak throughout the section, except for minor normal faults at about 260 and 360 mbsf and normal shear zones at 678–685 mbsf and in the dolerite. A folded region at 36–55 mbsf is interpreted as a slump.

Velocities linearly increase with depth from 1.5 km·s^{-1} at the surface to 1.9 km·s^{-1} at 520 mbsf, and then more rapidly to 2.2 km·s^{-1} at 590 mbsf with the increasing calcium carbonate. Velocities increase to 3–4 km·s^{-1} and are more variable in the bioclastic sandstones and limestones between 590 and 672 mbsf, and then return to 2 km·s^{-1} in the lagoonal sequence below that. Porosity decreases downward, but the usual negative exponential decay is interrupted at two levels (160–280 and 350–540 mbsf) where the higher porosity reflects undercompaction correlated with periods of high sedimentation rates (225–312 m/m.y.) (Fig. F11). The thermal conductivity generally mirrors the porosity-depth profile and ranges from 0.78 to 1.5 W·m^{-1}·°C^{-1}, except for the dolerite, which shows values up to 2 W·m^{-1}·°C^{-1}. Six temperature measurements down to 170 mbsf define a linear thermal gradient of 31°C·km^{-1} and, when combined with an average thermal conductivity of 0.9 W·m^{-1}·°C^{-1} over this interval, a heat flow of 28 mW·m^{-2}.

Although their number rapidly decreases with depth, bacteria are present in all samples obtained down to 746 mbsf. Total populations and numbers of dividing and divided cells show obvious relationships to the sediment geochemistry (Fig. F14). Pore-water constituent profiles show that carbonate diagenesis occurs at shallow depth (above 100 mbsf), aided by the bacterial decomposition of organic matter. Diagenetic transformation of pre-existing detrital clay minerals occurs to 300 mbsf. Bacterial activity further downhole is evidenced by deep-seated (430–550 mbsf) ammonia and alkalinity submaxima (the latter likely because of increased CO_2 production). Of note is a generally increasing pH downhole, from 7.8 to greater than 8.6. Pore-water composition

also reflects the alteration of volcanic components, formation of authigenic clay minerals, silica diagenesis, and diffusion of elements above the shell-rich and freshwater units below 672 mbsf. A crossover of Ca and Mg profiles, as often observed above igneous sills, occurs at 661 mbsf.

Headspace gas analyses show a typical methane profile, with concentrations increasing rapidly at 100 mbsf from ~5 to ~6000 ppm, then remaining between 1000 and 10,000 ppm down to 600 mbsf. Methane content begins to decrease below 600 mbsf, reaching 5 ppm by 720 mbsf. The only other hydrocarbon detected was C_2, but it remained below 3.2 ppm throughout the entire cored section. The C_1/C_2 ratios did not drop below 1000, and organic carbon was generally <1% throughout the core.

Site 1118

Hole 1118A (RCB):
    9°35.110′S, 151°34.421′E; 2303.6 mbsl
    0–205.0 mbsf drilled without coring; 205.0–926.6 mbsf cored;
   466.21 m recovered (65%)

Site 1118 is 1.8 km north of a major south-dipping normal fault system that is antithetic to, and bounds the rift basin above, the low-angle fault dipping north from Moresby Seamount (Figs. F5, F7). The location was selected in order to drill through the thick synrift section onlapping the northern margin and to penetrate an angular unconformity into north-dipping reflectors deep in the inferred prerift forearc basin sequence. The site is ~9 km due south of Site 1109 and has similar objectives in common to it and Site 1115, namely to determine (1) the sedimentology, biostratigraphy, and vertical-motion history of the northern margin, and (2) the nature of the forearc basin and basement sequence.

Results from Site 1118 record the progressive subsidence of a lower Pliocene, subaerially eroded and tropically weathered, landmass (Figs. F9, F10). A conglomerate of dolerite with minor basalt was recovered (Fig. F16) and imaged with FMS below 873 mbsf. Iron oxides and well-rounded clasts reveal that the dolerite, similar to that encountered at Site 1109 (although locally more pegmatitic), was exposed to subaerial alteration. Shearing and veining fragmented and partially brecciated the dolerite, which was deposited as a poorly sorted, probably fluvial conglomerate mixed with various clasts and sediment, including paleosols.

The dolerite conglomerate is overlain to 857 mbsf by a sequence of lower Pliocene limestones, calcareous paraconglomerates, and a volcaniclastic sandstone that was deposited in a marine lagoon with abundant calcareous algae. This sequence is well marked in the geophysical logs and by highs in the $CaCO_3$ profile of >80 wt%. A VSP shows that the dolerite-limestone section corresponds to a strong reflector at the base of the sedimentary sequence that mantles underlying northward-dipping reflectors, which were not penetrated.

The Gauss/Gilbert Chron boundary (3.58 Ma), occurring at 846–850 mbsf, dates an upward-fining sequence disconformably above the limestones as all middle Pliocene and younger, in agreement with paleontological data (Biozones N20–N21 and NN16A–NN19A through the top of the cored sequence at 205 mbsf). The lower sedimentary section records a significant terrestrial input, including wood fragments, confirmed by

F16. Hole 1118A core photograph illustrating the rift onset unconformity and the transition facies from dolerite overlain by conglomerate, limestone, and volcaniclastic sandstone, p. 50.
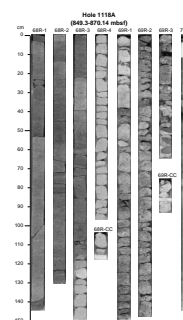
the C/N ratio, which indicates a mixed-marine and terrigenous source of organic carbon. The whole sequence records turbiditic and hemipelagic sedimentation. It comprises mixed volcaniclastic sandstones, siltstones, and minor claystones, and then mostly siltstones and claystones interbedded with turbiditic sandstones and siltstones that decrease in proportion upward. The orientations of the subhorizontal maximum axes of the ellipsoids of magnetic susceptibility (corrected for bedding dip and core orientation) between 490 and 680 mbsf suggest an east-southeast–west-northwest–directed paleocurrent during sedimentation, almost perpendicular to the present-day slope.

The sedimentation rate from 3.58 to 2.58 Ma (387.5 mbsf) was 479 m/m.y., the highest encountered during Leg 180, with benthic foraminifers revealing an upper bathyal (150–500 m) paleowater depth. Between 2.58 and 1.95 Ma (288 mbsf), the sedimentation rate decreased to 155 m/m.y., and the paleodepth was middle bathyal (500–2000 m) to at least 205 mbsf. Apparently, rapid subsidence since 3.6 Ma was accompanied by sufficient sediment supply to limit deepening of the seafloor until 2.6 Ma. High porosities slowly decreasing from 50%–60% at 205 mbsf to 40%–50% at 800 mbsf likely reflect underconsolidation related to the observed high sedimentation rates.

Volcanic ash and volcaniclastic sands are ubiquitous throughout the Pliocene sedimentary section, but especially so in the portion dated to between 3.0 and 3.6 Ma (Fig. F17) in which a predominance of rhyodacitic glass reflects explosive acidic volcanism probably associated with rifting of the continental arc.

Most of the sedimentary section is undeformed with nearly horizontal beds and shows compaction-related minor faults as well as common slump folds. The abundance of synsedimentary features on such a nearly level seafloor suggests an unstable area periodically shaken by earthquakes and affected by mass movement.

As seen in other northern sites drilled during Leg 180, the variations in interstitial water constituents reflect the oxidation of organic matter mediated by microbial activity and the concomitant early diagenesis of biogenic carbonates (Figs. F14, F15). Volcanic alteration and authigenesis are important processes, particularly in the lower part of the hole. The abundance of volcaniclastic sands and the higher porosities in the lower part of the hole, when combined with the high temperature gradient (~63°C·km^{-1}), greatly influence the pore-water chemistry. In particular, the dissolved silica, lithium, and strontium show higher concentrations than might otherwise be expected. In addition, temperature measurements in the open hole during a logging run suggest migration of warm fluids at 700–800 mbsf.

Both methane and ethane, whose ratio is between ~5000 and ~1600, are present down to ~700 mbsf, below which ethane is not detected. The highest concentrations in these two volatile hydrocarbons occur where sulfate disappears from the interstitial water, attesting to a biogenic origin.

Bacteria population numbers and dividing and divided cells decrease rapidly with increasing depth and conform to the general model for their distribution in marine sediments. In extending their known distribution to 842 mbsf at this site, the deepest samples so far obtained, there is an indication that numbers are decreasing more rapidly than the model predicts, resulting in a sigmoidal depth distribution in these sediments (Fig. F14).

F17. Volcanogenic ash layers at Sites 1118, 1109, and 1115 in terms of thickness (gray) and number of layers (black) per core, p. 51.
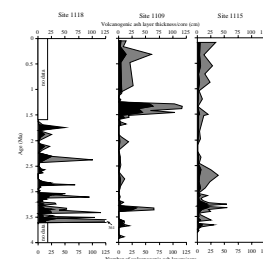
Site 1108

Hole 1108A (jet-in test only):
    9°44.708′S, 151°37.514′E; 3162.7 mbsl
    0–16.3 mbsf drilled without coring
Hole 1108B (RCB):
    9°44.724′S, 151°37.543′E; 3177.2 mbsl
    0–485.2 mbsf cored; 148.58 m recovered (30%)

Site 1108 is in the seismically active region of incipient continental separation 1 nmi ahead of the neovolcanic zone of the Woodlark Basin spreading center, Papua New Guinea (Fig. F7). Here, a continental fault block (Moresby Seamount: summit 120 mbsl) forms the footwall to a low-angle normal fault imaged to 9 km that dips 25°–30° beneath a 3.2-km-deep, asymmetric rift basin with more than 2 km of sediment fill (Fig. F4). At Site 1108 we sought to drill through ~900 m of the rift basin sediments, the low-angle normal fault zone, and into the footwall metamorphics. The primary objectives at this site were to (1) characterize the composition and in situ properties (stress, permeability, temperature, pressure, physical properties, and fluid pressure) of the active low-angle normal fault zone to understand how such faults slip and (2) determine the vertical- motion history of the hanging wall and the footwall as local ground truth for models of the timing and amount of continental extension before spreading initiation. Hole 1108A was a jet-in test in anticipation of reentry operations. Hole 1108B was rotary cored to 485 mbsf, with ~60 m of open-hole logging using the triple combo and temperature tools before unstable hole conditions terminated operations. The site was not deepened because of pollution prevention and safety concerns, and hence, the primary objectives were not met.

The first core contained upper Pleistocene nannofossil-bearing hemipelagic sediment: calcareous clay with minor volcaniclastic silt and sand. Talus from Moresby Seamount was recovered as isolated clasts from 14.5 to 62.7 mbsf and included dark siliciclastic sandstone and siltstone, volcanic breccia, microgranite, granodiorite, epidosite, greenschist mylonite, and biotite gneiss. Some glassy basalt fragments from submarine eruptions were incorporated in the same interval. Trace amounts of adhering sediments reveal biostratigraphic ages >1.25 Ma by 24.1 mbsf. Quartzo-feldspathic-lithic sand from 62.7 to 63.4 mbsf may relate to and herald the overlying talus. Gas observed bubbling out of the top of the core barrel for this interval may reflect penetration of a gas hydrate layer.

Terrigenous turbidites, now lithified to sandstones, siltstones, claystones, and minor conglomerates, constitute the remainder of the section 72.3–485.2 mbsf (Fig. F9). Ages increase from 1.67 to 1.75 Ma at 82.8 mbsf to <3.35 Ma at the base. Sedimentation rates increase downsection, from 324 m/m.y. at 1.7–2.0 Ma to 400 m/m.y. at 2.60–3.2 Ma. Benthic foraminifers indicate deposition in deep water (lower bathyal: >2000 m), except for middle (500–2000 m) to lower bathyal conditions below 410 mbsf (Fig. F10).

The majority of the turbidites comprise interbedded sandstones, siltstones, and claystones in which medium- to coarse-grained sediments dominate. The sandstones above ~330 mbsf contain a high proportion of metamorphic-derived lithoclasts, related mineral grains, and altered igneous-rock-derived grains (volcanic and ophiolitic), whereas those below contain large amounts of material derived from basic and acidic

volcanic and minor plutonic rocks. Planktonic foraminifers and bio-clasts of shallow-water origin are common to both sections.

A subunit from 139.4 to 200.2 mbsf comprises foraminifer-bearing clayey siltstone and silty claystone with occasional fine-grained sand-stone. Bioturbation is common. Minor disseminated pyrite is suggestive of relatively low oxygen bottom conditions at times. Subunits of thin conglomerate were recovered near 313, 380, and 437 mbsf. The clayey siltstone subunit shows abundant evidence of brittle deformation characterized by bedding dips of up to 35°, low-angle shearing, brecciation, and ubiquitous slickensides. The faults dip at moderate angles (~45°), and most of the structures indicate normal senses of displacement in an extensional fault zone. The greatest frequency of fractures and faults is concentrated between 158 and 173 mbsf. Within this interval there is an age offset from 2.0 to 2.58 Ma between 159.6–164.8 and 172 mbsf. Based on the sedimentation rates above and below, ~200 m of section appears to be cut out by this normal fault near 165 mbsf.

Within the more competent lithologies below, the intensity of tectonic deformation falls off markedly and bedding is subhorizontal. However, below 350 mbsf the turbidites become finer grained (more claystones, siltstones, and fine sandstones), and the section is once more deformed with scaly fabrics, fractures, and evidence of shear along fault planes. Tectonic deformation appears to be concentrated in the finer grained units.

Porosities measured in the laboratory show an expected exponential decay with depth below ~160 mbsf, but the misfit of these values when extrapolated to the surface with the measured surface porosities indicates that at least 400 m of sediments has been removed (Fig. F11). Half this amount may be associated with throw on the fault near 165 mbsf, the rest with erosion between the unconsolidated sands at 63 mbsf and the consolidated sandstones at 72 mbsf.

Temperature measurements suggest an average thermal gradient of $100°C\cdot km^{-1}$ to 390 mbsf. Alternatively, the same data may be explained by advection of fluids along the ~165-mbsf fault, and/or by a thermal gradient of $94°C\cdot km^{-1}$ above 160 mbsf and $65°C\cdot km^{-1}$ below 200 mbsf, with a 10°C offset formed in the last thousand years. Thermal conductivities in the upper several meters are $0.8–0.9 W\cdot m^{-1}\cdot °C^{-1}$ and are $1.0–1.7 W\cdot m^{-1}\cdot °C^{-1}$ below 130 mbsf.

Three processes appear to control the pore-water geochemistry. Bacterially mediated oxidation of organic matter depletes sulfate 75% by 83 mbsf (and totally below 172 mbsf), the depth where methane concentrations become elevated and there is a salinity minimum. The downhole decrease in K^+ and Mg^{2+} and the increase in salinity, Na^+, Cl^-, Ca^{2+}, Li^+, and Ca/Mg (locally modulated by the formation of calcite cements) are consistent with diagenesis of volcanic matter to form clay minerals. Depth profiles of all these ions show offsets or local deviations associated with the fault at ~165 mbsf.

Organic carbon contents average 0.5 wt%. The C/N ratios mainly between 8 and 20 suggest a mixed terrigenous and marine origin for the organic matter. Headspace gas data show a C_1/C_2 ratio decreasing from ~2000 at 335 mbsf to 138–195 in the deepest samples (467 and 476 mbsf) (Fig. F14). Starting at 391 mbsf, there is an increasing presence of higher chain volatile hydrocarbons indicative of thermogenically derived gas.

Sites 1110 through 1113

Site 1110

Hole 1110A (APC):
  9°43.599′S, 151°34.511′E; 3246.4 mbsl
  0–9.5 mbsf cored; 9.5 m recovered (100%)
Hole 1110B (APC/XCB):
  9°43.609′S, 151°34.509′E; 3246.3 mbsl
  0–22.3 mbsf cored; 5.37 m recovered (24%)
Hole 1110C (RCB):
  9°43.599′S, 151°34.498′E; 3245.8 mbsl
  0–15.0 mbsf drilled; no cores taken
Hole 1110D (RCB):
  9°43.588′S, 151°34.526′E; 3245.8 mbsl
  0–22.7 mbsf drilled; 22.7–28.7 mbsf cored;
  0.10 m recovered (2%)

Site 1111

Hole 1111A (RCB):
  9°43.059′S, 151°34.533′E; 3200.7 mbsl
  0–173.7 mbsf cored; 15.19 m recovered (9%)

Site 1112

Hole 1112A (RCB):
  9°44.749′S, 151°36.721′E; 3046.7 mbsl
  0–122.4 mbsf cored; 5.85 m recovered (5%)
Hole 1112B (RCB):
  9°44.746′S, 151°36.714′E; 3046.6 mbsl
  0–126.1 mbsf drilled without coring; 126.1–164.6 mbsf cored;
  1.19 m recovered (3%)

Site 1113

Hole 1113A (RCB):
  9°45.449′S, 151°36.737′E; 2915.6 mbsl
  0–25.2 mbsf cored; 0.44 m recovered (2%)

Sites 1110 through 1113 were drilled in various locations near the foot of Moresby Seamount (Fig. F8) in an attempt to find a viable alternate location to our primary Site 1108. With the hydrocarbon safety restriction of 485 mbsf, the depth reached at Site 1108, we sought to intercept the Moresby low-angle normal fault in other locations or at shallower depths. We first tried two locations ~6 km west-northwest of Site 1108, near the rift basin depocenter located due north of Moresby Seamount. We then tried two other locations updip of Site 1108, all without success.

At Site 1110, where the fault may be 400–450 mbsf, multiple holes were unable to penetrate below ~29 mbsf because of talus beneath ~9 m of surficial calcareous clay, late Pleistocene in age (<0.22 Ma). The pebbles and cobbles of the talus include micaschists, amphibolites, and rare granite porphyry.

Moving 1 km north, at Site 1111, we cored a single hole through ~154 m of Pleistocene deposits (<1.02 Ma): talus pebbles and cobbles in calcareous ooze, clay, and silty clay with lesser nannofossil-rich silt,

sand, and gravel. The talus includes metasediments (micaschist and gneiss) and variably metamorphosed igneous rocks, both basic (dolerite, metadolerite, and lamprophyre) and acidic (granite porphyry). Coring was stopped at 174 mbsf in large metamorphic cobbles. Based on temperatures measured at the mudline and at 136 mbsf, the thermal gradient is 95°C·km^{-1}, similar to that encountered at Site 1108, and the heat flow is 86 mW·m^{-2}.

Site 1112 is 1.5 km west of, and updip from, Site 1108, where the depth to the fault is ~450 mbsf. Another thick pile of talus deposits in Pleistocene (<1.75 Ma) sediments, including silty clay with occasional ash, required two RCB holes to reach 165 mbsf. The recovery consisted of pebbles only, mostly of metadolerite and epidosite, but also minor andesite, granite porphyry, micaschist, and sandstone.

After offsetting 1.3 km south, we attempted a "bare rock" spud at the base of the slope of Moresby Seamount where the fault crops out (Site 1113), but there was enough talus to make the hole unstable and repeatedly refill, and it was abandoned at 25 mbsf in micaschist and epidosite pebbles and cobbles.

Most of the metamorphic rocks recovered from the talus of Moresby Seamount have igneous protoliths. In addition, micaschists and gneisses record an early tectono-metamorphic stage characterized by the development of a foliation under epidote-amphibolite to amphibolite facies conditions. A later retrograde metamorphism in the greenschist facies affected all protoliths. This later stage was coeval to brittle extensional deformation and extensive hydrothermal alteration, probably during the normal faulting of Moresby Seamount and the subsequent unroofing of its basement.

Site 1117

Hole 1117A (RCB):
   9°46.526'S, 151°32.945'E; 1663.2 mbsl
   0–111.1 mbsf cored; 6.42 m recovered (6%)
Hole 1117B (RCB):
   9°46.527'S, 151°32.951'E; 1663.2 mbsl
   0–9.5 mbsf cored; 0.05 m recovered (0.5%)
Hole 1117C (RCB):
   9°46.520'S, 151°32.943'E; 1663.2 mbsl
   0–9.5 mbsf cored; 1.05 m recovered (11.1%)

Site 1117 is on the upper slope of the northern flank of Moresby Seamount, 3.5 km to the northwest of Site 1114 (Figs. F6, F8). It was a successful attempt to bare-rock spud into, and drill through, the main detachment fault where it crops out.

The base of the cored section consists of a noncumulate, quartz-magnetite gabbro (Fig. F18) that passes upward into brecciated and then mylonitized equivalents, with a fault gouge at the surface. The upward-increasing shearing and alteration confirm that the northern flank of the seamount is an outcropping fault surface. The first undeformed gabbro occurs at 86 mbsf, but brecciated gabbro was found deeper in the section, at 96 mbsf. Therefore, the minimum thickness of the shear zone preserved within the footwall is about 100 m.

In the surficial core we recovered 4 m of soft, light-colored, clayey material with a soapy feel, interpreted as a fault gouge (Fig. F19). This material contains talc, chlorite, calcite, ankerite, and serpentine, which is consistent with hydrothermal alteration of the underlying deformed

F18. Coarse-grained gabbro, Site 1117, p. 52.
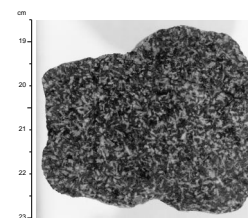
F19. Core photograph of fault gouge, Site 1117, p. 53.
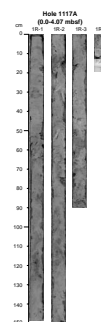
gabbro. It has low porosity (~30%), bulk density of ~2.2 $g \cdot cm^{-3}$, unconfined compressive strength in the range of 65–90 kPa, thermal conductivities of 1.3–1.8 $W \cdot m^{-1} \cdot °C^{-1}$, and transverse sonic velocities of ~2 $km \cdot s^{-1}$. These physical properties strongly contrast with those common to near-seafloor deposits and to the gabbro protolith below (porosity 3%, bulk density 2.76 $g \cdot cm^{-3}$, thermal conductivity up to 3.8 $W \cdot m^{-1} \cdot °C^{-1}$, and sonic velocity 6.0–6.4 $km \cdot s^{-1}$). Although the fault gouge has been exposed at the seafloor, its characteristics still reflect its deformational origin. The shape parameter of the ellipsoid of magnetic susceptibility (T = 0.2–0.8) indicates an oblate magnetic fabric and the degree of anisotropy of the magnetic susceptibility is maximum in the fault gouge (P_j = 1.1–1.2), both indicative of flattening as a result of high shear strain.

The deformation textures in the gabbro range from brecciated to cataclastic to mylonitic, almost totally obscuring the initial subautomorphic texture. Mylonite clasts recovered down to 57 mbsf show a well-developed foliation with S-C structures (Fig. **F20**). Within the foliation, the association of epidote-rich and very fine grained layers of quartz, epidote, and chlorite reveals greenschist facies conditions during deformation. Asymmetrical fibrous quartz pressure shadows present around pyrite also attest to syntectonic metamorphism. The gabbro between 62 and 86 mbsf shows evidence of increasing brecciation upward, passing progressively to the mylonite. Quartz + epidote veins, reoriented parallel to the foliation in the mylonite, suggest that the brecciation was assisted by silica-rich fluids. Late veins of epidote and calcite cut the rock, attesting to more carbonate-rich fluids in the late stage of shearing. Late alteration, associated with fluid flow within the shear zone, has produced chlorite, talc, and fibrous amphibole replacing primary plagioclase and clinopyroxene.

The mineralogy and texture of the gabbro are similar to those of high-level gabbros occurring in ophiolites. These gabbros, together with the presence of dolerites reminiscent of a sheeted dolerite complex at Site 1114, suggest that Moresby Seamount may be part of an ophiolitic complex exhumed by extension along the northward-dipping low-angle normal fault bounding the seamount to the north.

Site 1114

Hole 1114A (RCB):
   9°47.613′S, 151°34.504′E; 406.5 mbsl
   0–352.80 mbsf cored; 43.78 m recovered (12%)

Site 1114 is just north of the crest of Moresby Seamount where seismic reflection data indicate that the basement beneath a south-southwest–dipping normal fault is shallowest (Figs. **F5, F8**). The primary objective was to determine the internal structure and composition of Moresby Seamount, particularly the nature of the basement (rock type, pressure-temperature history, structural fabric, and deformation history). A second objective was to determine the sedimentology, biostratigraphy, and vertical motion history of the ~300 m of local sedimentary cover, which may correspond to the uplifted and partly eroded synrift sequence.

In Hole 1114A, we drilled ~286 m of Pliocene–Pleistocene sediments separated by a 6-m-thick tectonic breccia from a metadolerite that forms the basement (Fig. **F21**). The dolerite was metamorphosed under low-grade greenschist facies conditions before its upper part, which

F20. Sheared gabbro with foliation plane and shear bands, Site 1117, **p. 54**.
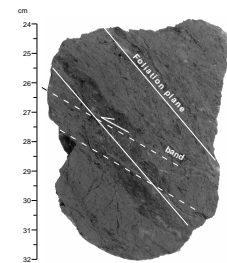
F21. Lithostratigraphy of Sites 1114, 1116, and 1117 on Moresby Seamount, **p. 55**.
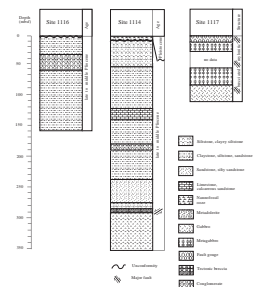
contained a chilled margin, was reactivated by normal faulting, leading to its unroofing.

The sediments consist of rift-related, mostly volcaniclastic, turbidites deposited in middle bathyal water depths (500–2000 m). The benthic foraminiferal assemblage is characteristic of a suboxic environment of deposition, which may correspond either to a basinal situation with restricted circulation or to the oceanographic oxygen minimum situated at middle to upper bathyal water depths. From bottom to top, the deposition changed from mostly coarse-grained sandstones, ~100 m thick, to a finer grained intercalation of sandstones, siltstones, and claystones. The mineralogy of the sandstones suggests that most of the turbidites were derived from calc-alkaline extrusive rocks, but minerals and clasts from ultramafics and metamorphics (serpentinite and calcschists) are also present, as well as ubiquitous bioclasts.

Only the uppermost sediments are Pleistocene in age. The indurated sediments below 35 cm in Core 180-1114A-2R are all late and middle Pliocene (from >1.67 Ma to 3.09–3.25 Ma) and were deposited at rates of at least 176 m/m.y. (Fig. F10). The offset of the porosity vs. depth curve suggests that from 220 to >400 m of the Pleistocene section has been removed (Fig. F11), which we tentatively relate to the uplift of Moresby Seamount in the footwall of bounding normal fault systems.

The deformation in the recovered sedimentary rocks preferentially occurs in the fine-grained strata, where it is expressed as a scaly fabric with numerous striated surfaces. It increases in intensity approaching the tectonic breccia. The bedding dips in the upper ~110 m range from 0° to 30°, then increase to 25°–60° below that. The FMS data reveal (Fig. F22) that (1) bedding dip directions are dominantly northwest but range from north to west; (2) the basement/sediment faulted contact outlined by the breccia dips ~60° toward the southwest, slightly oblique to the main normal fault that offsets basement by >2 km; and (3) in contrast, faults within the overlying sedimentary rocks mostly dip to the north, but a few dip to the south just above the breccia. The sense of motion on faults within the sedimentary rocks is dominantly normal, but reverse and oblique slip faults also exist. These observations suggest that a component of left-lateral motion exists on the bounding, south-southwest-dipping normal fault, in agreement with regional evidence for north-south extension.

The brecciated fault contact is also marked by an abrupt increase in the degree of hydrothermal alteration. The alteration in the breccia and metadolerite is characterized by massive clay and calcite veins that crosscut numerous quartz and epidote veins. In the breccia, the latter veins are restricted to the clasts. The hydrothermal alteration tends to decrease downward in the metadolerite, suggesting that fluids were channeled into the tectonic breccia.

Site 1116

Hole 1116A (RCB):
    9°51.934′S, 151°34.508′E; 1851.3 mbsl
    0–158.90 mbsf cored; 32.61 m recovered (21%)

Site 1116 is on the southern flank of Moresby Seamount, 8 km south of Site 1114, within a tilted block bounded by two normal faults that each offset the basement by >1 km to the south-southwest (Figs. F5, F8). The objectives for this site were to characterize the early rift sediments and the seamount basement (which was not reached).

F22. Bed and fracture dip directions and strikes from FMS images analysis at Site 1114, p. 56.
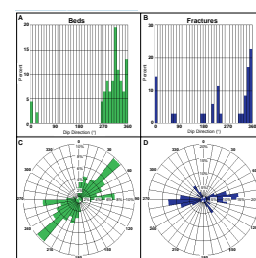
Very low surface porosity (~30%), and high bulk density (~2.15 g·cm⁻³), sonic velocity (2.2–2.8 km·s⁻¹), and thermal conductivity (1.0–2.2 W·m⁻¹·°C⁻¹) values, suggest that 700–1000 m of the section has been removed by faulting and/or erosion (Fig. **F11**). This is consistent with the lack of a Quaternary and uppermost Pliocene section, as well as the seismic stratigraphy.

The recovered section is dominated by Pliocene indurated sandstones alternating with siltstones/claystones (Fig. **F21**). The sandstones are fine to medium, and occasionally coarse grained, and display parallel, wavy, and convolute laminations, which indicate they originated from turbidity currents in a near-source slope setting. A paraconglomerate is present at 34–63 mbsf. The sandstones below this are subarkosic with a calcareous matrix. Measured $CaCO_3$ contents are <5 wt%. Some thick-bedded, reverse-graded sandstones with occasional intraformational rip-up clasts were deposited from high-density turbidity currents. However, normal grading and lamination in some siltstones/sandstones also indicate deposition by low-concentration turbidity or bottom currents. The matrix-supported conglomerates, interbedded with sandstones and siltstones, comprise relatively unaltered, mainly angular clasts and are interpreted as debris-flow deposits.

Benthic foraminifers indicate middle bathyal paleowater depths (500–2000 m), with inner neritic (<50 m) benthic foraminifers redeposited within turbidite beds. The N20/N21 boundary (3.35 Ma) occurs between 104 and 128 mbsf, and the minimum age of 1.95 Ma at the surface yields a minimum sedimentation rate of 70 m/m.y. (Fig. **F10**). Burrows are either abundant or relatively depleted, suggesting alternating poorly and well-oxygenated subseafloor conditions with, in both cases, abundant detrital organic matter input and a mostly terrigenous source, as indicated by C/N ratios.

The orientations of the subhorizontal maximum axes of the ellipsoids of magnetic susceptibility (corrected for bedding dip and core orientation) below 100 mbsf indicate northeast-southwest or northwest-southeast–directed paleocurrents during sedimentation.

The sources of clastics are little-altered basic extrusive rocks of mainly calc-alkaline affinities, probably derived from the Miocene Trobriand Arc, but also include acidic extrusives, shallow-water bioclasts, metamorphics, and serpentinite. The serpentinite, rare chromite, and some of the gabbro and dolerite grains probably have an ophiolitic origin (Paleocene–Eocene Papuan Ultramafic Belt?).

The upper 100 m of the section shows abundant evidence of synsedimentary deformations, including folding and low-angle extensional faulting typical of gravity-driven processes. The bedding dips <10°, except for fold limbs where it is up to 50°. Common dewatering and fluidization features were possibly seismically triggered. Faults and scaly fabrics are within a narrow zone between 100 and 120 mbsf. They include steep strike-slip and 25°- to 55°-dipping pure normal faults. Below the fault zone beds dip ~15° consistent with the dip of seismic reflectors.

THEMATIC OVERVIEW

Depositional History

Discussion of depositional history of the sites drilled during Leg 180 can be conveniently divided into, first, those on the hanging wall and

northern margin of the active rift basin (Sites 1108, 1109, 1110–1113, 1115, and 1118) and, second, those on the footwall (Sites 1114 and 1116). The northern margin sites are relatively little deformed, well dated, and can be correlated accurately using seismic reflection data. By contrast, the footwall sites are more highly deformed, less well dated, and difficult to correlate using seismic stratigraphy. In addition, owing to faulting, differential sedimentation, and erosion, the footwall and hanging wall sites cannot be correlated with confidence across the rift basin.

Hanging Wall and Northern Margin Sites

Middle to Late Miocene Forearc Succession and Emergence

The oldest well-dated sedimentary rocks recovered during Leg 180 were from Site 1115, the most northerly location of the south-north transect (Fig. F9), and are of middle Miocene to late Miocene age. They are interpreted as part of a forearc basin located north of the calc-alkaline Trobriand Arc and south of the Trobriand Trough subduction zone. These sediments are mainly turbidites deposited in upper bathyal water depths (150–500 m) and derived mainly from basic extrusive rocks. Upward in the middle Miocene succession there is an incoming of redeposited shallow-water carbonate and minor pebbly sandstone. Above this, the upper Miocene interval records shallowing up to a major unconformity.

The uppermost Miocene succession above the unconformity at Sites 1115 and 1109 is emergent to lagoonal. At Site 1115, coring and FMS logging data show the presence of ~3 m of conglomerate composed of well-rounded clasts of basalt together with fine-grained sediments, including possible root traces. At Site 1109, drilling terminated in massive dolerite. This could alternatively (1) form part of a regional Paleogene arc/forearc (part of the Papuan ophiolite belt), (2) record part of the Neogene Trobriand forearc, or (3) relate to rifting of the Woodlark Basin. The dolerite is overlain by conglomerate, as confirmed by interpretation of FMS data. The conglomerates at both sites were apparently deposited in a fluvial to swampy setting. At Site 1109 the nonmarine sediments are thicker and include goethite concretions and altered basaltic material. The overlying lagoonal facies is brackish (alternating fresh and hypersaline) at Site 1109 to initially relatively enclosed and then more open marine at Site 1115. A similar facies (Ruaba unit) is developed at the Nubiam-1 well ~100 km to the northwest where the underlying unconformity is dated as younger than 9.63 Ma (Francis et al., 1987). At that time, Site 1118 was subaerial. An early Pliocene or older conglomerate, at least 50 m thick, was deposited at Site 1118 (Fig. F16), with clasts up to 0.5 m thick, again composed of basalt and dolerite. Lateritic paleosol and breccia are present there in the interstices between clasts.

Rift-Related Subsidence

Each of the three Sites 1115, 1109, and 1118 shows evidence of subsidence from paralic to shallow-marine to deeper (bathyal) water conditions. This transition was diachronous, and began in latest Miocene to early Pliocene time (Fig. F10). The transition from inner to outer neritic and then to upper bathyal water depths occurred first at Site 1109 where shallow-marine carbonates of early Pliocene age accumulated on an open-shelf setting, influenced by traction currents. Similar transitions occurred shortly thereafter at the northern site, Site 1115. At Site 1118, situated on a paleotopographic high, a slightly younger transgres-

sion was marked by deposition of early Pliocene or older shallow-marine conglomerates and then lagoonal carbonate with abundant calcareous algae. Then the sediments pass disconformably into upper bathyal calcareous sands in the latest early Pliocene.

Site 1115 sediments exhibit deepening and rapid deposition (344 m/m.y.) (Fig. F10) mainly by turbidity currents during early Pliocene time (3.9–3.6 Ma). Calcium carbonate increases generally upward in the Pliocene–Pleistocene interval, which correlates with a general increase in the pelagic carbonate component through time (Fig. F23). At Site 1109, ~250 m of hemipelagic mud and fine-grained turbidites accumulated during middle to late Pliocene time. At Site 1118 sediments above the shallow-water succession (sandstone, siltstone, and volcaniclastic sandstone) accumulated in deeper water (150–500 m) at very high sedimentation rates (435–485 m/m.y.; Fig. F10) during latest early to late Pliocene time.

Pliocene–Pleistocene Deposition

At each of Sites 1118, 1109, and 1115 the Pliocene–Pleistocene successions are dominated by deep-marine turbiditic and pelagic lithologies, although with subtle differences in the facies and age at each location. The Pliocene–Pleistocene successions are thickest and show the highest sedimentation rates in the south (Site 1118), decreasing northward through Sites 1109 and 1115 (Fig. F10).

At Site 1118 ~500 m of turbidites and hemipelagic sediments accumulated from upper bathyal depths to middle bathyal depths during middle Pliocene to late Pliocene–Pleistocene? time. Ash-rich interbeds are common (Fig. F24). Reddish, finely laminated, less bioturbated sediments are interspersed with darker colored mainly turbiditic sediments. The interval of reddish sediments can be traced northward on a seismic profile until it disappears before reaching Site 1109 (Fig. F25). Geophysical logs suggest that the noncored interval at Site 1118 (above 205 mbsf) records turbiditic and hemipelagic deposition of mainly Pleistocene age.

At Site 1109 very rapid, thick (~250 m) deposition of hemipelagic sediments and turbiditic mud, silt, and minor sand occurred during middle to late Pliocene time at initially upper bathyal then middle to lower bathyal depths. Volcaniclastic sand and silt and mud of turbidite origin became more abundant at middle bathyal depths. Finally, during the Pleistocene, calcareous nannofossil-rich pelagic ooze and calcareous clay were interstratified with volcaniclastic silt, sand turbidites, volcanic ash, and rare calciturbidites.

During early Pliocene time (3.9–3.6 Ma) at Site 1115 there was a transition to a deeper water succession (150–500 m) with rapid deposition (284 m/m.y.) of muds and volcaniclastic sands, mainly by turbidity currents. Deposition continued in an upper bathyal setting at a very rapid depositional rate during middle Pliocene time (3.6–2.5 Ma). Volcanic glass-rich beds and local concentrations of pumice fragments (Fig. F26) are interpreted as ash fallout. Further deepening took place during late Pliocene–Pleistocene time to upper middle bathyal depths, and the overall sedimentation rate decreased to 63 m/m.y. Pleistocene deposition was dominated by nannofossil ooze with volcanic ash (see below), and sedimentation slowed further (34 m/m.y.) after 0.5 Ma.

A counterpart of the Pliocene–Pleistocene successions at Sites 1109, 1115, and 1118 is found at Site 1108, which is very close to the depocenter of the rift basin. The deeper part of the recovered succession is dominantly turbiditic, whereas the upper part is dominated by talus
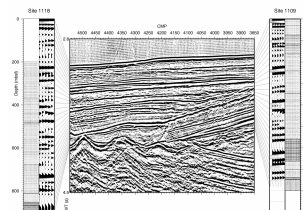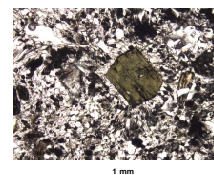
F23. Calcium carbonate vs. depth at Site 1115, **p. 57**.
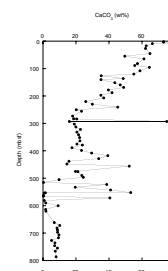
F24. Tuff, with glass shards in glassy matrix, **p. 58**.
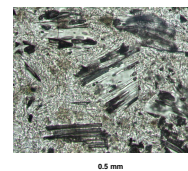
F25. Depth converted multichannel seismic traces at Sites 1118 and 1109, **p. 59**.

F26. Pumiceous rock containing hornblende phenocrysts in glassy groundmass, **p. 60**.

derived from the Moresby Seamount. The recorded sedimentation began in the middle to late Pliocene with rapid deposition (400 m/m.y.) of fine-, medium-, and coarse-grained sandstones, and minor conglomerate, interpreted mainly as deposits from turbidity currents and debris flows. Clasts and mineral grains were derived from basic and acidic volcanic rocks, and to a minor extent from plutonic rocks (including ultrabasic rocks), metamorphic rocks, and neritic carbonates (Figs. **F27, F28**). During the late Pliocene (1.95–2.58 Ma) there was an interval of fine-grained turbidity current deposition, affected by faulting. The turbiditic sediments were followed by emplacement of talus (as much as ~50 m thick) comprised of angular clasts of mainly metadolerite of possible ophiolitic provenance, for which the obvious source is the Moresby detachment fault system. Finally, during the late Pleistocene deposition was relatively slow (15 m/m.y.) with accumulation of calcareous, nannofossil-rich clay with minor silt and sand, including volcanic ash.

A small amount of Pleistocene sediments was also recovered at Sites 1111, 1112, and 1113. Data on turbidites and other inferred mass-flow deposits from Site 1110 record deep-water Quaternary sedimentation in a setting of extreme sediment instability. Metamorphic clasts are most likely to be talus deposits derived from the nearby Moresby Seamount. At Site 1111 individual clasts of igneous, metamorphic, and rare sedimentary rocks were recovered. At Site 1112 there was minor recovery of talus of mainly metamorphic rocks intercalated with clay and silty clay, silt and sand, and several volcanic ash beds.

Footwall Sites

Sedimentary evidence from the footwall sites (Sites 1114 and 1116) on the Moresby Seamount was limited by poor recovery, incomplete logging data, and imprecise dating (Fig. **F21**).

At Site 1114 the recovered section comprises classical turbidites, mud turbidites, and paraconglomerates possibly deposited by high-density turbidity currents, or debris-flow deposits, that accumulated at middle bathyal depths (500–2000 m) during middle to late Pliocene time at an average sedimentation rate of >176 m/m.y. for the entire succession (Fig. **F10**). The sediment was apparently derived from calc-alkaline, metamorphic, and possibly ophiolitic sources.

At Site 1116 Pleistocene sediments are absent, and the deep-water succession is dominated by coarse-grained turbidites, debris flows, and fine-grained deposits with a minor input of shallow-water carbonate. The whole of the recovered succession accumulated during middle late Pliocene time at middle bathyal depths (500–2000 m) at an average sedimentation rate of >70 m/m.y. (Fig. **F10**). The provenance of sediments at Site 1116 was again mainly from a calc-alkaline arc terrane, with a minor metamorphic (Fig. **F29**) and possibly an ophiolitic contribution.

In summary, the overall sedimentary regime at Sites 1114 and 1116 is consistent with a relatively proximal rift setting. By contrast, sediments in the hanging wall sites were more distally derived, with a variable volcanogenic input, as summarized below.

History of Volcanism

The presence of volcanogenic ash layers in the sediments at Sites 1118, 1109, and 1115 is displayed in terms of thickness and number of volcanogenic ash layers per million years for the Pliocene–Pleistocene time (Fig. **F17**). Only one volcaniclastic ash layer was recovered in the middle Miocene section and none from the latest middle Miocene to
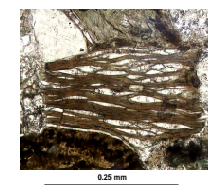
F27. Basalt clast with plagioclase and biotite microphenocrysts in calcitic matrix, **p. 61**.
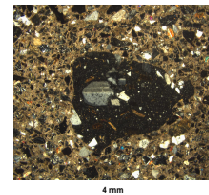
F28. Basalt clast with plagioclase microphenocrysts and acidic and serpentinite clasts within a calcareous matrix, **p. 62**.
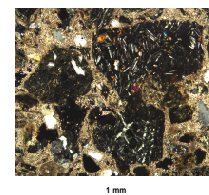
F29. Calc-schist fragment surrounded by basalt and silicic fragments in calcite cement, **p. 63**.

earliest Pliocene time interval. The probable source of the volcanic ash was the Trobriand Arc, including former volcanoes in the Amphlett Islands and Equm Atoll.

The volume of ash fallout layers is volumetrically minor compared to the supply of volcaniclastic turbidites. However, the presence of numerous ash fallout layers indicates that explosive volcanism, possibly related to continental arc rifting, did take place during Pliocene–Pleistocene time. These volcanic ash interbeds are composed of rhyodacitic to rhyolitic bubble-wall shards and highly vesicular and pipe-vesicular shards with minor phenocrysts. By contrast, the volcaniclastic component consists of brown and colorless glass shards, crystals of plagioclase, quartz, biotite, amphibole, pyroxene, and opaque minerals. Phenocrysts may reach up to 50% by volume of the sediment.

The temporal and spatial distribution of the recovered ash is quite variable (Fig. F17). In the sediments from the early to middle Pliocene transition (3.5–3.6 Ma), volcaniclastic ash layers are particularly abundant at the southernmost site, Site 1118, with 100 layers and a thickness of 8.7 m per 0.1 m.y. By comparison, the frequency at Site 1115 peaks at 10 layers per 0.1 m.y. and at Site 1109 at 15 layers per 0.1 m.y. Several layers of middle to late Pliocene age with abundant volcanogenic material (mainly volcaniclastic) were recovered at Site 1118, in contrast to Site 1109 and Site 1115, where only minor input was dominated by air-fall silicic ash. A prominent episode of mainly volcaniclastic sedimentation took place at Site 1109 in early Pleistocene time, but this was not recorded in the sediments at Site 1115 further north. Finally, the Pleistocene section at both Sites 1109 and 1115 was marked by abundant, dominantly silicic, air-fall ash of platy and bubble-wall types indicative of explosive volcanism.

Erosion Estimates

Porosity profiles reflect a combination of loading history, lithologic effects (e.g., differences in grain size, grain shape, mineralogy, strength, etc.), and chemical effects (e.g., degree of pore filling by cementation and permeability differences that affect dewatering rates). Typically, seafloor porosities of marine oozes are high (70%–80%). For homogeneous sediments that are not overpressured, porosity loss with depth follows an exponential law (e.g., Terzaghi, 1925; Athy, 1930).

As shown in Figure F11A, porosity data from Sites 1109, 1111, 1115, and 1118 show a widely scattered, but consistent downhole trend, which starts at ~70%–80% seafloor porosity and then decreases exponentially to values between ~30% and ~55% at ~700 mbsf. Other than ~120 k.y. of missing sediment at the top of Site 1115, no obvious hiatuses have been noted above the regional unconformity for the sedimentary record recovered from these sites. In contrast, porosity data from Sites 1108, 1114, and 1116 differ remarkably from the above trend, ranging from ~15% to ~45%, although the boreholes were rather shallow (~150 to ~485 mbsf). These anomalously low porosities may reflect erosion of overlying material, although other factors such as cementation may also contribute.

The thickness of eroded material was estimated at these sites by using a regression least-squares exponential fit to the data from each site (e.g., Athy, 1930). The estimates regarding the thickness of removed deposits are ~400 m at Site 1108, ~220 to >400 mbsf at Site 1114, and ~960 m at Site 1116 (see Table T2). However, the limited amount of data and poor curve fits reduce the reliability of these estimates.

T2. Estimated thickness of removed sediments, p. 76.

In a second approach presented here, porosity profiles from Sites 1108, 1114, and 1116 are compared to the range shown by data from the non- (or minor-) erosion sites (Fig. F11B). This approach assumes that the lithologies and compaction histories of the sites allow them to be used as references for Site 1108 in the graben and for Sites 1114 and 1116, now uplifted on the Moresby Seamount. This comparison indicates that porosities at Sites 1108, 1114, and 1116 correlate to much deeper sections of the low-erosion sites (Fig. F11B) and the data were shifted in depth to obtain a reasonable visual fit. Site 1108 porosity data were shifted 500 m above 165 mbsf, and 700 m below 165 mbsf. The additional 200 m of removal is because of faulting. Similarly, 750 m of erosion was applied to the upper part of the sedimentary succession at Site 1114, resulting in a broad agreement of the data with that from the "reference" sites. Finally, porosities from Site 1116 were shifted down 1000 m (Table T2).

In summary, consistent results were obtained for Sites 1108 and 1116 using the two methods, but at Site 1114, the application of an exponential relationship yielded a significantly lower amount of sediment removed relative to that estimated by the comparison of these sites to the "reference" sites. One possible explanation is that the second approach overestimates erosion where fluid-enhanced cementation, as suggested from filled veins at Site 1108 or 1114, contributes to the low porosities observed. Proximity to active fluid flow along fault zones may cause these sites to be preferentially cemented.

Magnetic Susceptibility Intersite Correlation

Magnetic susceptibility reflects changes in magnetic mineralogy (e.g., lithologic variations) and was obtained routinely as part of the multisensor track (MST) measurement of sediment cores from Sites 1108, 1109, 1114, 1115, 1116, and 1118. The quality of magnetic susceptibility data commonly degrades from APC- to XCB- to RCB-cored sections because of a combination of reduced core diameter and core fracturing. For these reasons Leg 180 magnetic susceptibility data show considerable scatter.

Intersite correlations are based on recognizing characteristic features in the magnetic susceptibility data sets. For Sites 1118, 1109, and 1115, a first-order difference exists between a consistently high-amplitude susceptibility zone within the upper part of the stratigraphic section and a lower zone identified by a dramatic decrease in susceptibility amplitude (Fig. F12). This high-/low-amplitude combination is found within the turbidite units that characterize much of the basin infill. The magnetic susceptibility profiles shown in Figure F12 have been aligned relative to the top of the Mammoth polarity event, a datum recognized at both Sites 1115 and 1118. In general, the high-amplitude susceptibility zone correlates with the presence of high-frequency, clayey silt/silty clay turbidites. In contrast, the low-amplitude magnetic susceptibility zone relates to high-frequency, silty, and, on occasion, sandy turbidites. Lithologically, these differing clay- and silt-dominated turbidite units have been termed distal and proximal, respectively. By using the paleontologic- and paleomagnetic-determined sedimentation rates for each site, it is possible to display the magnetic susceptibility as a function of time (Fig. F13). This format removes the effect of varying sedimentation rate between sites. Within the accuracy of the age determinations (100–200 ka), it would seem that the transition between the first-order low- and high-amplitude magnetic susceptibility variation is coeval

between the sites. Second-order trends are represented by the relatively high amplitude magnetic susceptibility variations that occur at the base of each stratigraphic succession.

Explaining the origin of the magnetic susceptibility variations within and between the Leg 180 sites remains enigmatic. Although the magnetic susceptibility generally correlates with the remanent magnetization intensity, there is no simple relationship with either grain size, main lithologic boundaries, and/or gamma-ray count. A general correspondence does exist between magnetic susceptibility and remanent magnetic intensity, indicating a common magnetic mineralogy. However, X-ray diffraction failed to identify this mineralogy although the high remanent intensities suggest that magnetite is the dominant mineral with respect to the remanence. Ferromagnesium-rich clays such as smectite and, less frequently, chlorite, are likely important contributors to the magnetic susceptibility.

The mixing between magnetic and nonmagnetic clays and sands, in addition to the approximately synchronous change in magnetic susceptibility character across the sites, implies sediment input and mixing from multiple provenances.

Petrology of the Dolerites and Gabbros

Apart from clasts and crystals in volcanogenic sandstones and a few clasts of hornblende basalt at Site 1116, dolerites, metadolerites, and quartz gabbros were recovered at Sites 1108, 1109, 1110–1114, 1117, and 1118. Several conclusions have been drawn from preliminary analyses of these rocks:

1. Ubiquitous dolerite and some gabbro (Fig. **F18**) occur on both the footwall and the hanging wall of the detachment. Dolerite is the major rock type in the upper levels of the basement of Moresby Seamount.
2. Preliminary chemical comparison shows similar major and trace element compositions in the dolerite and gabbro from the seamount sites (Sites 1114 and 1117) and the dolerite from Site 1118. All of these differ from the Site 1109 dolerite, which is generally less altered. The relationship between these units is not yet clear, but further chemical evidence may provide clarification to provenance, as may dating the time(s) of their formation.
3. Close to the major faults at Sites 1114 and 1117 on the footwall of the Moresby detachment, the rocks underwent a similar history of deformation, metamorphism, and alteration. Metamorphism of these rocks has progressed from the formation of foliation and veining. Subsequently, these structures were refolded and subjected to greenschist facies conditions and hydrothermal alteration. A final phase of brittle deformation is shown by fractures filled with quartz and calcite.

Figure **F30** shows average values of major and trace elements from Sites 1114, 1117, and 1118 normalized to the average for Site 1109, which, on petrographic evidence, is the freshest of the sites. The patterns are remarkably consistent, showing very little variation except for K_2O, Rb, and Ba. Because these are all well-known mobile elements, it is tempting to ascribe this variation to the effects of alteration, either by weathering or hydrothermal activity. The rocks from Site 1118 are the most affected by weathering, on the basis of the core descriptions that

F30. Major and trace element data for dolerites and metadolerites, Sites 1109, 1114, 1117 and 1118, **p. 64**.
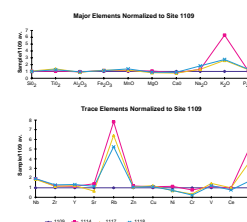
record extensive formation of red iron oxides, but may also have suffered some hydrothermal alteration. As this site diverges least from the values from Site 1109, we conclude that the variations shown are most likely caused by metamorphism and hydrothermal alteration, especially as these variations are most marked at Site 1114. Small variations, especially in Ni, Cr, and V can probably be ascribed to different amounts of igneous fractionation as seen at Site 1118.

Figure F31 shows plots of major and trace elements of variably altered rocks at Sites 1108, 1111, and 1114 normalized to values for Site 1109 (i.e., the least altered samples). The samples plotted here are specifically chosen to reflect varying degrees of alteration. The samples were arranged in order of decreasing loss on ignition (LOI), as a first-order index of alteration. Encouragingly, Site 1109, judged to be the least altered, had also the lowest loss on ignition. This method of plotting the results shows unequivocally that these samples have gained K_2O, Rb, and Ba relative to Site 1109. Also, the order of increase for all the elements is consistent. Thus, the foliated metadolerite from Site 1114 is the most enriched, followed by the foliated epidote-rich schist, then by the nonfoliated dolerite and the nonfoliated metadolerite, and finally by the metadolerite pebble from Site 1108. This is not the order of LOI, but this may not be too significant. Petrographic evidence shows that the metadolerite from Site 1108 has suffered low-temperature alteration, which has altered the feldspars, while other samples show epidote growth indicative of more drastic mineralogical changes. As an increasing degree of enrichment is related to increasing signs of metamorphism on the basis of, among other things, epidote growth, we conclude that the enrichments shown in Figures F30 and F31 are caused by hydrothermal effects associated with greenschist facies metamorphism. On the evidence from Site 1117, we propose that this metamorphism and chemical alteration have taken place adjacent to fault zones in the presence of fluids channeled by these faults, which have facilitated the metamorphism and hydrothermal alteration.

Data shown in Figure F32 suggest that the Leg 180 dolerites and gabbros are remarkably similar to enriched mid-ocean ridge basalt (E-MORB), with the exception of the elements noted as deviating in the two previous figures, and Ba and Ce are rather surprisingly below the values for E-MORB at all localities. The simplest explanation for this is that Ba is intrinsically low in these samples, as is Ce, suggesting that a better comparison may be with normal- (N-) MORB. This is especially true for Site 1109, which is the least altered of the Leg 180 sites. The other sites have higher Ba because of alteration, as noted above, but never quite reach E-MORB levels. Barium is strongly enriched over N-MORB levels in island arc related lavas and is one of the elements that distinguishes the two (e.g., in the Lau Basin; Hergt and Farley, 1994). Because the Leg 180 dolerites and gabbros have been subjected to varying degrees of Ba enrichment, but have still not reached E-MORB levels, the shipboard geochemical data do not show evidence of a subduction-related signature.

Faulting at Moresby Seamount and on the Flexured Margin

The most spectacular tectonic structure encountered during Leg 180 is the Moresby detachment fault, which dips 25°–30° toward the north-northeast (Fig. F4). At Site 1117, where the fault plane crops out on the

F31. Major and trace element data for dolerite and metadolerite from talus samples at Sites 1108, 1111, and 1114, p. 65.
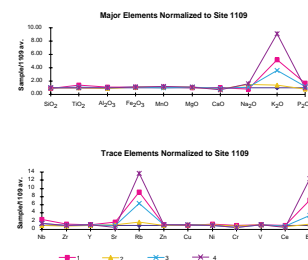
F32. Major and trace elements of dolerites and metadolerites from Sites 1108, 1109, 1111, 1114, 1117, and 1118 normalized to E-MORB, p. 66.
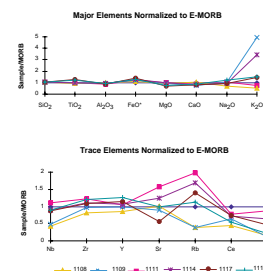
northern flank of Moresby Seamount (Fig. F6), we drilled an ~100-m-thick succession of deformed rocks above a basement of undeformed gabbro (Fig. F21). From bottom to top, the gabbro ranges from undeformed (Fig. F18) to brecciated to mylonitic with a well-developed foliation with S-C structures (Fig. F20). Epidote and quartz dominate the secondary minerals, indicating syntectonic greenschist facies conditions. Above this, a fault gouge (Fig. F19) several meters thick crops out on the seafloor and represents the most advanced stage of deformation with evidence for fluid-assisted alteration to produce serpentinite, chlorite, talc, calcite, ankerite, and fibrous amphibole.

By contrast, at Site 1114 a south-southwest–facing normal fault offsets the basement by ~2 km near the crest of the seamount. At Site 1114 a 6-m-thick tectonic breccia lies above a basement of metadolerite. We thus infer a much larger displacement and more extreme P-T conditions along the Moresby detachment fault. One other large normal fault was penetrated at 165 mbsf at Site 1108 within the rift basin. This fault, for which the dip direction could not be determined aboard ship, is revealed mainly by well-developed scaly fabric. It has a vertical offset of ~200 m, which is based on offsets in sediment age, porosity, pore-water chemistry, and temperature vs. depth curves. Otherwise, the observed normal faults have minor offsets and correspond to high level brittle faulting.

At all sites, dip-slip normal faults are predominant but usually coexist with both oblique- and strike-slip faults. The proportion of strike-slip faults markedly increases from the northern sites toward the Moresby Seamount (Fig. F33), in agreement with probable oblique motion on west-northwest–trending normal faults that affect the seamount. This oblique motion, inferred to be left lateral, is in agreement with the north-south extension deduced from earthquake fault plane solutions (Abers, 1991; Abers et al., 1997) and GPS measurements (Tregoning et al., 1998).

Thermal Gradients

Estimates of thermal gradient were obtained at five sites during Leg 180 (Fig. F34). The most reliable estimates were from Sites 1109 and 1115 (31° and 28°C·km^{-1}, respectively), where in situ data were collected from multiple Adara temperature tool and Davis-Villinger temperature probe (DVTP) deployments. At Site 1111, two in situ DVTP deployments were made, which were supplemented by an open-hole measurement that was used to extrapolate in situ temperature. Results suggested natural or drilling-induced influx of seawater at shallow depths, with a large-scale thermal gradient of 95°C·km^{-1}, based on the mudline temperature and a reliable DVTP estimate at 136.5 mbsf.

Thermal estimates from Sites 1108 and 1118 were obtained solely from open-hole temperature surveys in which data were collected at several depth stations. Measurements from Site 1108 were obtained with the Adara tool on the wireline, whereas Site 1118 data were collected with the temperature tool (TLT) on the logging string. Results from Site 1108 suggest a thermal gradient of 100°C·km^{-1}, but the profile suggests possible disruption because of recent faulting or fault-related fluid flow. Results from measurements at Site 1118 yield an approximate thermal gradient of 60°C·km^{-1}. However, this estimate was based on only the mudline temperature and one extrapolation at 834 mbsf, and evidence suggests influx of warm fluid at ~700 mbsf. Overall, tem-

F33. Cross section showing increasing proportion (in pie charts) of strike-slip and oblique-slip faults toward Moresby Seamount, p. 67.
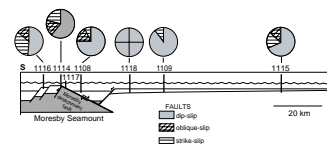
F34. Thermal gradients (in °C·km^{-1}) from Leg 180, p. 68.
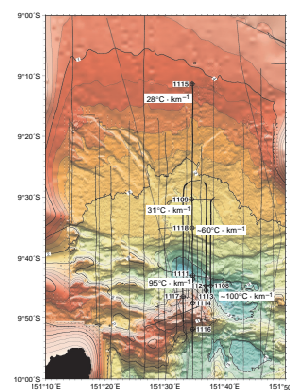
perature measurements indicate a trend of increasing thermal gradients toward the graben to the north of Moresby Seamount.

Interstitial Pore-Water Geochemistry and Sediment Diagenesis

The inorganic geochemistry sampling program during Leg 180 focused in large part on the acquisition of high-resolution pore-water profiles at Sites 1109, 1115, and 1118. Data from these three northern sites provide a basis for evaluating sediment diagenesis in the Woodlark Rise on a regional basis.

Although notable differences exist between the three sites, similar trends in various portions of the profiles of interstitial water (IW) constituents at Sites 1109, 1115, and 1118 indicate that many of the same diagenetic processes mediate the pore-water composition throughout sediments of the Woodlark Rise. The IW chemistry is most similar at Sites 1109 and 1115, with these two sites displaying greater differences with respect to the southernmost Site 1118.

Concentrations of IW constituents in the upper portions of all holes reflect the oxidation of organic matter mediated by microbial activity and the concomitant early diagenesis of biogenic carbonates. This is reflected in extensive SO_4^{2-} depletion and NH_4^+ production (see below) in the younger sedimentary sequences section of each site. The upper 500 m at Site 1109 is most similar to the upper 700 m at Site 1118 in this regard, whereas the sediments of the thick onlap sequence at Site 1118 represent an expanded version of part of the section cored at Site 1109. Specific reactions thought to occur include dissolution of aragonite and recrystallization into low-magnesian calcite. The dominant lithologies and mineralogies at all three sites support this inference. The alteration of volcanic matter and clay-mineral diagenesis also occurs at all three sites, albeit to a varying extent. The profiles of dissolved Ca^{2+}, Mg^{2+}, and SiO_2 shown in Figure **F15** reflect a combination of carbonate diagenesis and alteration of volcanic matter. Volcanic alteration and clay-mineral authigenesis typically increase in importance deeper in the sedimentary sequences of each hole. At each site, volcanic ash layers as well as volcaniclastic sands disseminated in carbonates are altered, leading to enrichment of SiO_2 and Ca^{2+} in the pore fluids, whereas the precipitation of various authigenic minerals (e.g., chlorite, smectite, and zeolites) leads to a decrease in the concentration of Mg^{2+} and other pore-water constituents such as K^+ and Na^+. Conversion of pre-existing detrital clays, such as illite interlayering into smectite, also contributes to depletion of K^+ downhole.

The differences between the three sites are often attributable to differences in the thickness and/or the presence of different lithologies at one site relative to the other. Paramount among these are the existence of a lagoonal/brackish water to freshwater transitional sediment sequence overlying dolerite at the bottom of Site 1109, a connectivity between the forearc sediment sequence and the synrift sediments at Site 1115, and the absence of this transitional lagoonal/brackish water to freshwater sequence at Site 1118. A marked limestone/coarse sandstone neritic sediment sequence at Site 1118 imposes important constraints on changes in the pore-water chemistry at this site. The elevated dissolved SiO_2 (and also Li^+ and Sr^{2+}) concentrations deep at this site likely reflect the alteration of the volcanic matter under a higher temperature regime than existed at Sites 1109 and 1115.

The chemical composition of the IW in the sediments of the Woodlark Rise is influenced by a series of sedimentary diagenesis reactions. The alteration of volcanic matter whether as ash layers or dispersed throughout the sediments, carbonate recrystallization reactions mediated by the microbially driven oxidation of organic matter, as well as silicification reactions, all contribute to the observed profiles of pore-water constituents.

Bacterial Activity and Hydrocarbon Generation Biogeochemical Cycling in the Northern Sites (1109, 1115, and 1118)

Bacteria play a dominant role in the degradation of organic matter in sediments and, as a consequence, drive chemical changes and diagenesis. Although the existence of a deep bacterial biosphere in marine sediments has only recently been established (Parkes et al., 1994), the activity of bacteria at depths to 750 mbsf and their direct involvement in geochemical changes have been demonstrated.

Bacteria were present in all samples analyzed at all three of the deep northern sites drilled during Leg 180 (Sites 1109, 1115, and 1118 [Fig. F14]). Near-surface bacterial populations are similar to those at other sites with similar overlying water depths and near-surface organic carbon concentrations. Population numbers decrease rapidly with increasing depth and conform to the general model for bacterial distributions in marine sediments of Parkes et al. (1994), although in the deeper, more indurated sediments from Leg 180 there is an indication that numbers are decreasing more rapidly than the model predicts, resulting in a sigmoidal depth distribution (Fig. F14A).

The activity of deep subsurface microbial populations is evident in geochemical data from these sites (Fig. F14B–D). Pore-water sulfate concentrations are depleted in the uppermost sediments, below which methane concentrations increase rapidly as methanogenic bacteria gain a competitive advantage over sulfate-reducing bacteria for common organic substrates. Biological decomposition of organic matter is also evident from the accumulation of ammonia in pore waters.

At Site 1118, below ~700 mbsf, an increase in pore-water sulfate concentrations, probably associated with lateral fluid flow, is associated with a rapid drop in methane concentrations (two orders of magnitude in one core; Fig. F14B). This constitutes compelling evidence for continuing microbiological activity in the deep subseafloor environment.

In contrast, at Site 1109 sulfate concentrations were depleted to 0 by 107 mbsf, and remained very low throughout the rest of the depth profile (Fig. F14C). The pore-water ammonia profile shows two distinct peaks, the uppermost of which is associated with a peak in bacterial numbers (Fig. F14A) and is clear evidence of bacterial organic matter degradation. The second peak in ammonia was associated with an increase in alkalinity (data not shown) reflecting continued microbiological activity at depth.

At Site 1115, there are distinct minima in both methane and ammonia depth profiles around ~520–580 mbsf (Fig. F14D). These suggest two separate zones of peak bacterial activity that are separated by the regional unconformity at 572 mbsf.

Hydrocarbon Generation at Site 1108

At Sites 1109, 1115, and 1118, C_1/C_2 ratios remain between 10^3 and 10^4 throughout the holes, reflecting the biological origin of methane (Fig. **F14E**). At Site 1108, methanogenesis was biological in origin in the uppermost sediments, with a dramatic increase in methane concentrations below the depth of pore-water sulfate depletion. However, increasing quantities of ethane with increasing depth cause a decrease in the C_1/C_2 ratio (Fig. **F14E**). Below ~100 mbsf small quantities of ethane and propane were present in the headspace gas samples; their concentrations increased with depth. Furthermore, below ~400 mbsf traces of branched and straight-chain C_4 and C_5 components were also detected. The accumulation of $>C_1$ hydrocarbons and the concomitant decrease in C_1/C_2 ratio confirm a thermogenic gas input to the sediments. The presence of thermogenic gas at shallow depths is consistent with the high thermal gradient at Site 1108 (~100°C·km^{-1}) and the thick sedimentary section in the rift basin. Pollution and safety concerns, therefore, prevented us from deepening this site.

Implications for a Deep Bacterial Biosphere in Marine Sediments

The continued presence of bacterial populations at more than 800 mbsf is of fundamental significance. The persistence of microbial life into indurated sedimentary rock adds to a steadily growing body of evidence for a more extensive biosphere than previously imagined. Microbes live in high-temperature regions of the lithosphere (e.g., oil reservoirs, aquifers, iron-rich ores, ocean rifts, and hot springs; Brock, 1985) and even into basalt (Furnes et al., 1996; Giovannoni et al., 1996), and granites (Pedersen and Ekendahl, 1990). Bacteria are known to grow at temperatures to ~120°C (Stetter et al., 1993) with indirect evidence for the existence of cells approaching 400°C at abyssal depths (Deming and Baross, 1993) and at pressures of over 1000 atmospheres. The bacterial biosphere in deep-marine sediments may be conservatively equivalent to about 10% of the surface biosphere (Parkes et al., 1994). Recent advances have made significant inroads into understanding both energy sources (e.g., Wellsbury et al., 1997) and electron acceptors (Lovley et al., 1996; Raiswell and Canfield, 1996) for life at "extremes" along with significant improvements in understanding the diversity and physiology of microbial life in deep-sea sediments. The discovery of the deep bacterial biosphere has extended our perception of life from merely a surface phenomenon, and has profound implications for the biodiversity of our planet, fossil fuel formation, the origins of life on Earth, and the potential for life on other planets.

The limits of life on Earth remain unknown: ODP Leg 180 has provided samples and data that considerably extend our knowledge of the deep-marine component of our biosphere.

Downhole Logging

During Leg 180, four holes were logged by the triple-combo geophysical and the FMS-sonic tool strings, and among these, three were logged for more than 750 m (Table **T3).** This yields ~2.4 km of FMS and classical logs.

Downhole Measurements

Despite rather uniform lithologies for most of the holes, the log response shows significant variability and will therefore prove very useful to correlate the different drilled sequences (Figs. **F35, F36, F37, F38**). For instance, the 200–250 mbsf interval in Hole 1118A shows low gamma ray (Fig. **F35**), low porosity (Fig. **F36**), and high sonic velocities (Fig. **F38**). The same features are observed in Hole 1109D in a narrower interval around 230 mbsf. In both cases, this interval can be correlated with a prominent seismic reflector. However, the closer convergence of the two porosity estimates in Hole 1109D indicates that the corresponding sedimentary unit contains less clay than in Hole 1118A. The brackish environment encountered above the major regional unconformity at 572 mbsf in Hole 1115C and at 773 mbsf in Hole 1109D also displays a characteristic log response in both holes. The sonic velocity logs will be used to interpolate the regional velocity structure and better migrate existing multichannel seismic data.

Formation MicroScanner Images

The FMS images acquired during Leg 180 provided critical information about the detailed stratigraphy and structure of both the hanging wall and footwall drill sites around Moresby Seamount (Figs. **F39, F40**). Excellent quality FMS images were acquired at the three sites on the northern margin (Sites 1109, 1115, and 1118), and at one site near the crest of Moresby Seamount, which penetrated an antithetic normal fault (Site 1114). The FMS images from the northern sites reveal conductive clay and resistive sandy or carbonate-rich interbedded units; centimeter-scale depositional features such as parallel laminae, foresets, and bioturbation; and post-depositional faults and fractures. In particular, FMS images were instrumental in determining the precise depths of important stratigraphic boundaries and the structural orientations of beds and fractures, which could not be precisely determined from core samples alone. Analysis of bed and fracture dips in the FMS images from Site 1114 revealed two distinct dip populations that vary vertically with distance from the south-southwest-dipping antithetic normal fault (Fig. **F40**). Histogram plots of the dip directions and stereonet plots of the strikes were particularly useful in determining the major bed and fracture dip distributions (Fig. **F22**).

Vertical Seismic Profiling, Depth Conversion, and Site Correlation

The VSP experiments were carried out at Sites 1109, 1115, and 1118. The depth range of the recording locations were limited at Sites 1109 and 1115 (effectively to "check shots") but covered 565 m at Site 1118. In conjunction with the VSP experiments, we compiled data of velocity variation with depth using laboratory measurements when sonic velocity data from logging were absent, erroneous (because of washouts), or failed to characterize very thin, high-velocity horizons. The resultant velocity-depth functions were used to depth convert the MCS data immediately adjacent to the boreholes. Check shot information derived from the VSP experiment was used to refine these depth conversions to errors within about 10 m. This will be further refined postcruise.

Depth conversion of the seismic data allows direct correlation of the Site 1109, 1115, and 1118 results with the regional stratigraphy. Figure

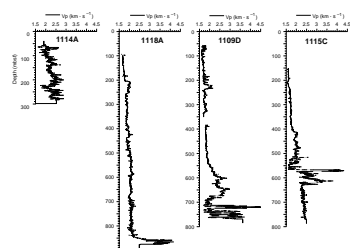F35. Natural gamma ray from Holes 1114A, 1118A, 1109D, and 1115C, **p. 69**.
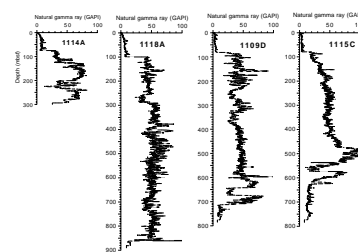
F36. Neutron and density porosity from Holes 1114A, 1118A, 1109D, and 1115C, **p. 70**.
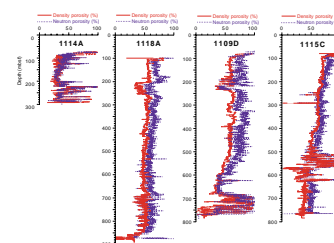
F37. Photoelectric effect in Holes 1114A, 1118A, 1109D, and 1115C, **p. 71**.
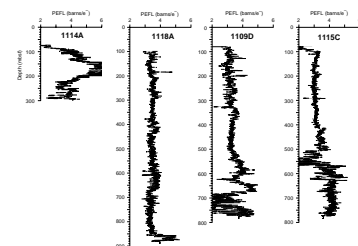
F38. Sonic velocity in Holes 1114A, 1118A, 1109D, and 1115C, **p. 72**.

F25 shows the depth conversions at Sites 1109 and 1118 along with the lithostratigraphic columns. The MCS data in time correlated with depth are shown linking the two sites, which are 8.7 km apart. The limestones and calcareous sandstones close to the base of Site 1118 are thin in comparison to those at Site 1109. These two units, both formed in a neritic environment, fall within a continuous seismic horizon, except that Site 1118 contains only the upper part of the sequence. The interval between 430 and 715 mbsf at Site 1118, corresponding to claystones, siltstones, and sandstones, rapidly thins between common midpoints (CMP) 4075 and 4200, maintaining a conformable relationship with the underlying beds. This interval corresponds to 305–390 mbsf at Site 1109. Volcaniclastic layers are found toward the bottom of the interval at both sites. The reddish claystone and siltstone found between 380 and 430 mbsf at Site 1118 was not seen at Site 1109. Following the corresponding reflectors from Site 1118 toward Site 1109 reveals that this unit pinches out northward between CMP 3950 and 4100 and does not reach Site 1109. The overlying reflectors indicate the possibility of local channel fill above this horizon. Above 385 mbsf at Site 1118 and above ~300 mbsf at Site 1109, the lithostratigraphy is dominated by monotonous silty clays and clayey silts with a middle bathyal origin. However, these horizons correlate well between the two sites.

F39. Dynamically normalized, double pass FMS image from Site 1115 showing horizontal beds characteristic of northern Sites 1109, 1115, and 1118, p. 73.
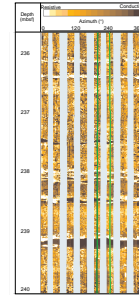
F40. Statically normalized FMS image (left) and tadpole plot (right) from Site 1114, p. 74.
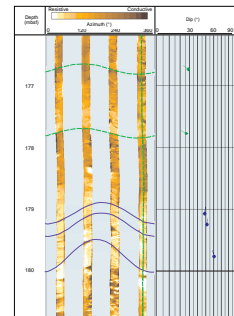
REFERENCES

Abers, G.A., 1991. Possible seismogenic shallow-dipping normal faults in the Wood-lark-D'Entrecasteaux extensional province, Papua New Guinea. *Geology,* 19:1205–1208.

Abers, G.A., Mutter, C.Z., and Fang, J., 1997. Shallow dips of normal faults during rapid extension: earthquakes in the Woodlark-D'Entrecasteaux rift system, Papua New Guinea. *J. Geophys. Res.,* 102:15301–15317.

Athy, L.F., 1930. Density, porosity, and compaction of sedimentary rocks. *AAPG Bull.,* 14:1–24.

Baldwin, S.L., Lister, G.S., Hill, E.J., Foster, D.A., and McDougall, I., 1993. Thermo-chronologic constraints on the tectonic evolution of active metamorphic core complexes, D'Entrecasteaux Islands, Papua New Guinea. *Tectonics,* 12:611–628.

Brock, T.D., 1985. Life at high temperatures. *Science,* 29:132–138.

Davies, H.L., 1980. Folded thrust fault and associated metamorphics in the Suckling-Dayman massif, Papua New Guinea. *Am. J. Sci.,* 280-A:171–191.

Davies, H.L., and Warren, R.G., 1992. Eclogites of the D'Entrecasteaux Islands. *Contrib. Mineral. Petrol.,* 112:463–474.

Deming, J.W., and Baross, J.A., 1993. Deep-sea smokers: windows to a subsurface bio-sphere? *Geochim. Cosmochim. Acta,* 57:3219–3230.

Francis, G., Lock, J., and Okuda, Y., 1987. Seismic stratigraphy and structure of the area to the southeast of the Trobriand Platform. *Geo-Mar. Lett.,* 7:121–128.

Furnes, H., Thorseth, I.H., Tumyr, O., Torsvik, T., and Fisk, M.R., 1996. Microbial activity in the alteration of glass from pillow lavas from Hole 896A. *In* Alt, J.C., Kinoshita, H., Stokking, L.B., and Michael, P.J. (Eds.), *Proc. ODP, Sci. Results,* 148: College Station, TX (Ocean Drilling Program), 191–206.

Giovannoni, S.J., Fisk, M.R., Mullins, T.D., and Furnes, H., 1996. Genetic evidence for endolithic microbial life colonizing basaltic glass/seawater interfaces. *In* Alt, J.C., Kinoshita, H., Stokking, L.B., and Michael, P.J. (Eds.), *Proc. ODP, Sci. Results,* 148: College Station, TX (Ocean Drilling Program), 207–214.

Goodliffe, A., 1998. The rifting of continental and oceanic lithosphere: observations from the Woodlark Basin [Ph.D. thesis]. Univ. Hawaii, Honolulu.

Goodliffe, A.M., Taylor, B., Martinez, F., Hey, R.N., Maeda, K., and Ohno, K., 1997. Synchronous reorientation of the Woodlark Basin spreading center. *Earth Planet. Sci. Lett.,* 146:233–242.

Hegner, E., and Smith, I.E.M., 1992. Isotopic compositions of late Cenozoic volcanics from southeast Papua New Guinea: evidence for multi-component sources in arc and rift environments. *Chem. Geol.,* 97:233–249.

Hergt, J.M., and Farley, K.N., 1994. Major element, trace element, and isotope (Pb, Sr, and Nd) variations in Site 834 basalts: implications for the initiation of backarc opening. *In* Hawkins, J., Parson, L., Allan, J., et al., *Proc. ODP, Sci. Results,* 135: College Station, TX (Ocean Drilling Program), 471–485.

Hill, E.J., 1994. Geometry and kinematics of shear zones formed during continental extension in eastern Papua New Guinea. *J. Struct. Geol.,* 16:1093–1105.

Hill, E.J., and Baldwin, S.L., 1993. Exhumation of high-pressure metamorphic rocks during crustal extension in the D'Entrecasteaux region: Papua New Guinea. *J. Metamorph. Geol.,* 11:261–277.

Hill, E.J., Baldwin, S.L., and Lister, G.S., 1992. Unroofing of active metamorphic core complexes in the D'Entrecasteaux Islands, Papua New Guinea. *Geology,* 20:907–910.

Hill, E.J., Baldwin, S.L., and Lister, G.S., 1995. Magmatism as an essential driving force for formation of active metamorphic core complexes in eastern Papua New Guinea. *J. Geophys. Res.,* 100:10441–10451.

Lister, G.S., and Baldwin, S.L., 1993. Plutonism and the origin of metamorphic core complexes. *Geology,* 21:607–610.

Lovley, D.R., Coates, J.D., Blunt-Harris, E.L., Phillips, E.J.P., Woodward, J.C., 1996. Humic substances as electron acceptors for microbial respiration. *Nature,* 382:445–448.

Mutter, J.C., Mutter, C.Z., and Fang, J., 1996. Analogies to oceanic behavior in the continental breakup of the western Woodlark Basin. *Nature,* 380:333–336.

Parkes, R.J., Cragg, B.A., Bale, S.J., Getliff, J.M., Goodman, K., Rochelle, P.A., Fry, J.C., Weightman, A.J., and Harvey, S.M., 1994. A deep bacterial biosphere in Pacific Ocean sediments. *Nature,* 371:410–413.

Pedersen, K., and Ekendahl, S., 1990. Distribution and activity of bacteria in deep granitic groundwaters of southeast Sweden. *Microb. Ecol.,* 20:37–52.

Raiswell, R., and Canfield, D.E., 1996. Rates of reaction between silicate iron and dissolved sulfide in Peru Margin sediments. *Geochim. Cosmochim. Acta,* 60:2777–2787.

Smith, I.E., and Simpson, C.J., 1972. Late Cenozoic uplift in the Milne Bay area, eastern Papua New Guinea. *Bull.—Bur. Miner. Resour., Geol. Geophys. (Aust.),* 125:29–35.

Smith, I.E.M., 1976. Peralkaline rhyolites from the D'Entrecasteaux Islands, Papua New Guinea. *In* Johnson, R.W. (Ed.), *Volcanism in Australasia:* Amsterdam (Elsevier), 275–285.

Stetter, K.O., Huber, R., Blöchl, E., Kurr, M., Eden, R.E., Fielder, M., Cash, H., and Vance, I., 1993. Hyperthermophilic archaea are thriving in deep North Sea and Alaskan oil reservoirs. *Nature,* 365:743–745.

Stolz, A.J., Davies, G.R., Crawford, A.J., and Smith, I.E.M., 1993. Sr, Nd and Pb isotopic compositions of calc-alkaline and peralkaline silicic volcanics from the D'Entrecasteaux Islands, Papua New Guinea, and their tectonic significance. *Mineral. Petrol.,* 47:103–126.

Sun, S.-S., and McDonough, W.F., 1989. Chemical and isotopic systematics of oceanic basalts: implications for mantle composition and processes. *In* Saunders, A.D., and Norry, M.J. (Eds.), Magmatism in the Ocean Basins. *Geol. Soc. Spec. Publ. London,* 42:313–345.

Taylor, B., Goodliffe, A., Martinez, F., and Hey, R., 1995. A new view of continental rifting and initial seafloor spreading. *Nature,* 374:534–537.

Taylor, B., Goodliffe, A.M., and Martinez, F., 1999. How continents break up: insights from Papua New Guinea. *J. Geophys. Res.,* 104:7497–7512.

Taylor, B., Mutter, C., Goodliffe, A., and Fang, J., 1996. Active continental extension: the Woodlark Basin. *JOI/USSAC Newsl.,* 9:1–4.

Terzaghi, K., 1925. *Erdbaumechanik auf bodenphysikalischer.* Grundlage: Leipzig (Deuticke).

Tregoning, P., Lambeck, K., Stolz, A., Morgan, P., McClusky, S., van der Beek, P., McQueen, H., Jackson, R., Little, R., Laing, A., and Murphy, B., 1998. Estimation of current plate motions in Papua New Guinea from global positioning system observations. *J. Geophys. Res.,* 103:12181–12203.

Weissel, J.K., Taylor, B., and Karner, G.D., 1982. The opening of the Woodlark basin, subduction of the Woodlark spreading system, and the evolution of northern Melanesia since mid-Pliocene time. *Tectonophysics,* 87:253–277.

Wellsbury, P., Goodman, K., Barth, T., Cragg, B.A., Barnes, S.P., and Parkes, R.J., 1997. Deep marine biosphere fueled by increasing organic matter availability during burial and heating. *Nature,* 388:573–576.

Figure F1. Major physiographic features and active plate boundaries of the Woodlark Basin region. The stippled area encloses oceanic crust formed during the Brunhes Chron at spreading rates labeled in millimeters per year. MT and ST = Moresby and Simbo transform faults, respectively; DE = D'Entrecasteaux Islands. Inset, geographical location of the Woodlark Basin.
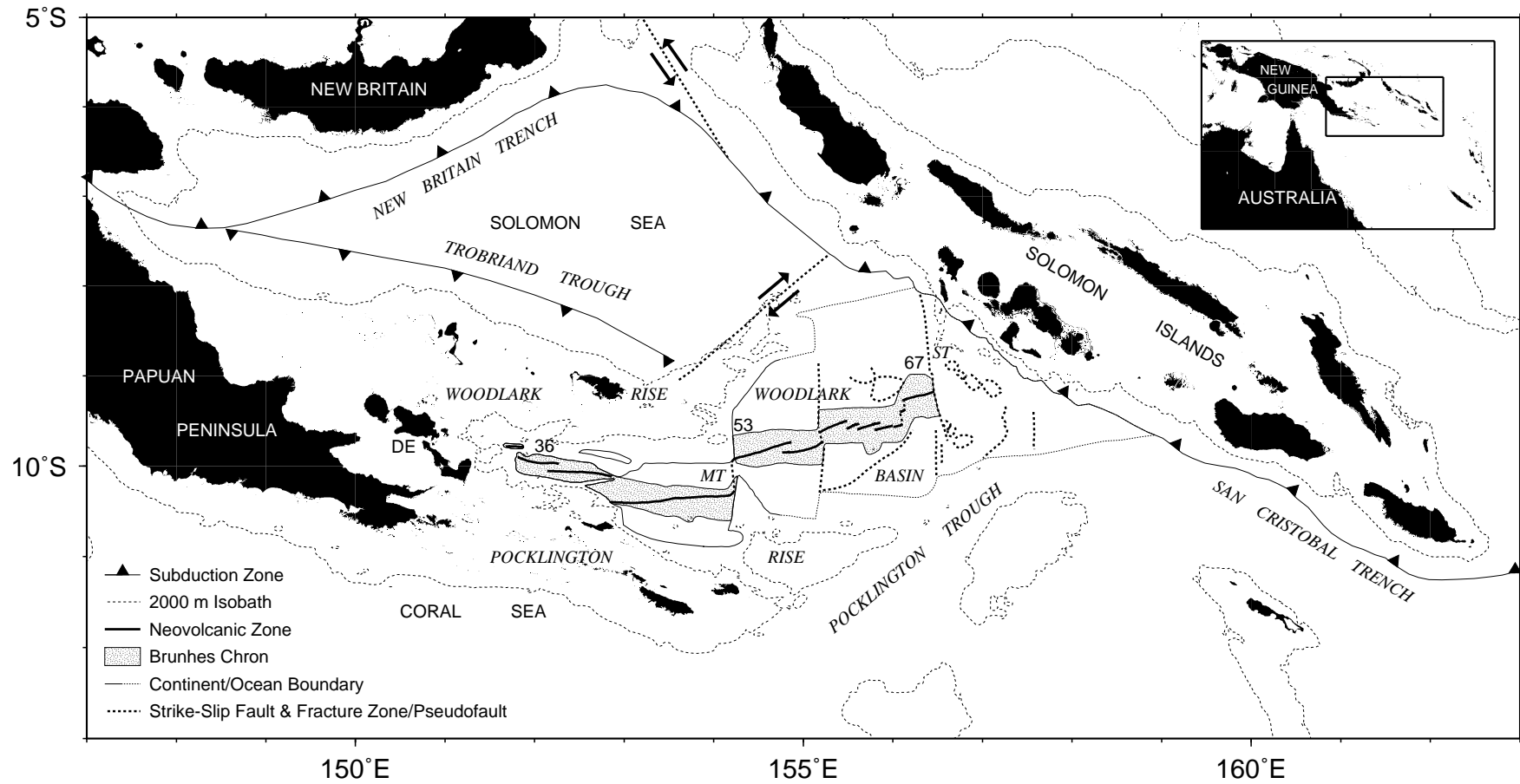
Figure F2. Topography of the Papuan Peninsula and bathymetry of the western Woodlark Basin showing relocated epicenters (solid circles) and earthquake focal mechanisms from Abers et al. (1997). E = Egum Atoll, GB = Goodenough Basin, G = Goodenough Island, F = Fergusson Island, N = Normanby Island, R = Rossel Island, T = Tagula Island, MS = Moresby Seamount, MT = Moresby transform fault, M = Misima Island, W = Woodlark Island. Exploration wells Goodenough-1 and Nubiam-1 are labeled G-1 and N-1. The solid line is the landward boundary of oceanic crust and the thin double lines locate the spreading axes (Taylor et al., 1995).
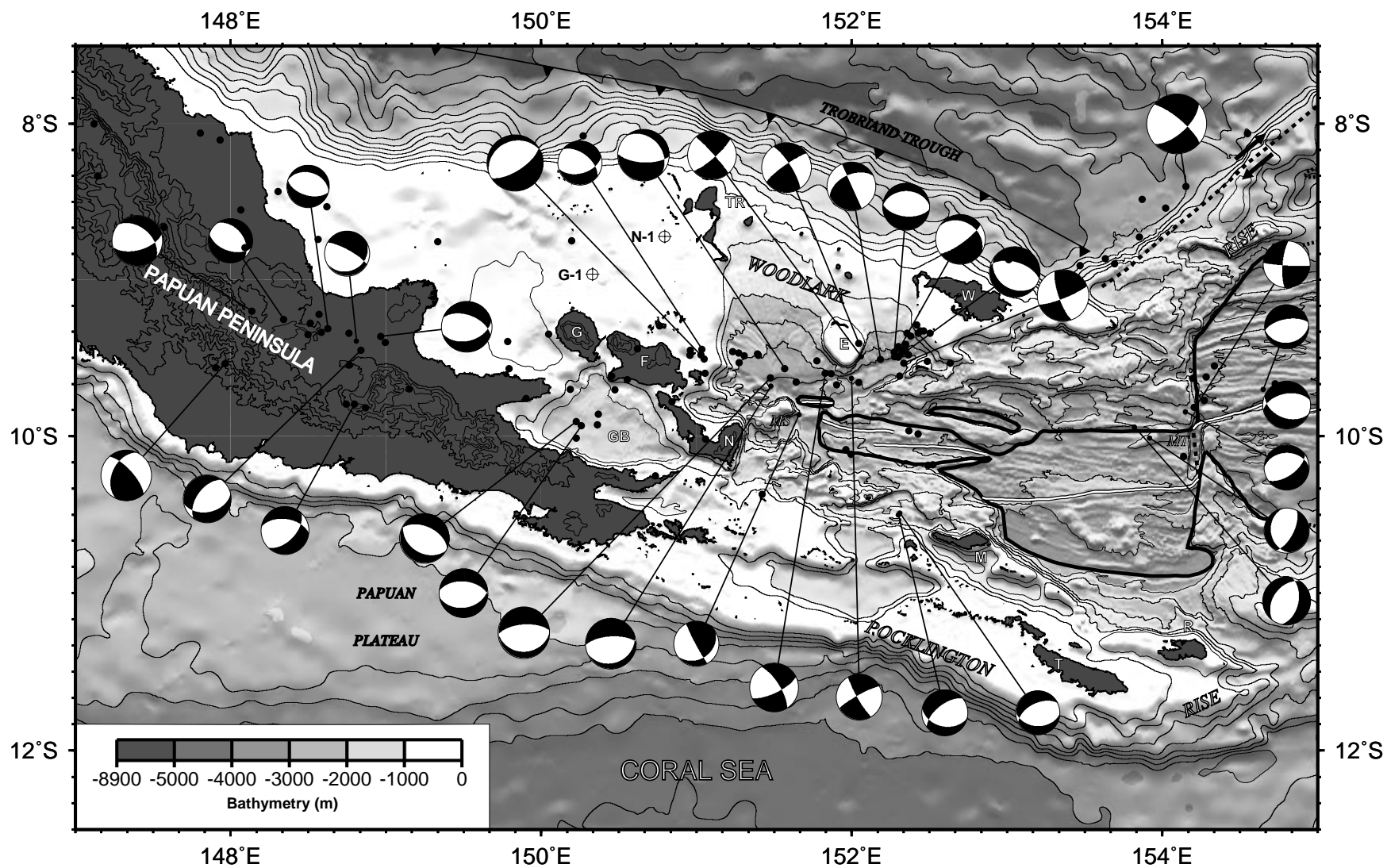
Figure F3. Nested meridional cross sections at 151°34.5′E showing the (**A**) regional bathymetry and (**B**) local structures across the incipient conjugate margins (modified after Taylor et al., 1996). Leg 180 drill sites are projected on the B section. VE = vertical exaggeration; M.S. = Moresby Seamount.
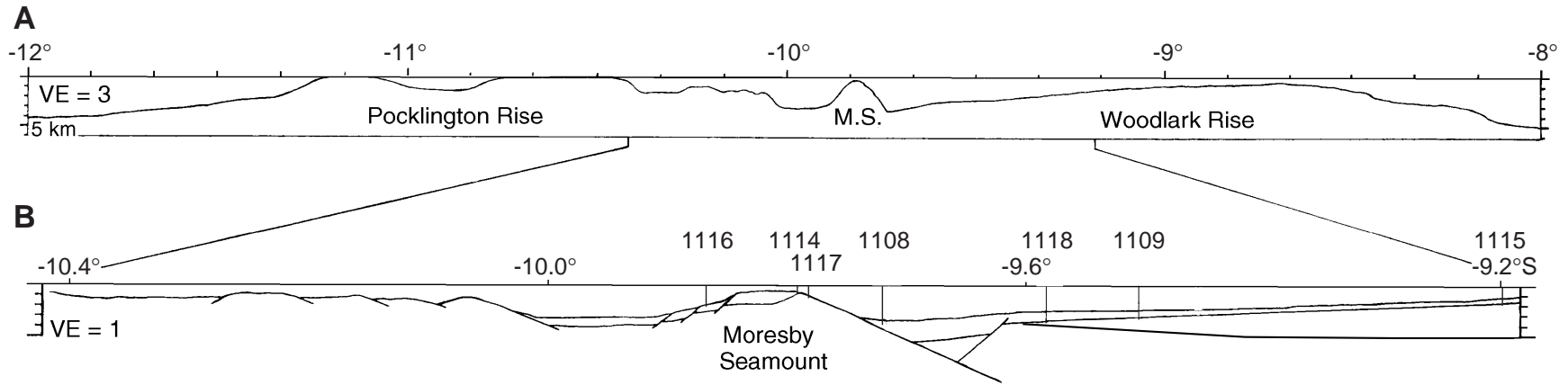
Figure F4. Stacked, migrated, and depth-converted 196-channel (EW95-1369) and 148-channel (EW95-1374) seismic sections on which Sites 1108, 1112, and 1113 were drilled. Seismic data were collected with a 5-km streamer across the rift basin north of Moresby Seamount that is the locus of current deformation ahead of the Woodlark spreading center (the western tip of the neovolcanic zone is hatched in the inset). There is no vertical exaggeration. One hundred common depth points (CDPs) = 1.25 km. The bounding low-angle normal detachment wraps around Moresby Seamount and has a true dip of 27° ± 3° toward 015°. Structure contours from 3 to 9 km depth are shown in the inset, with bathymetric contours labeled in hundreds of meters. The antithetic hanging wall normal fault dips south at 45°. On line EW95-1369 the planar detachment (curvi-planar in three dimensions) is imaged over the full depth extent of the seismogenic zone (3–9 km) determined from earthquake waveform inversion results (Abers et al., 1997). Miocene strata on the southern flank of the prerift forearc basin dip north at ~10° beneath the northern margin. Figure modified from Taylor et al. (1999) to show the location of Sites 1108, 1112, and 1113. **(Figure shown on next page.)**
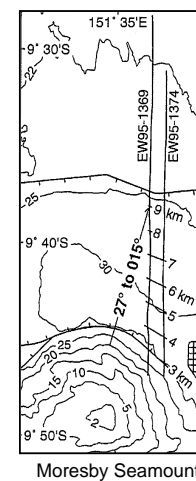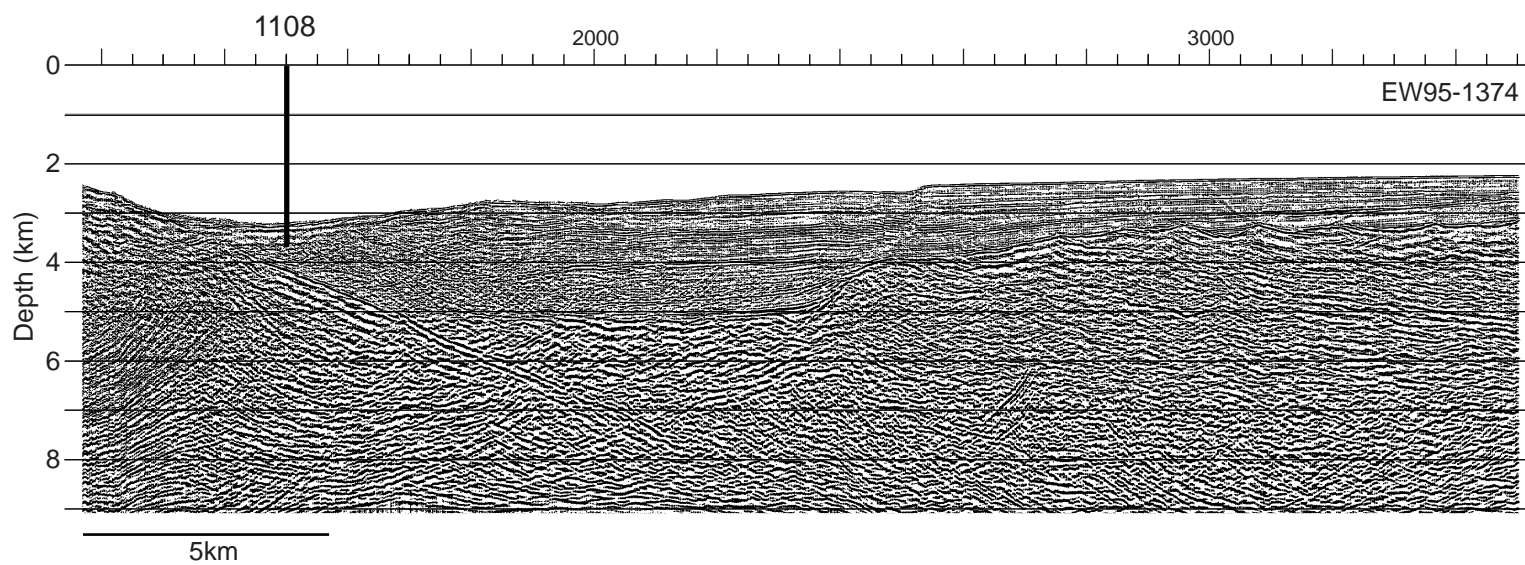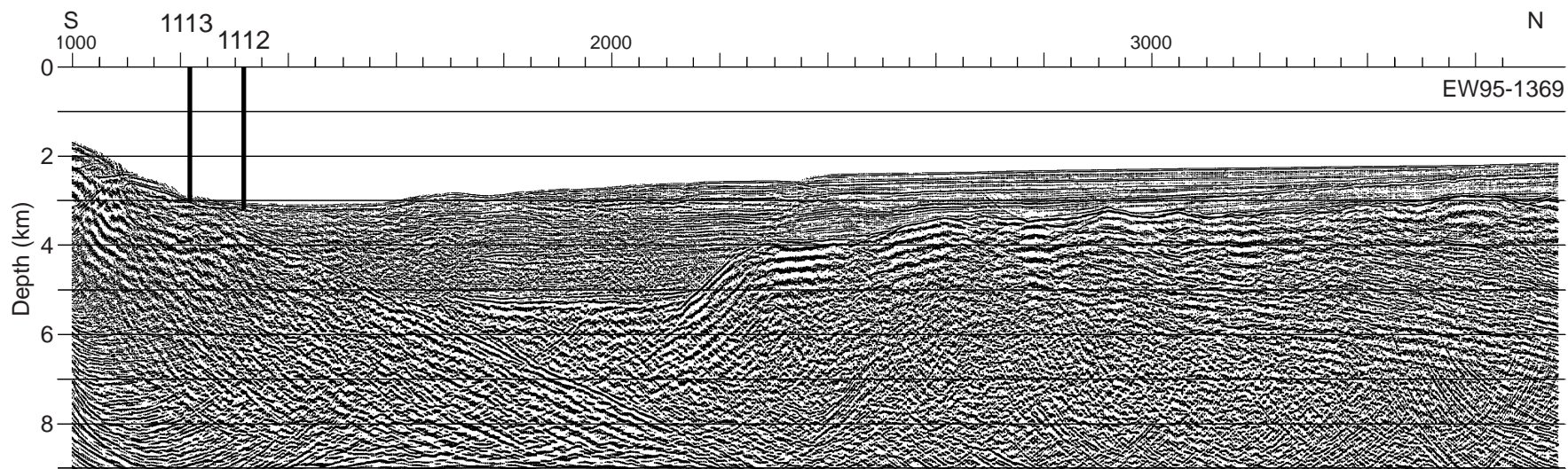
Figure F5. Stacked and migrated time section of 148-channel seismic line EW95-1366, located in Figure F7, p. 39, on which Sites 1109–1111, 1114–1116, and 1118 were drilled. Common depth points (CDPs) are labeled. The top and bottom parts overlap by 100 CDPs (1.25 km).
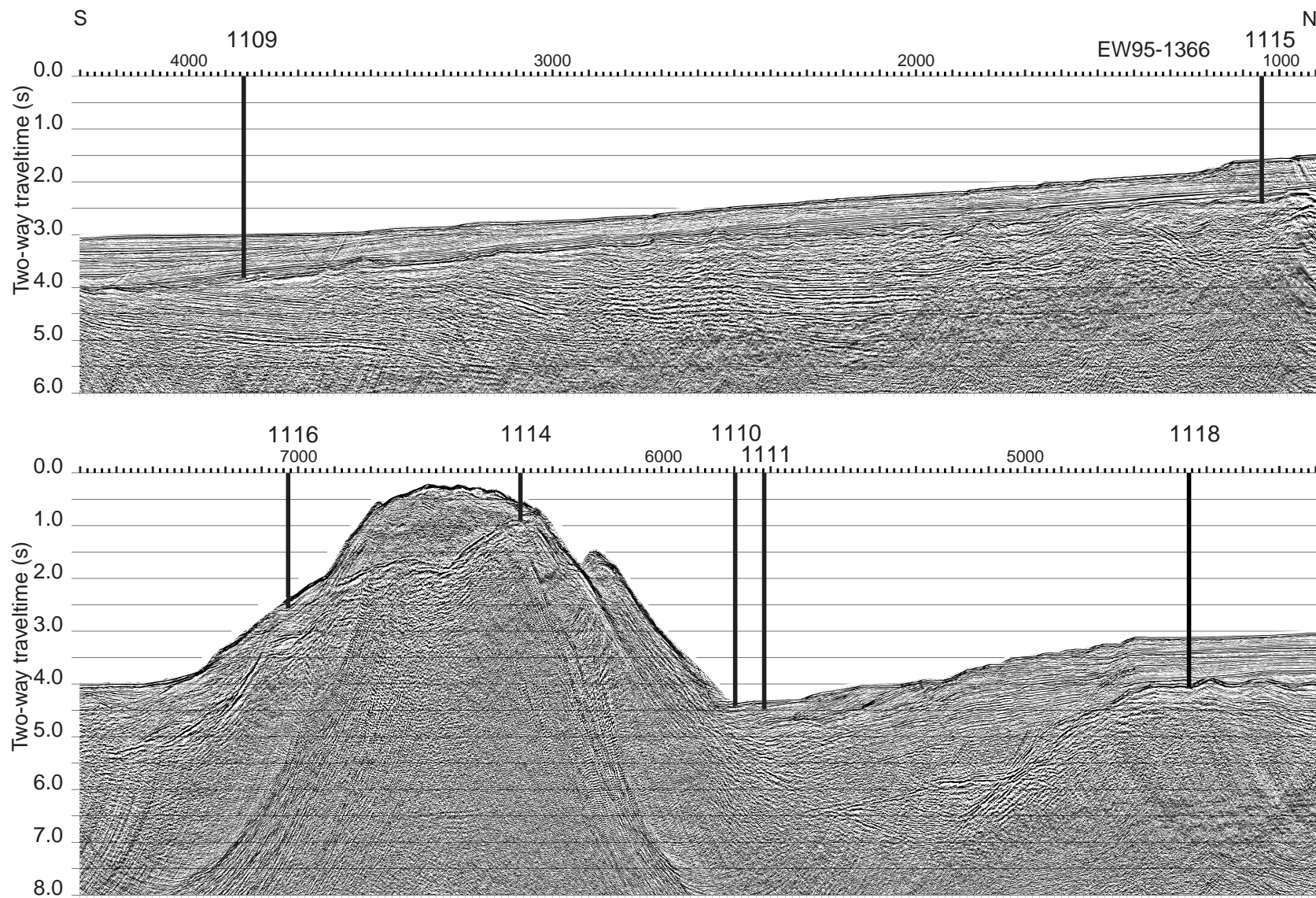
Figure F6. Stacked and migrated time section of 196-channel seismic line EW95-1371, located in Figure F7, p. 39, on which Site 1117 was drilled. CDPs are labeled. Four hundred CDPs = 5 km.
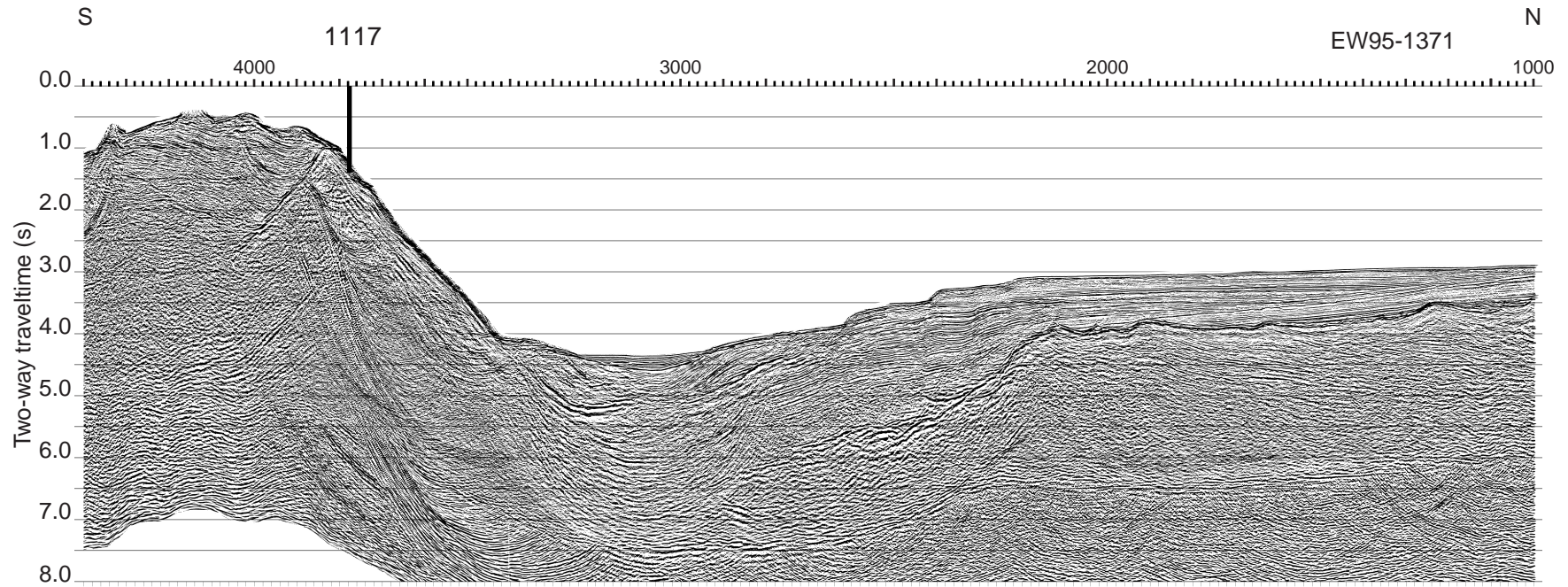
Figure F7. Locations of the Leg 180 drill sites and multichannel seismic tracks, plotted on a shaded relief map with 200-m bathymetric contours (thicker contours labeled every kilometer).
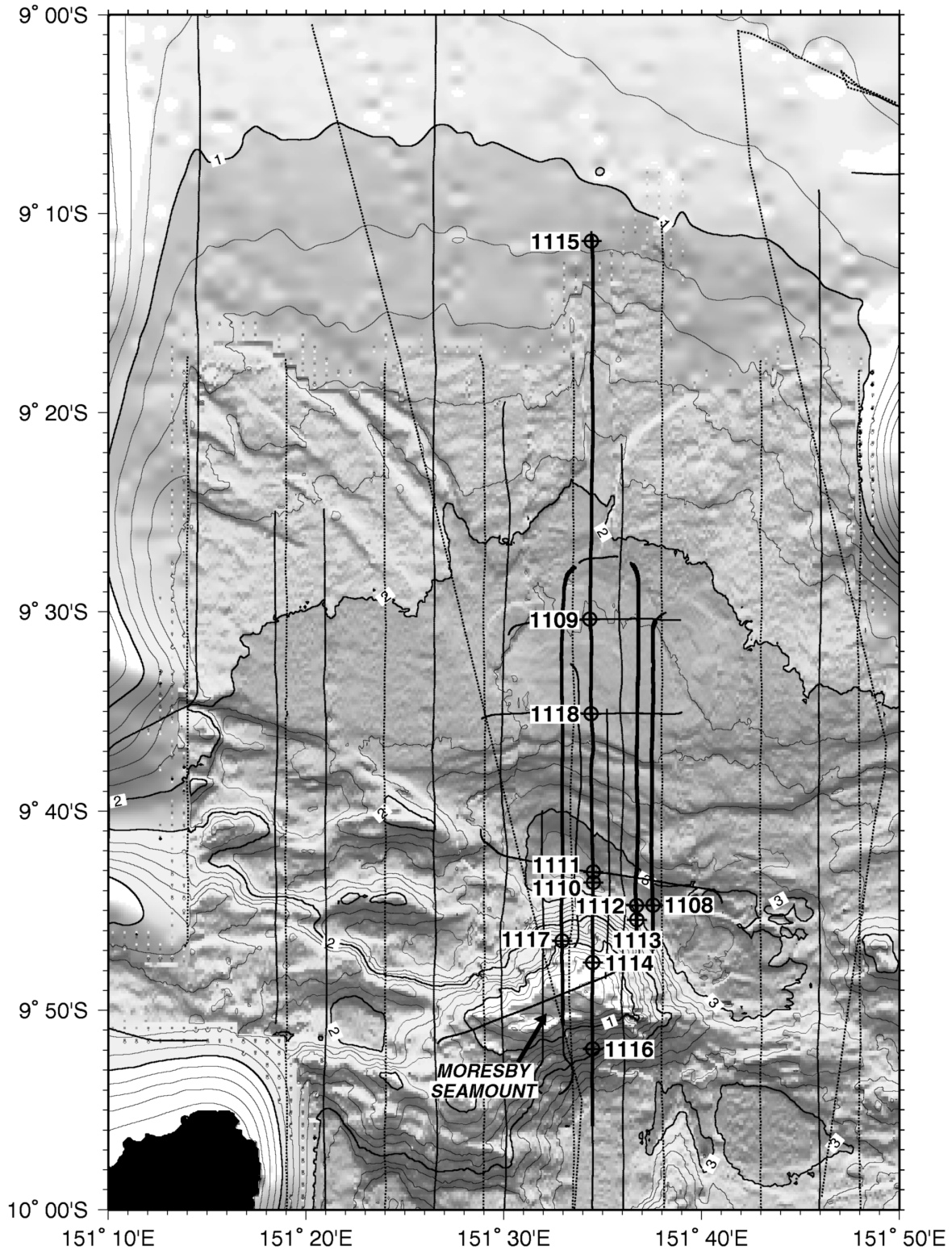
Figure F8. Multibeam bathymetric map (with 100-m contours and thicker contours labeled every kilometer) showing the locations of the Leg 180 drill sites in the vicinity of Moresby Seamount. Multichannel seismic tracks are plotted and labeled every 100 CDPs.
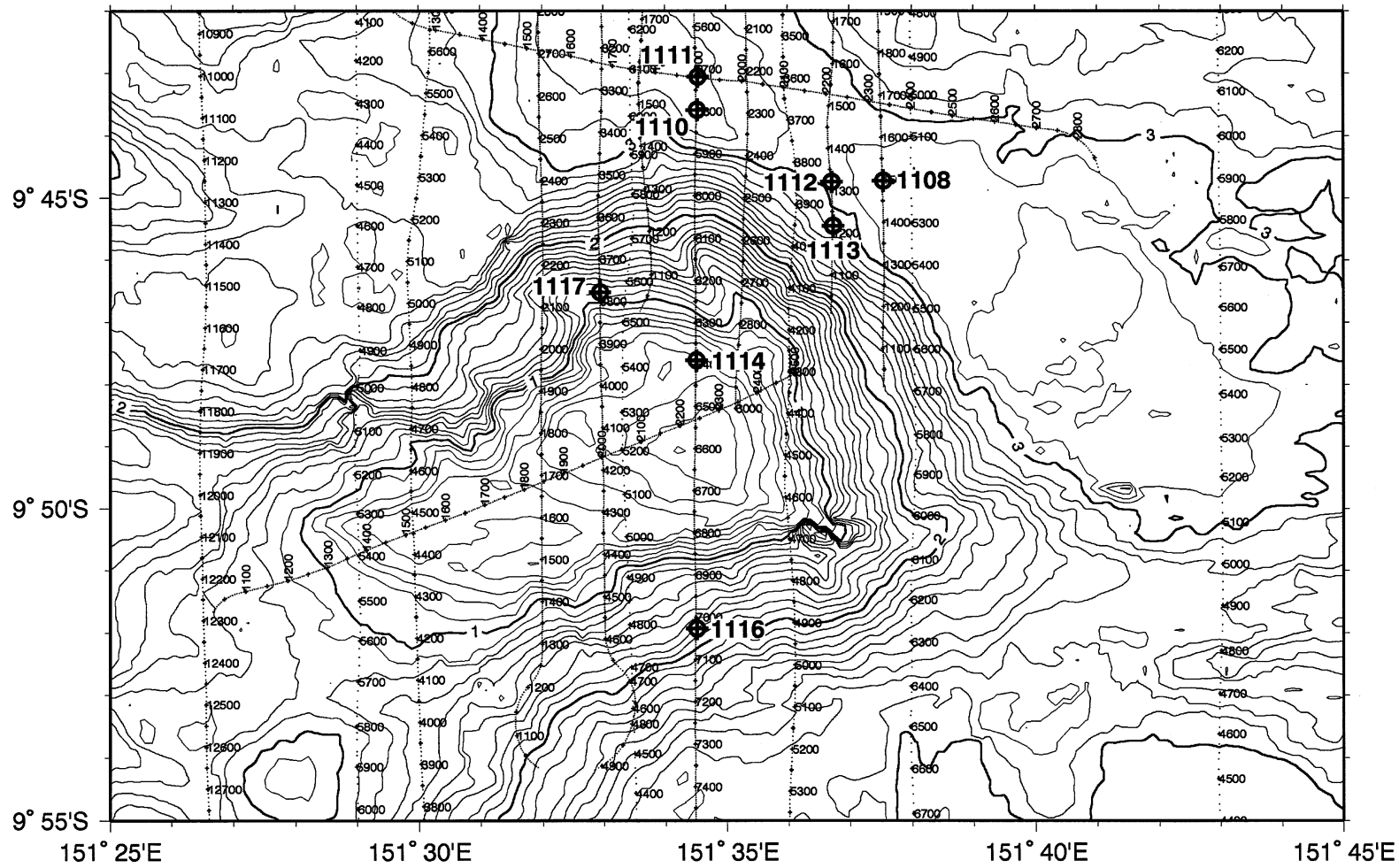
Figure F9. Lithostratigraphy and correlation of Sites 1108, 1109, 1115, and 1118.
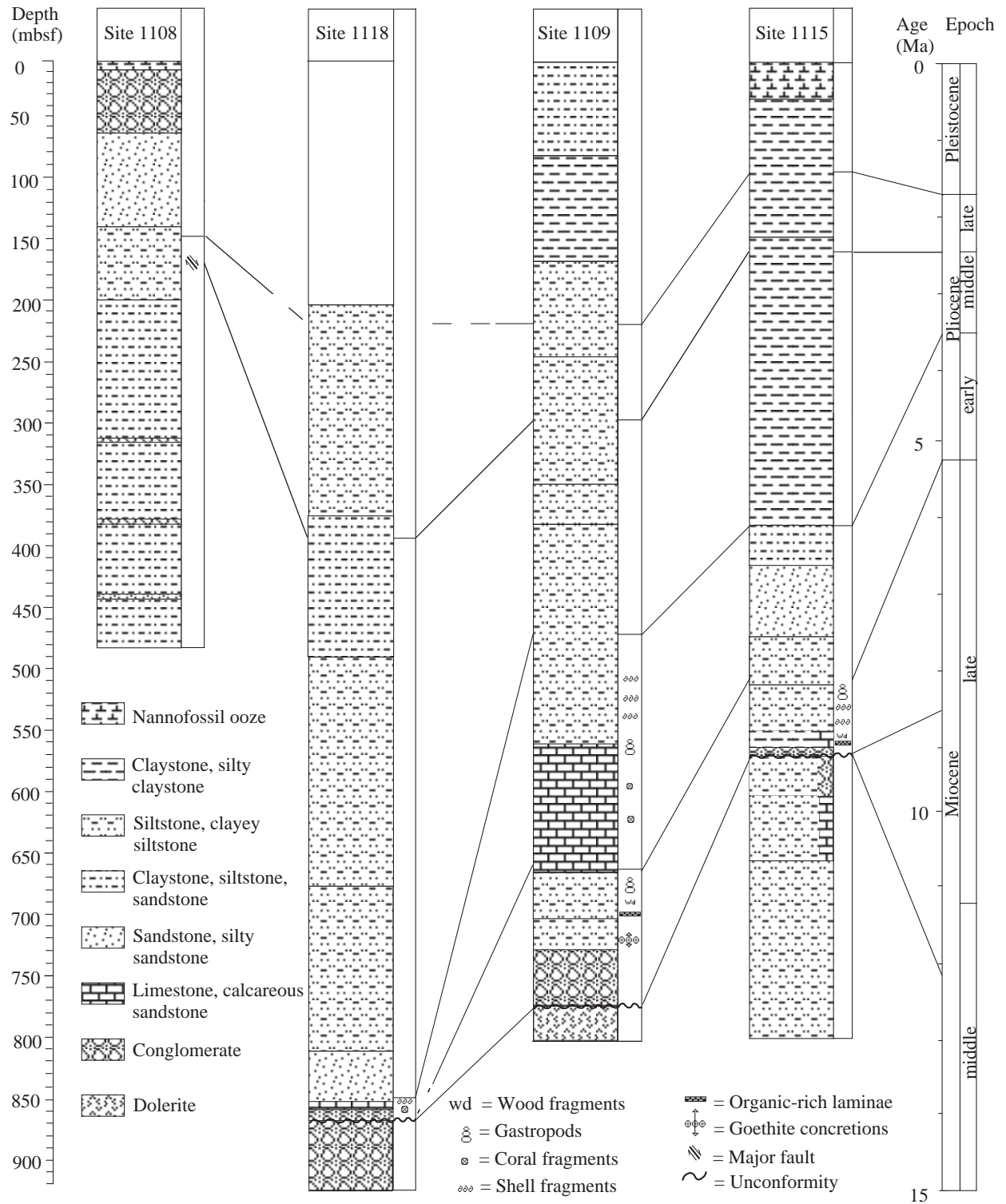
Figure F10. Sedimentation curves at Sites 1115 (solid line), 1109 (dashed line), 1118 (dotted line), 1108 (solid line upper right), 1114 (dashed line upper right), and 1116 (dotted line upper right), based on nannofossil (square) and planktonic foraminifer (circle) datum events, magnetic chron and subchron boundaries (triangle), and lithostratigraphic correlation (star), shaded to differentiate sites. Symbols with arrows denote actual datum point can be above or below and older or younger than indicated by the symbols. Wavy lines denote unconformities. Shown below are average sedimentation rates in meters per million years, calculated for intervals separated by vertical lines, and paleobathymetry, based on benthic foraminifers, at Sites 1115, 1109, and 1118. Broken lines indicate uncertainty in the placement of paleodepth boundaries. **(Figure shown on next page.)**

Age (Ma)

0 1 2 3 4 5 6 7 8 9 10 11 12 13 14 15

Depth (mbsf)

0 50 100 150 200 250 300 350 400 450 500 550 600 650 700 750 800 850

Site 1118

Site 1109

Site 1115

Site 1116

Site 1114

Site 1108

0 1 2 3

0 50 100 150 200 250 300 350 400 450

15

138

324

>70

>176

400

Sedimentation rate (m/m.y.)

| Site 1115 | 34 | 59 | 79 | 133 | 344 | 45 | >13 | ◄ | (<5) | ► | ► >135 | ◄ |

| Site 1109 | 67 | 21 | 225 | 66 | 69 | 160 | 312 | >79 | ◄ | >13 | ◄► |

| Site 1118 | (148) | 155 | 435 | 485 |

Paleo-bathymetry

| Site 1115 | Middle bathyal (500-2000 m) | Upper bathyal (150-500 m) | Outer neritic | Inner neritic (0-50 m) | Outer neritic (50-150 m) | Upper bathyal (150-500 m) |

| Site 1109 | Middle bathyal (500-2000 m) | Upper bathyal (150-500 m) | Outer neritic | Inner neritic | Brackish |

| Site 1118 | | Middle bathyal | Upper bathyal | Neritic (0-150 m) | Middle bathyal (500-2000 m) |

43

Figure F11. A. Porosity data for Sites 1108, 1109, 1111, 1114, 1115, 1116, and 1118, as measured from discrete index property samples. Dashed lines show the depth of the regional unconformity at the northern sites. (Continued on next page.)
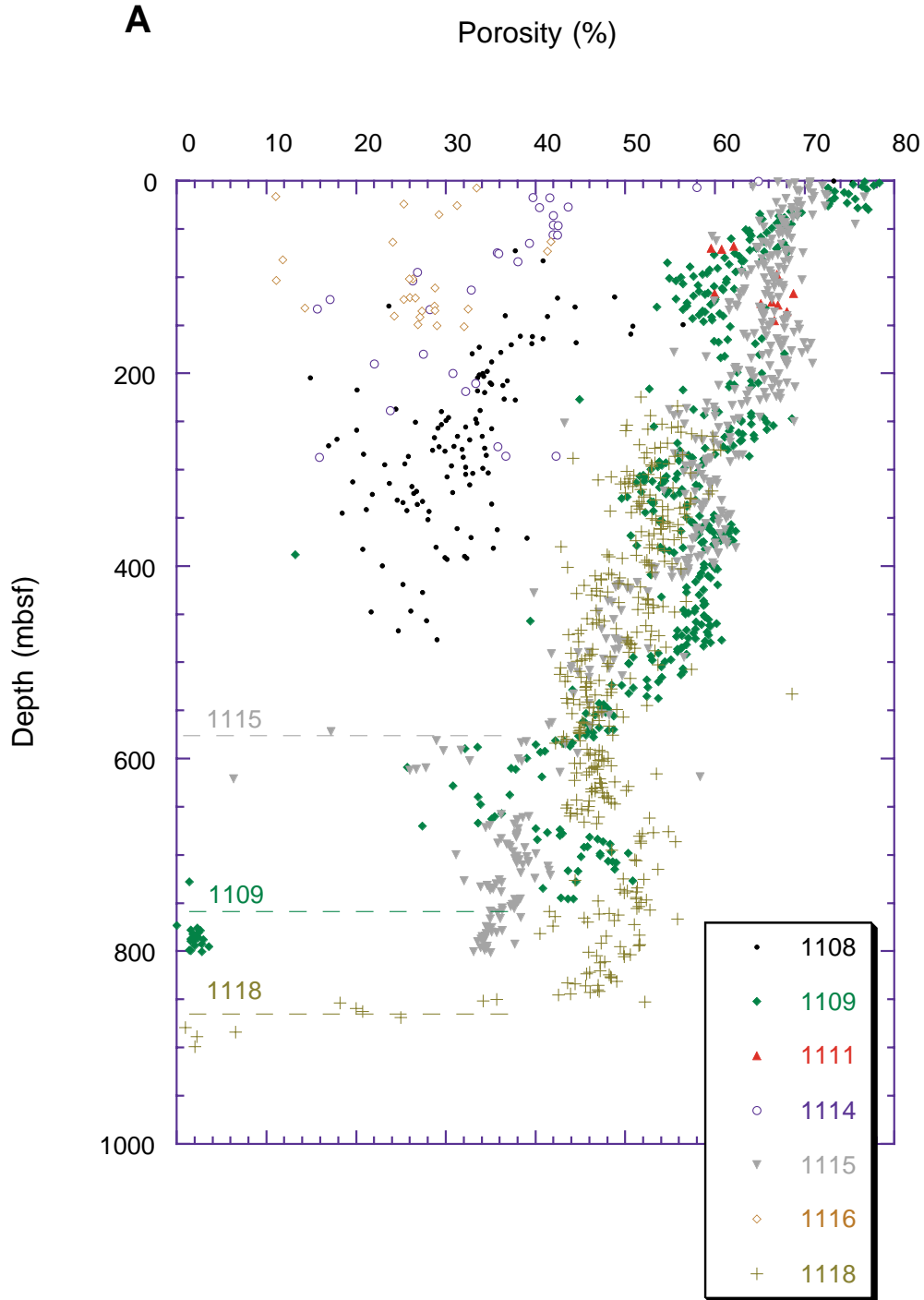
Figure F11 (continued). B. Porosity data, with depth shifts as follows: Site 1108: 500 m added to mbsf depths above 165 mbsf (the location of a fault zone), 700 m added below 165 mbsf; 750 m added to Site 1114 data; and 1000 m added to Site 1116 data. Data below the unconformities at Sites 1109, 1115, and 1118 are not shown because of the unknown hiatus. See **"Erosion Estimates,"** p. 20, for discussion.
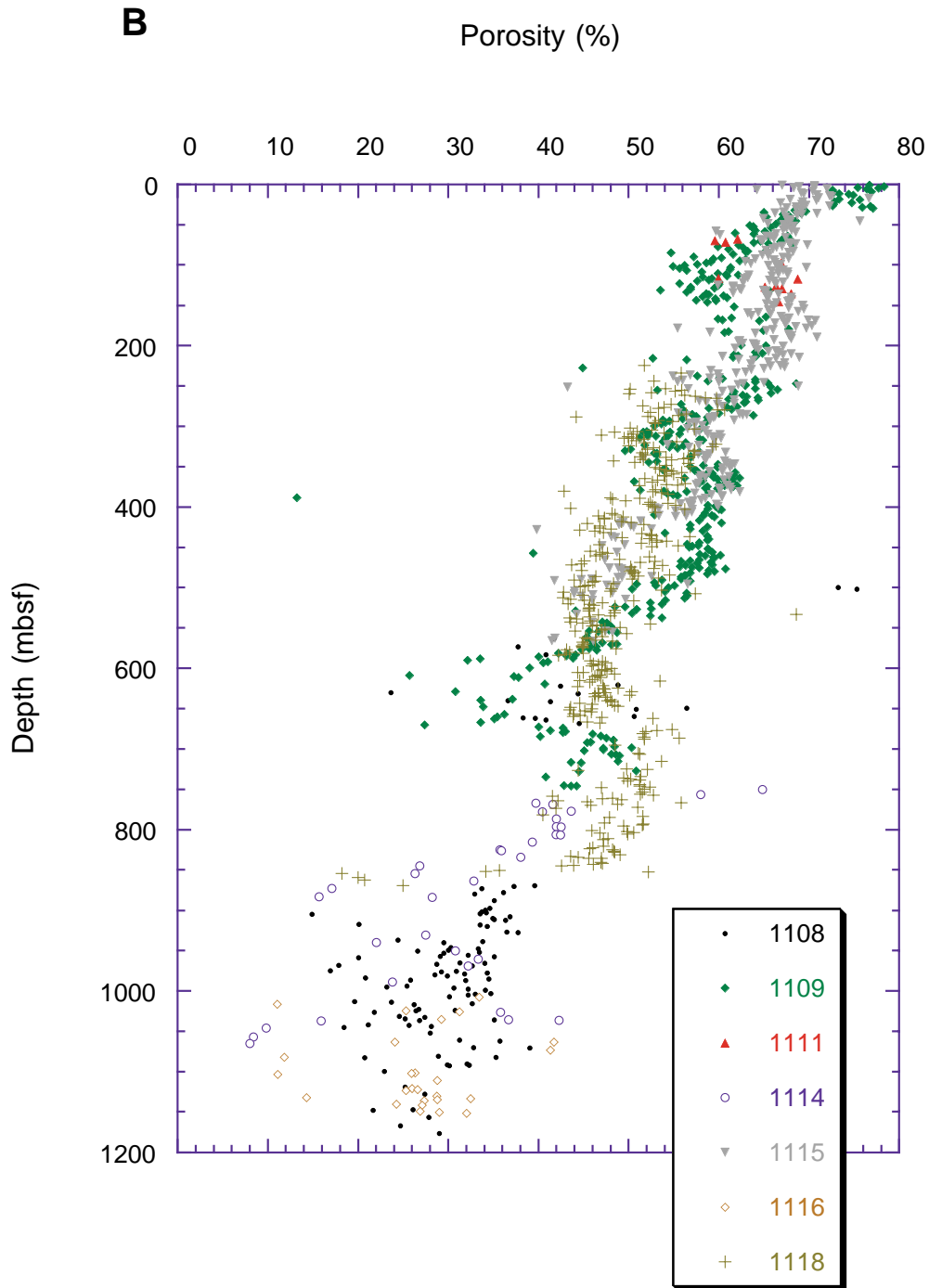
Figure F12. Magnetic susceptibility for Sites 1118, 1109, and 1115 aligned with respect to the location of the top of the Mammoth polarity event (interpolated from "**Biostratigraphy,**" p. 43, in the "Site 1109" chapter).
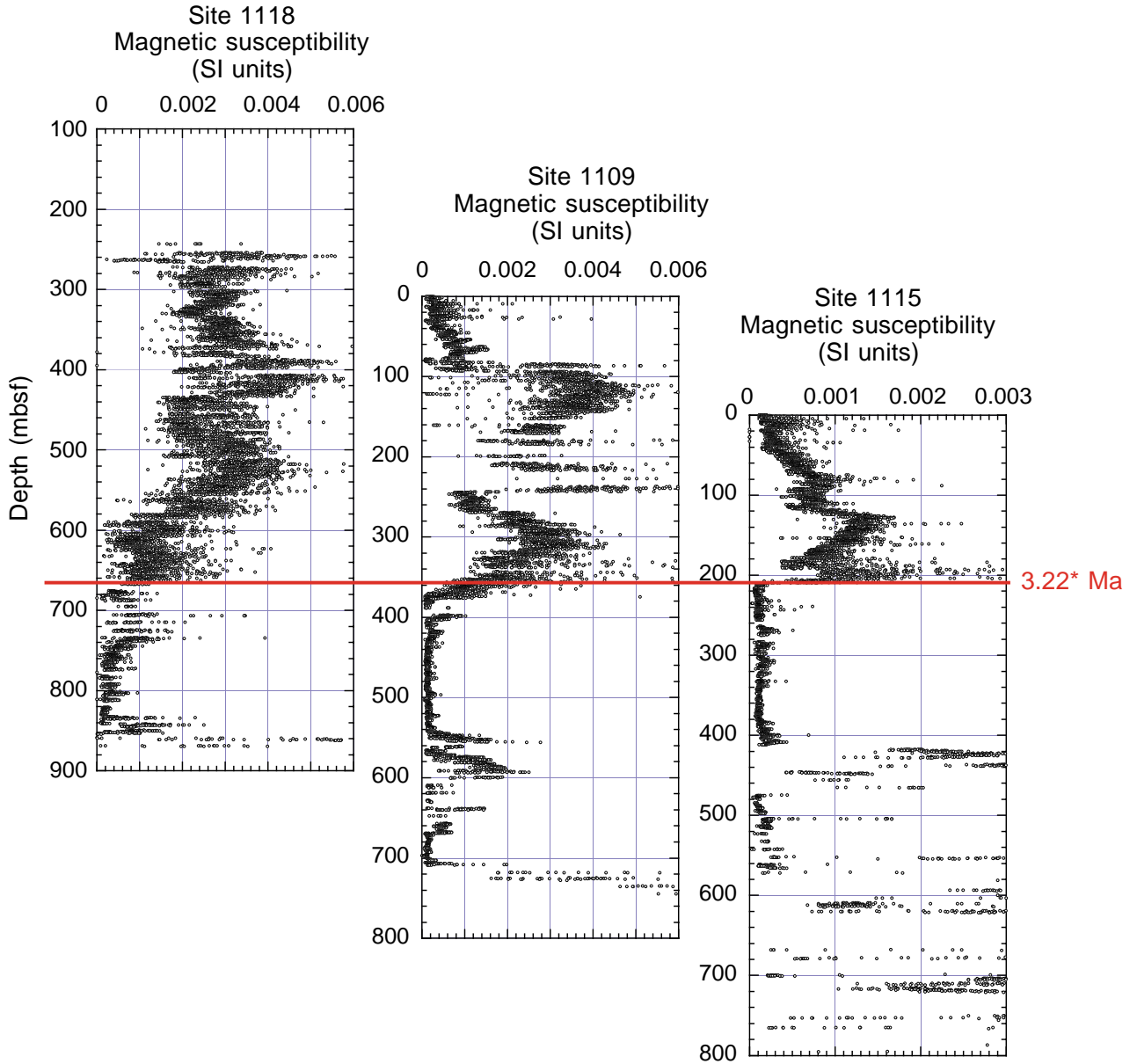
*Top of the Mammoth polarity event

Figure F13. Magnetic susceptibility for Sites 1118, 1109, and 1115 plotted as a function of age. Given the accuracy of the age data, the transition from low- to high-amplitude magnetic susceptibility is approximately coeval across the sites.
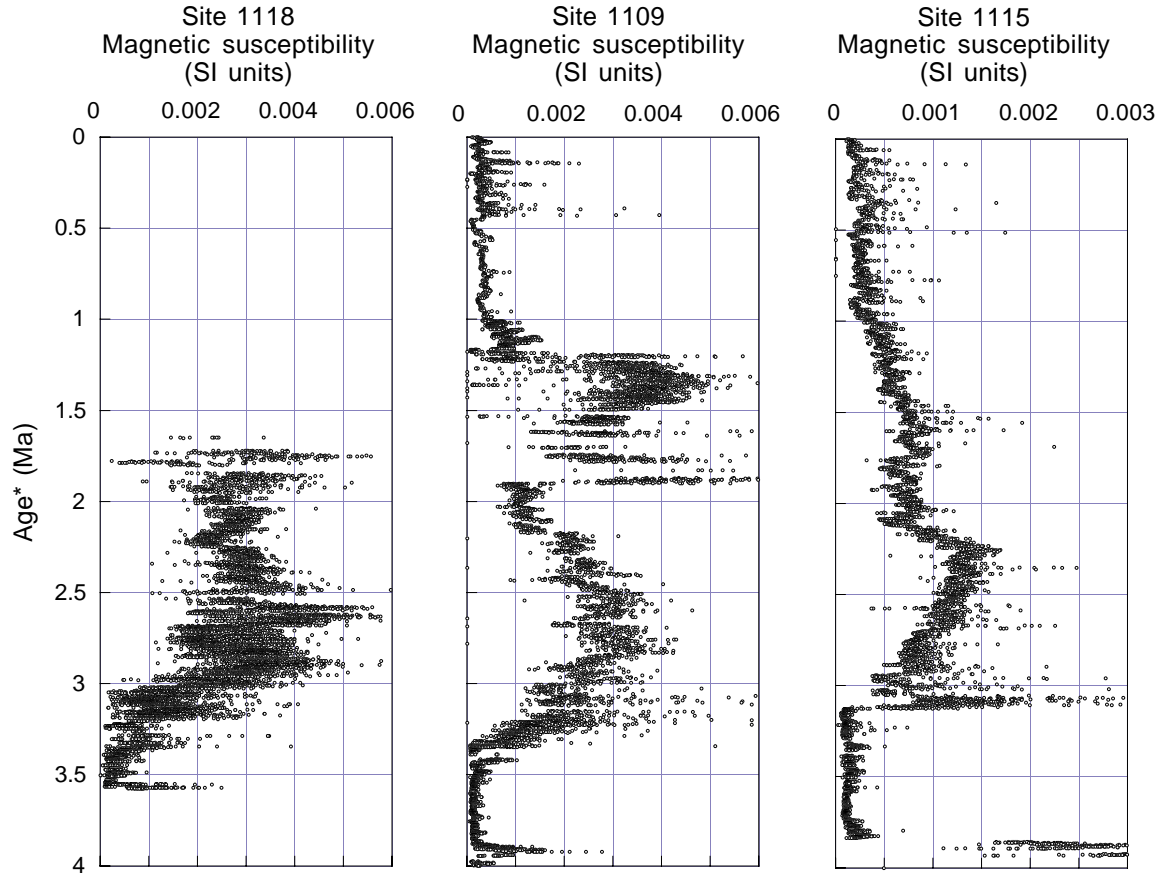
*Biostratigraphic/paleomagnetic estimates

Figure F14. Biogeochemical profiles in sediments from the northern margin (Woodlark Rise) sites, Leg 180: **A.** Total bacterial populations at Sites 1109, 1115, and 1118. The solid curve represents a general regression line of bacterial numbers vs. depth in deep-sea sediments (Parkes et al., 1994), with 95% upper and lower prediction limits shown by dashed curves. Sulfate, ammonia, and methane depth profiles at Sites (**B**) 1118, (**C**) 1109, and (**D**) 1115. Unconformity at each site represented by wavy line. **E.** C_1/C_2 ratios at Sites 1108, 1109, 1115, and 1118.
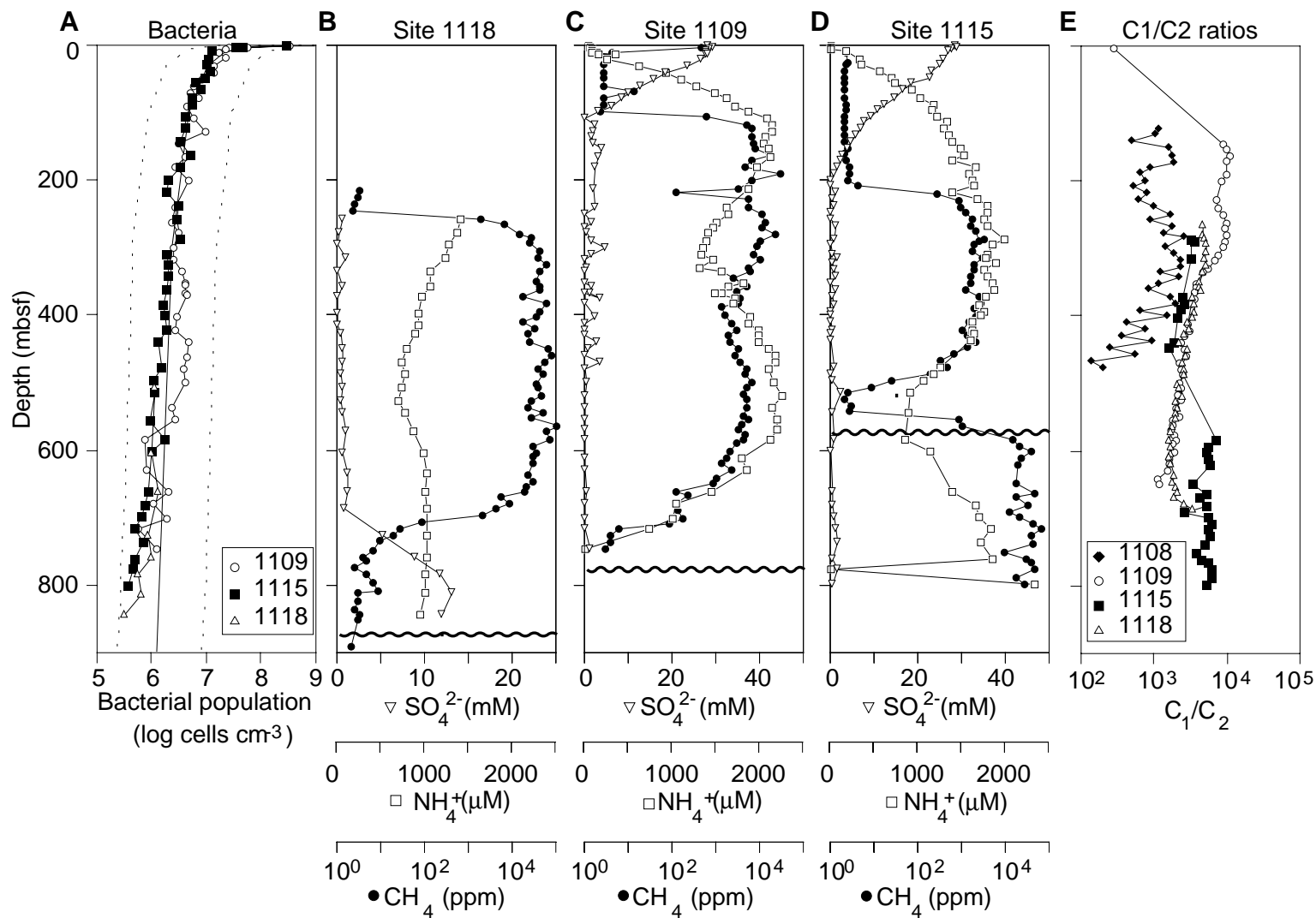
Figure F15. Plot of dissolved Ca^{2+}, Mg^{2+}, and SiO_2 at northern margin (Woodlark Rise) sites. The shapes of the Ca^{2+} and Mg^{2+} profiles reflect the effects of carbonate diagenesis and a variable extent of alteration of volcanic matter in the upper portion of the sedimentary column of each site. Deeper downhole, alteration of volcanics exerts a more dominant control on pore-water profiles. Large increases in dissolved Ca^{2+} result primarily from alteration of plagioclase whereas depletion of Mg^{2+} reflects its uptake during authigenic smectite formation. The dissolved SiO_2 profiles depict a downhole progression including dissolution of volcanic ash in the upper sedimentary column, and silicification reactions deeper downhole. Particularly elevated SiO_2 concentrations deep in Site 1118 are attributable to an abundance of fresh to slightly altered volcanic matter in higher porosity sediments.
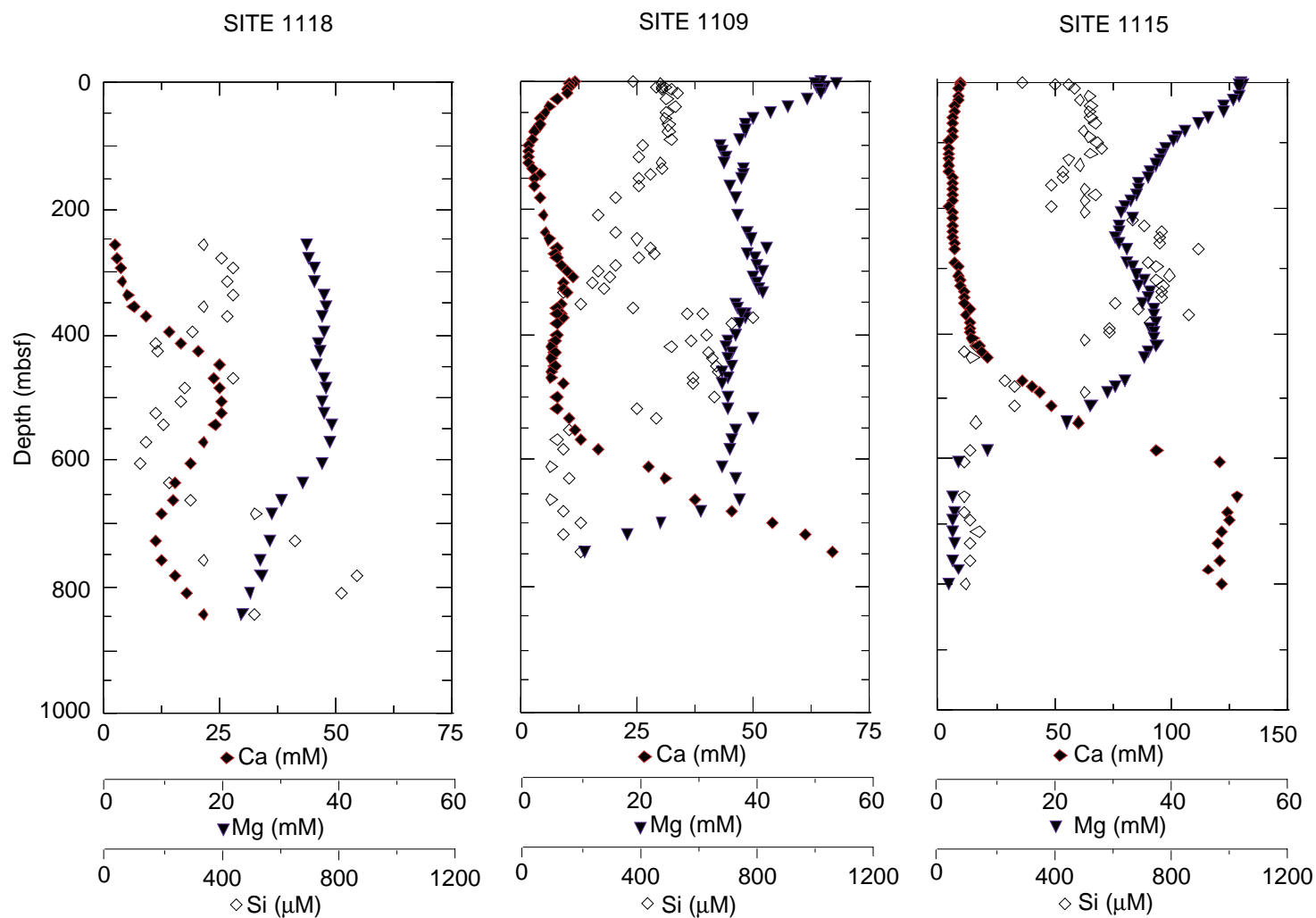
Figure F16. Hole 1118A core photograph illustrating the transition facies from dolerite (interval 180-1118A-70R-1, 87–140 cm), interpreted as a clast in conglomerate, overlain by shallow-marine conglomerates (interval 180-1118A-69R-1, 15 cm, through 70R-1, 87 cm), limestone (68R-3, 115 cm, through 69R-1, 15 cm), and volcaniclastic sandstone (68R-1, 0 cm, through 68R-3, 115 cm). We interpret the contact at the top of the dolerite as the rift onset unconformity.

Hole 1118A
(849.3-870.14 mbsf)
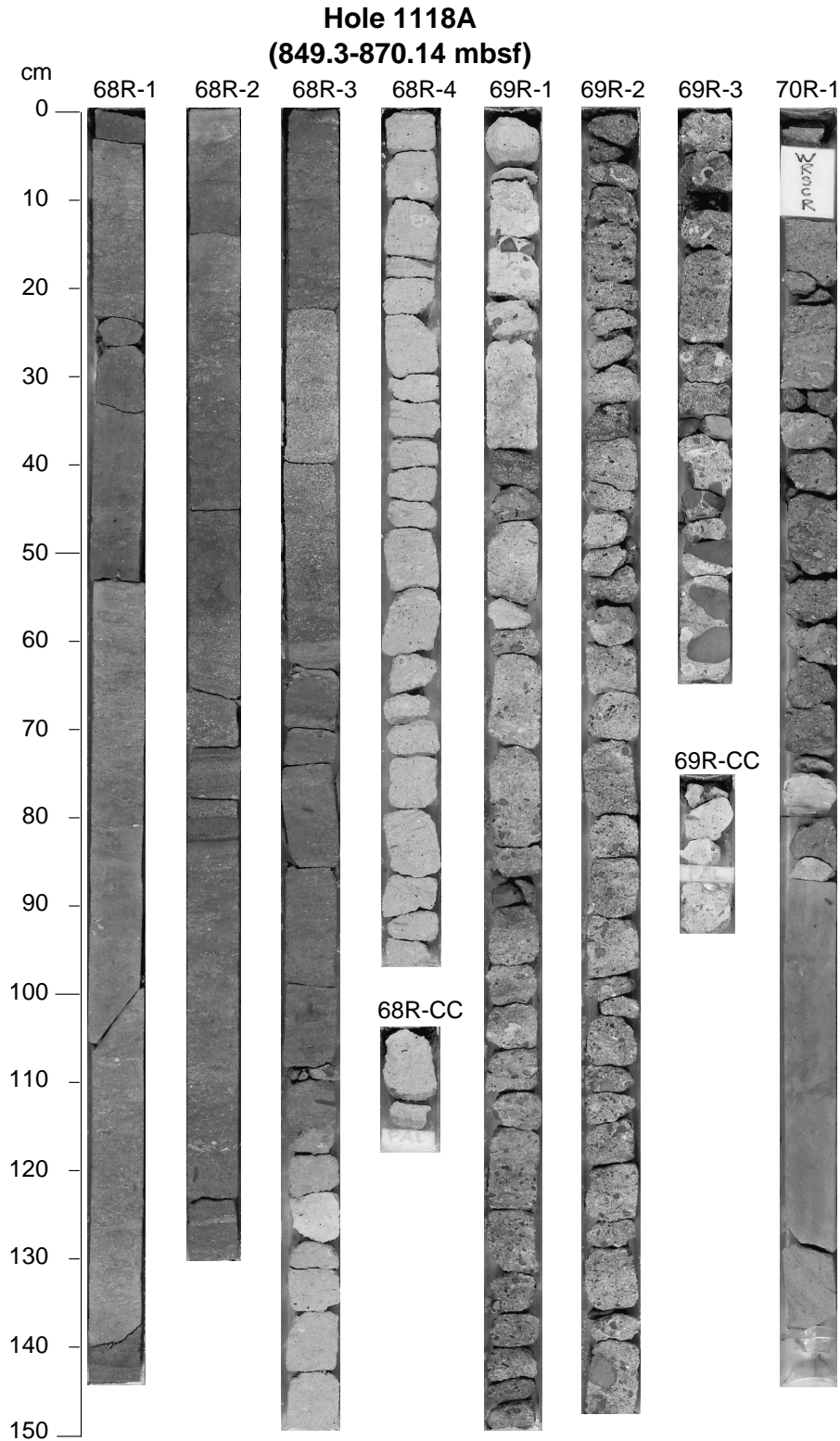
Figure F17. Occurrence of volcanogenic ash layers at Sites 1118, 1109, and 1115 shown in terms of thickness (gray pattern) and number of volcanogenic ash layers (black pattern) per core for Pliocene–Pleistocene time. Note: the spiky nature of the peaks of volcaniclastic input are in part artifacts of variable core recovery. Refer to the visual core descriptions for details of recovery (see **"Core Descriptions"** contents list).
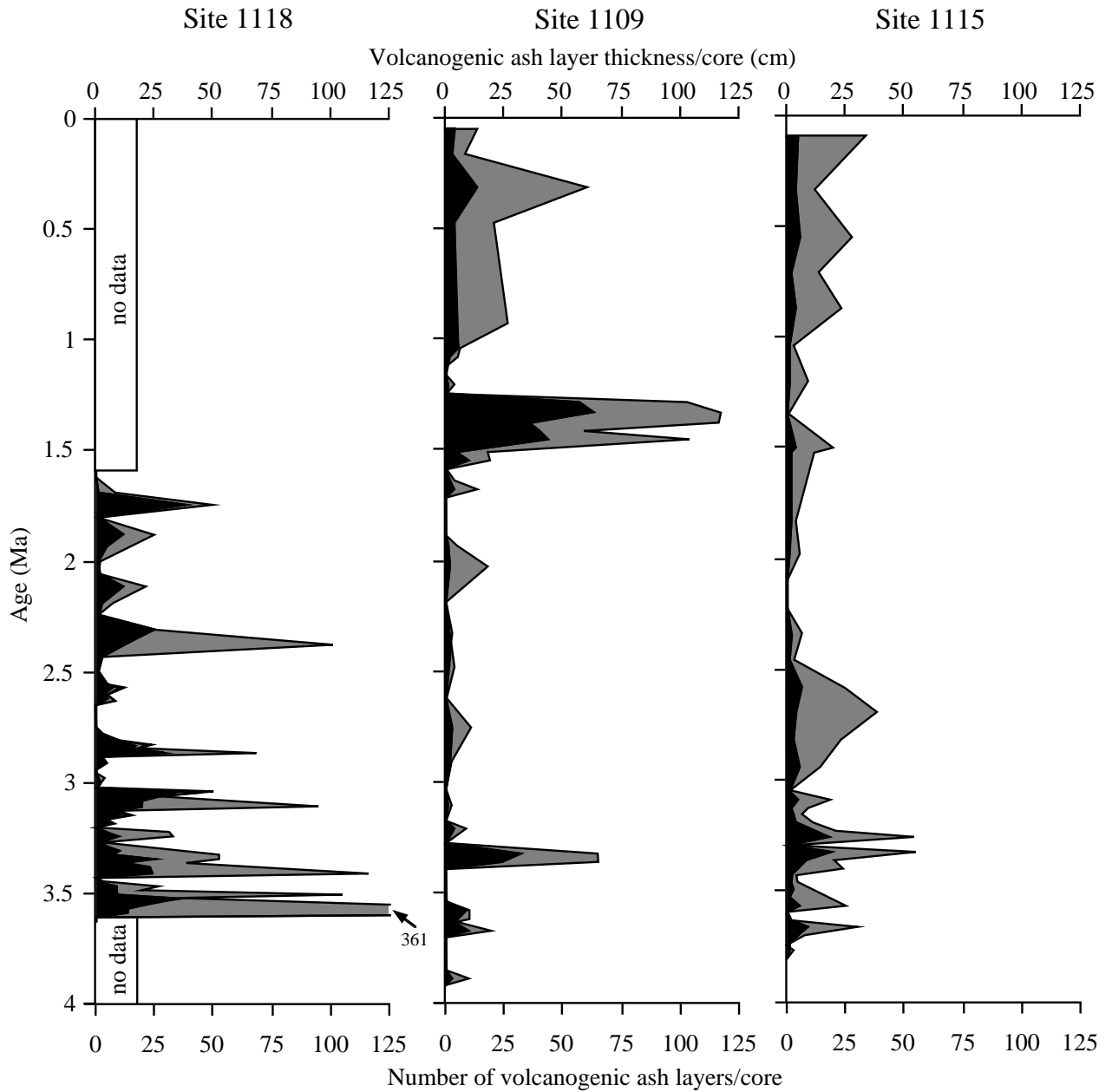
Figure F18. Hand specimen of gabbro showing coarse-grained, nonlaminated nature. No layering was apparent at the scale of the recovered material (Sample 180-1117A-13R-1, 19–23 cm).
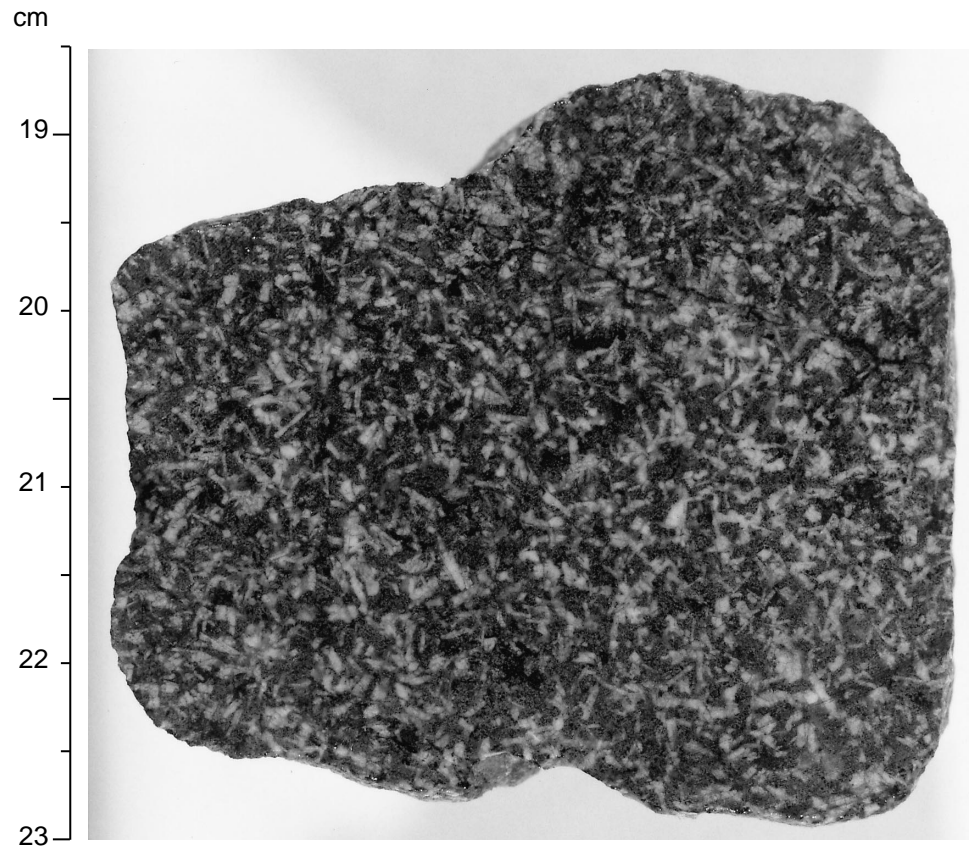
Figure F19. Core photograph of the fault gouge recovered at Site 1117. This shows soft, light-colored clayey material that contains talc, chlorite, calcite, ankerite, and serpentine. This material is consistent with intense shearing and hydrothermal alteration of underlying deformed gabbro.
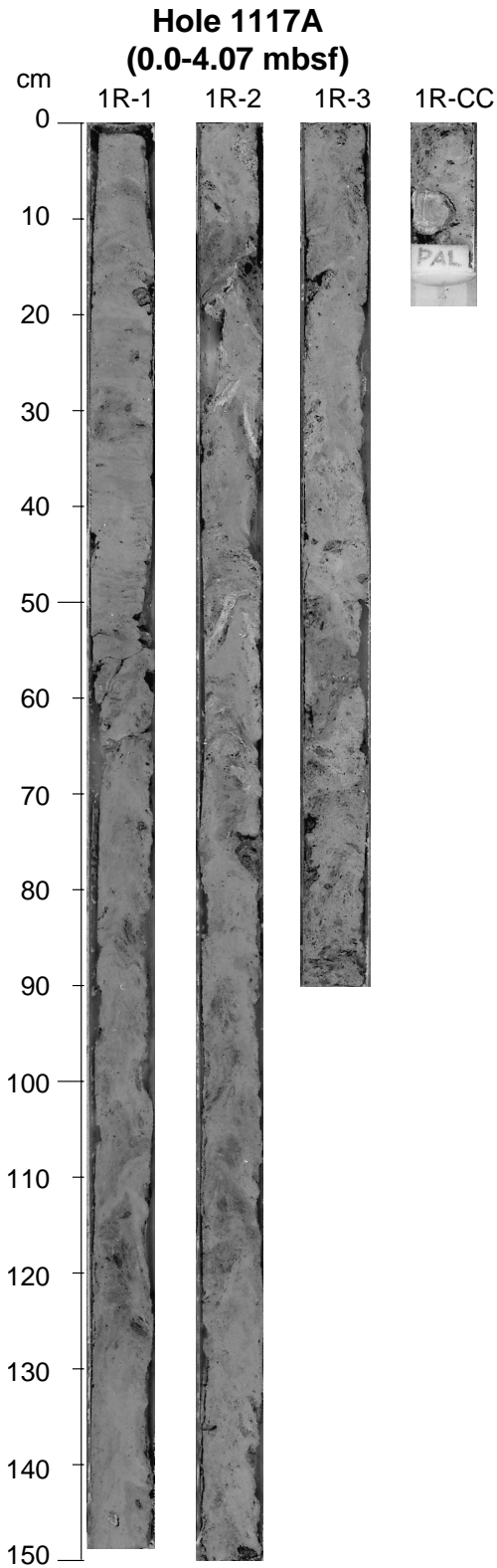
Figure F20. Close-up photograph of highly sheared gabbro with a well-developed foliation plane and shear bands (S-C mylonite; Sample 180-1117A-9R-1, 24–32 cm).
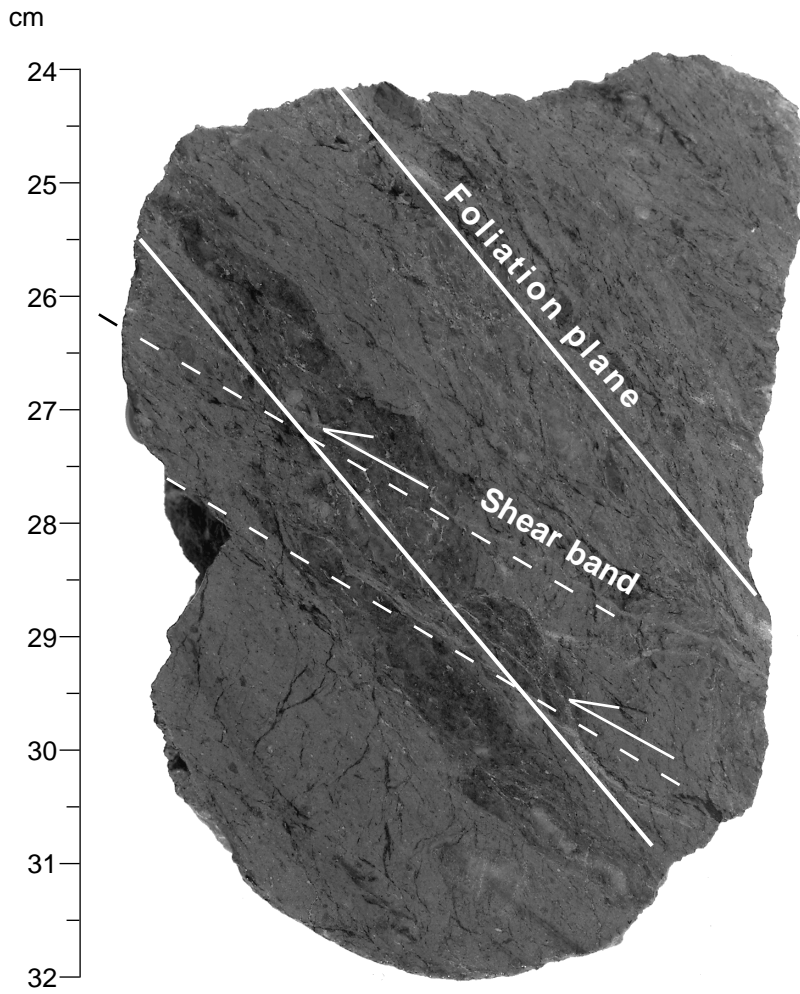
Figure F21. Lithostratigraphy of Sites 1114, 1116, and 1117 on Moresby Seamount.
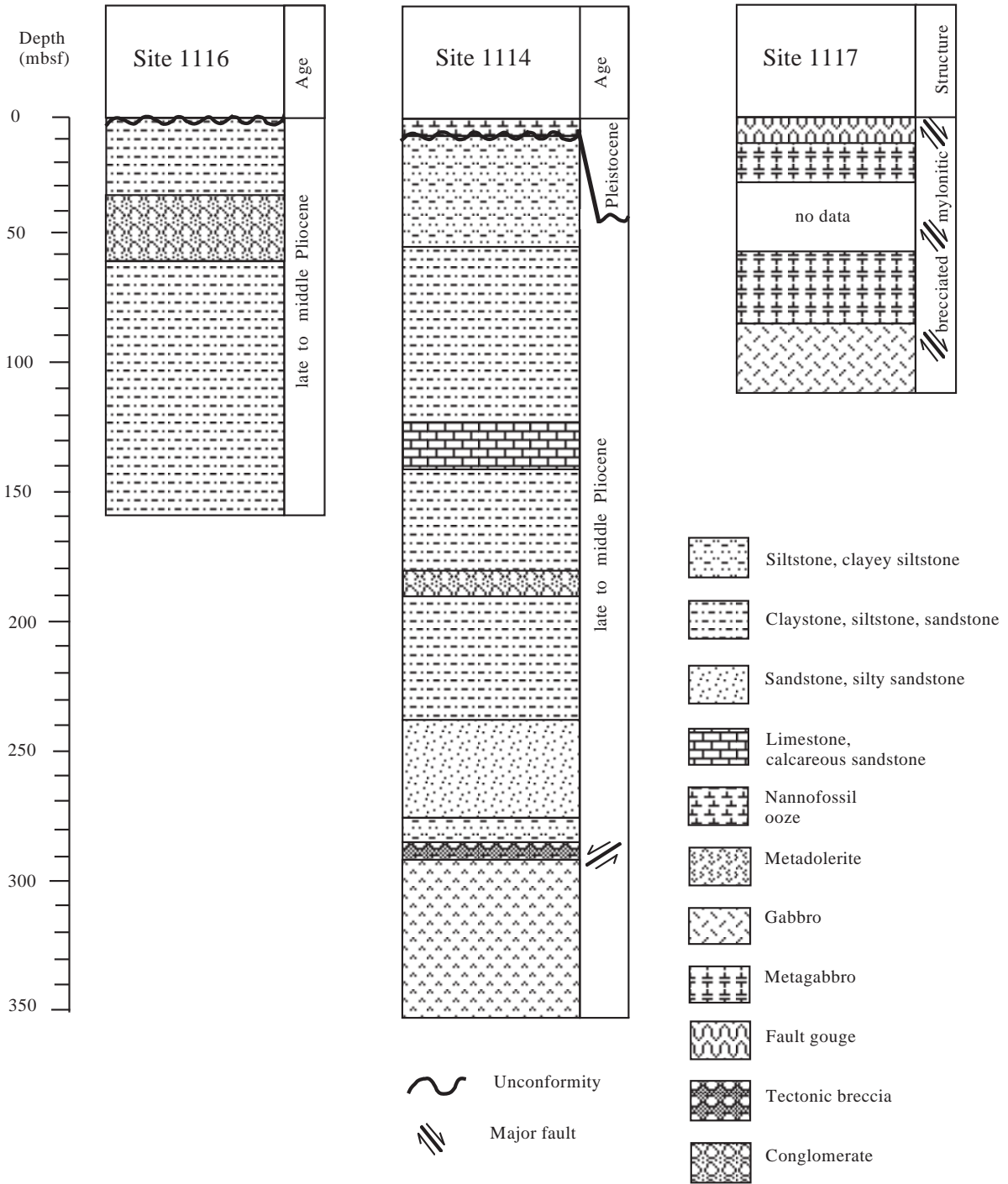
Figure F22. Bed and fracture dip direction distributions from FMS images analysis at Site 1114. **A**, **B.** Histograms of bed and fracture dip directions. **C, D.** Rose diagrams of bed and fracture strikes. The two main populations consist of beds that strike northeast and fractures that strike just north of east.
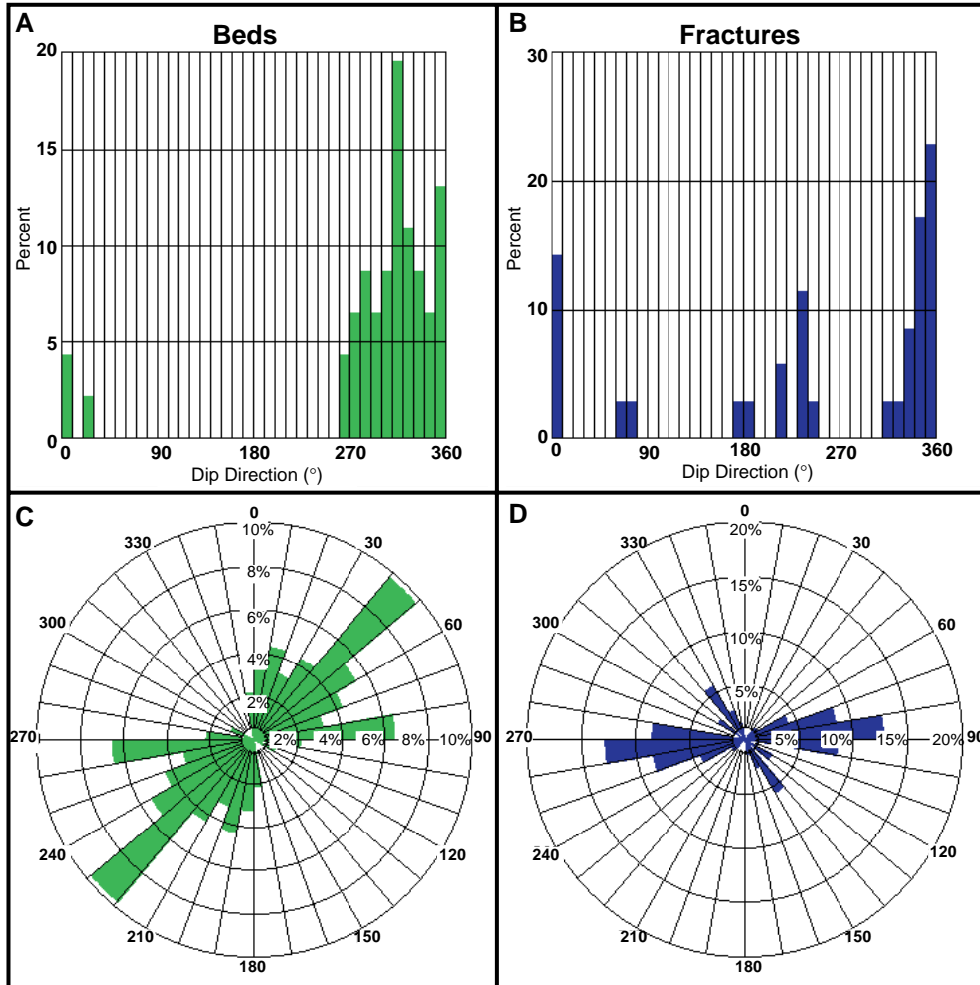
Figure F23. Calcium carbonate content plotted vs. depth at Site 1115. Note the downward decrease in calcium carbonate content to 300 mbsf.
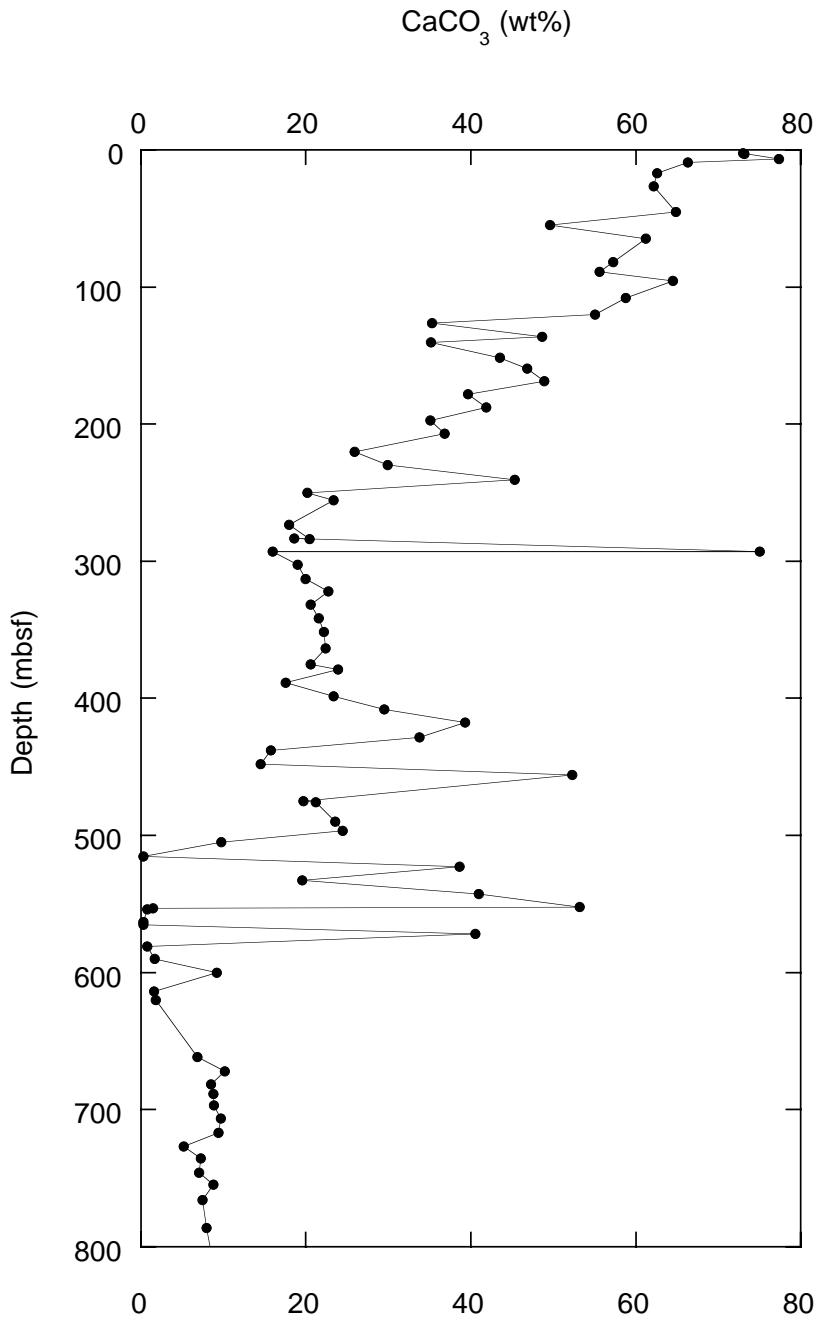
Figure F24. Digital photomicrograph (plane-polarized light). Crystal vitric tuff, with abundant angular, fresh pipe vesicle glass shards in a glassy matrix (Sample 180-1118A-38R-3, 128–130 cm).
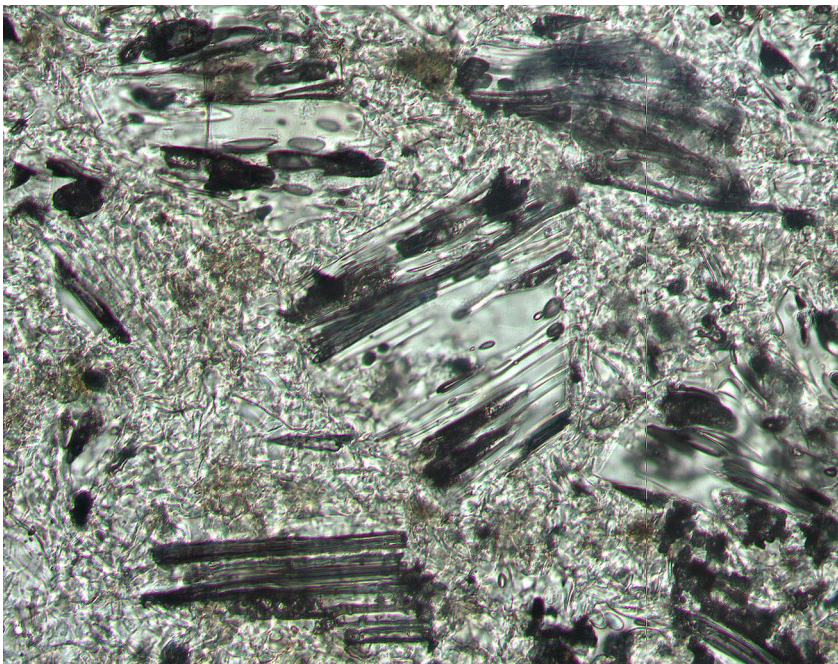
0.5 mm

Figure F25. Depth converted multichannel seismic (MCS) traces at Sites 1118 and 1109, displayed with the lithostratigraphic columns. The MCS data in time, spanning the two sites, are shown correlated with depth. CMP = common midpoint; 50 CMPs = 621 m. TWT = two-way traveltime. Lithologic patterns as in Figure F9, p. 41.
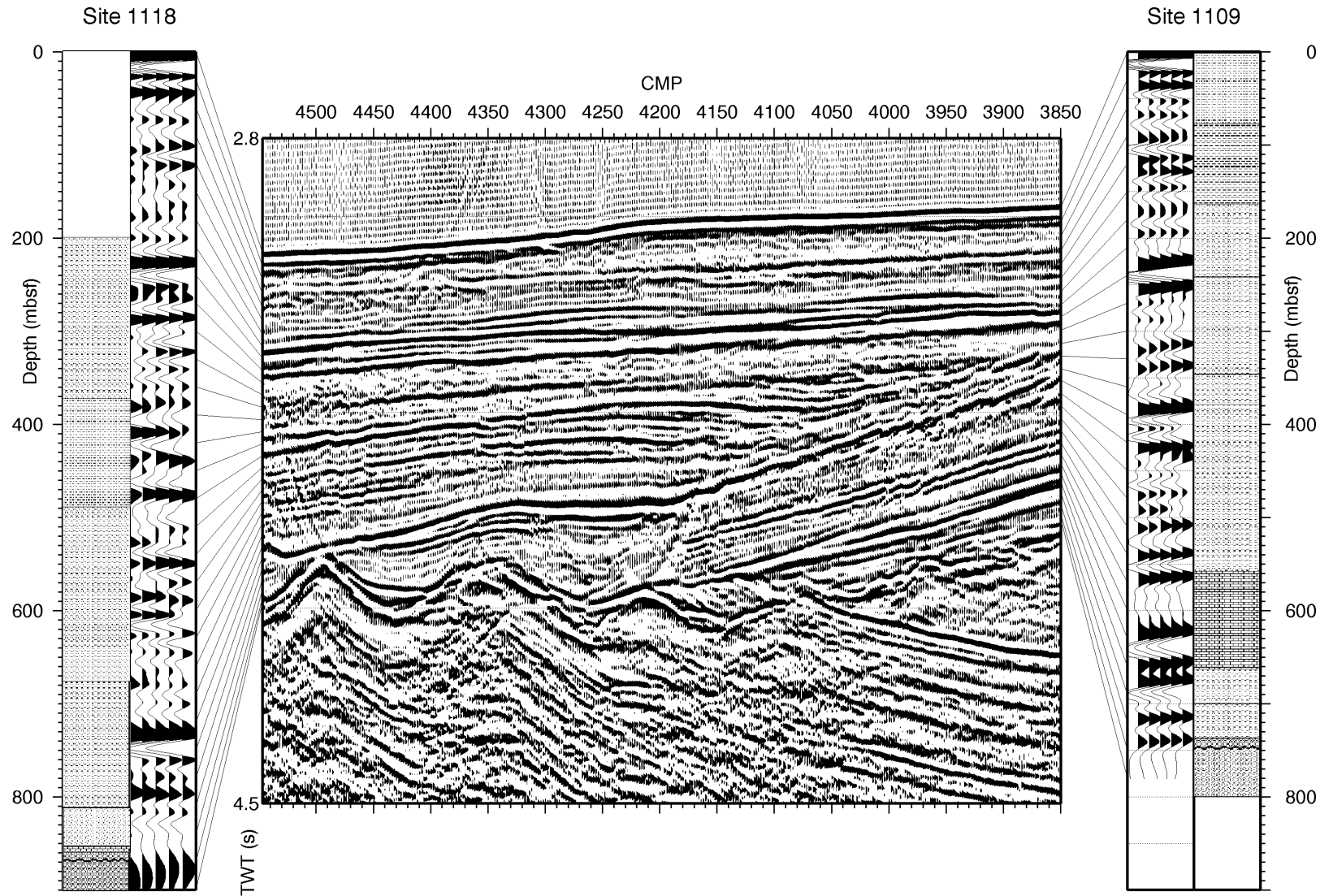
Figure F26. Digital photomicrograph (plane-polarized light). A pumiceous rock containing phenocrysts of hornblende within a glassy groundmass. Occurs as a granule-size clast within a sandy silty claystone (Sample 180-1115C-12R-5, 50–53 cm).
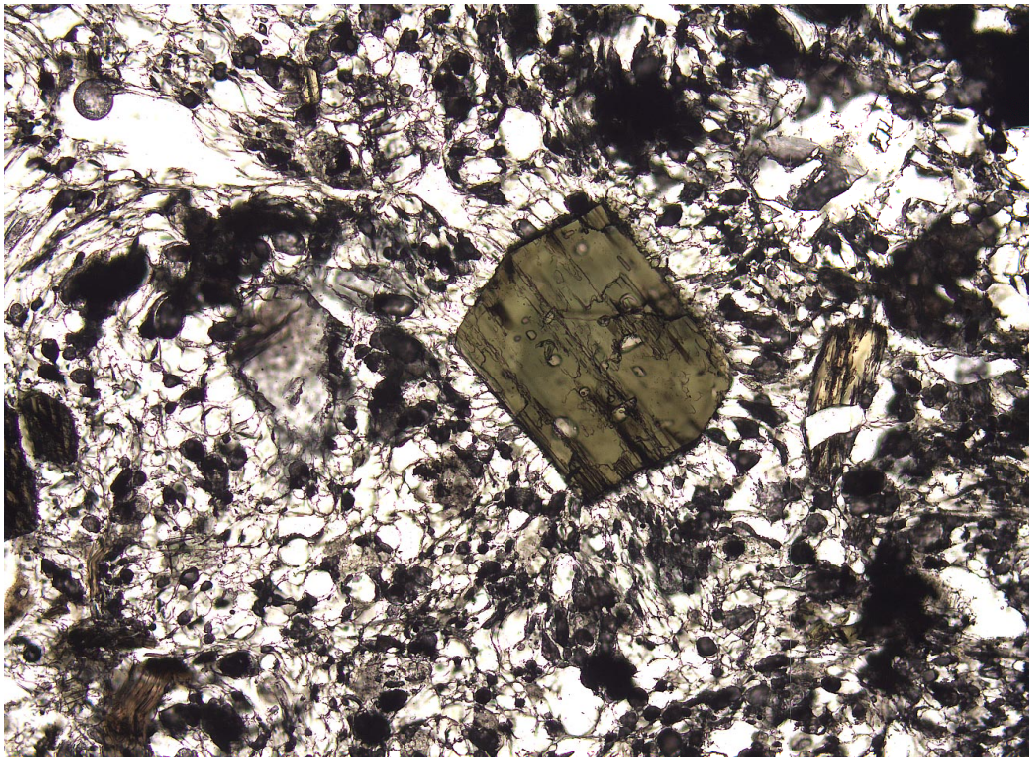
1 mm

Figure F27. Digital photomicrograph (crossed nicols). A well-rounded clast of fresh glassy basalt with plagioclase and biotite microphenocrysts, set in a calcitic matrix including volcanic and metamorphic grains (Sample 180-1108B-3R-CC, 0–4 cm).
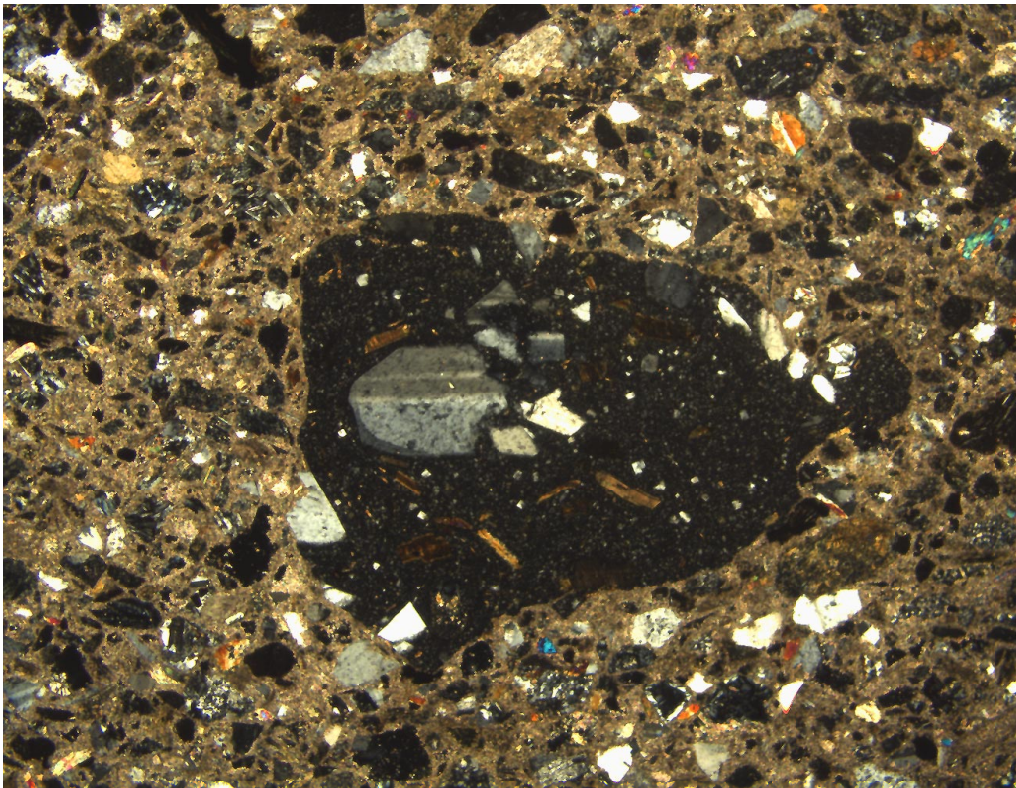

4 mm

Figure F28. Digital photomicrograph (crossed nicols). A subrounded clast of basalt with plagioclase microphenocrysts (right); an acidic clast (left), and a clast of serpentinite (lower). The matrix is calcareous, with quartz and feldspar grains (Sample 180-1108B-3R-CC, 0–4 cm).
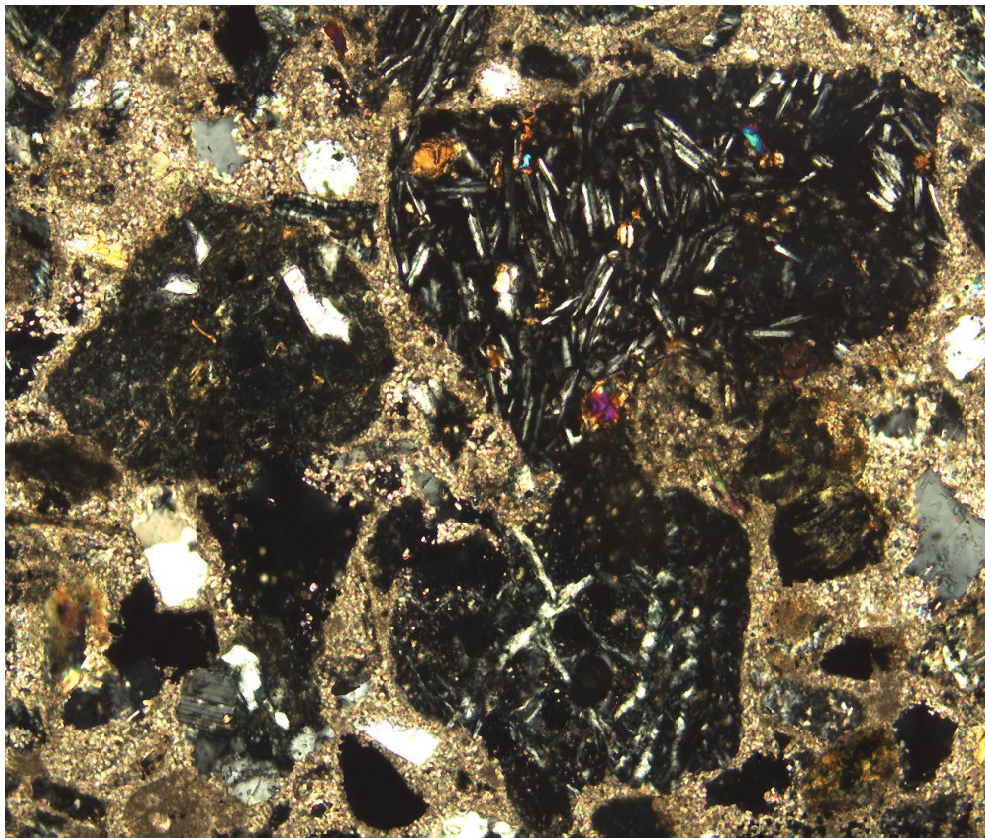
1 mm

Figure F29. Digital photomicrograph (crossed nicols). Angular fragment of calc-schist, surrounded by glassy basalt and silicic fragments, set in a sparry calcite cement (Sample 180-1116A-13R-2, 25–27 cm).
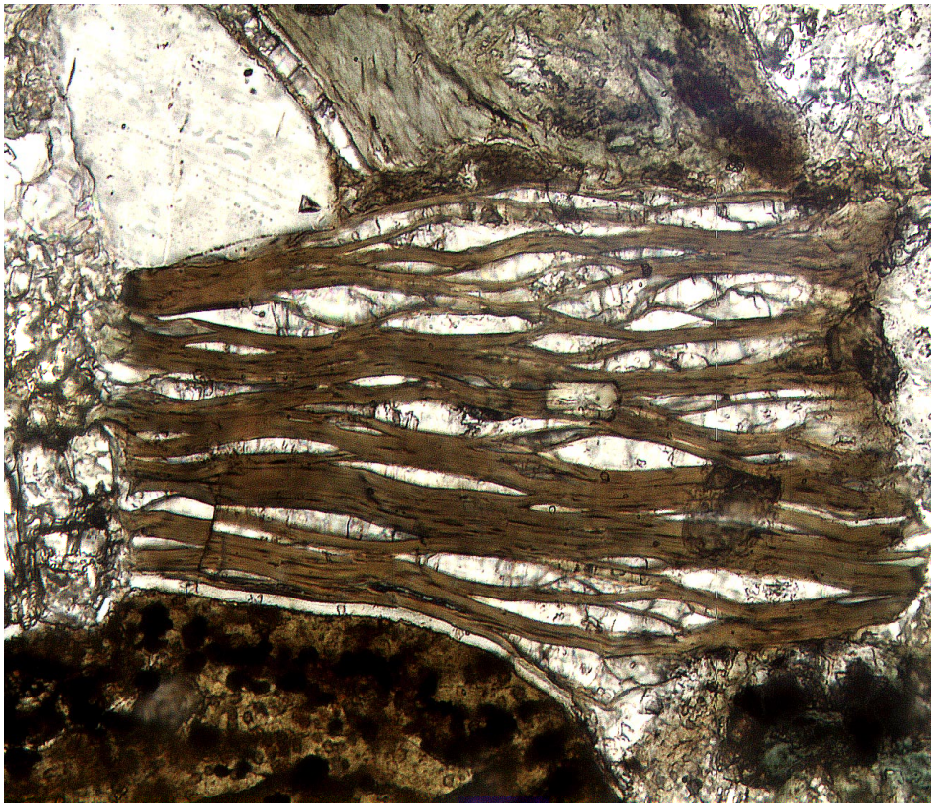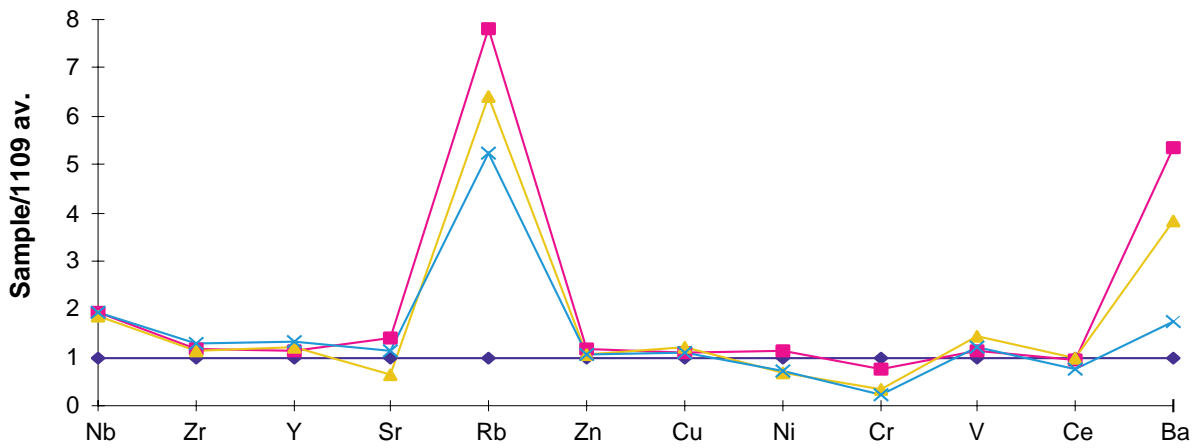

0.25 mm

Figure F30. Plots of major and trace element data for dolerites and metadolerites from Sites 1109, 1114, 1117 and 1118 normalized to average values from Site 1109 (presumed closest to pristine dolerite).
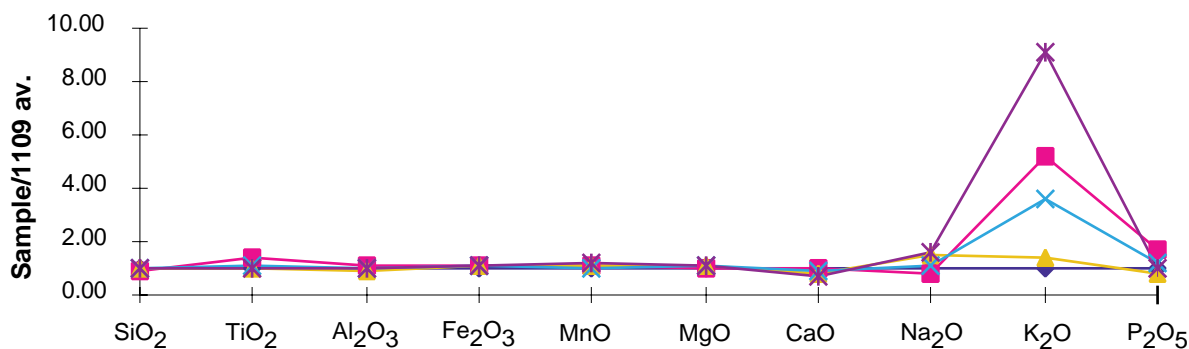
Major Elements Normalized to Site 1109
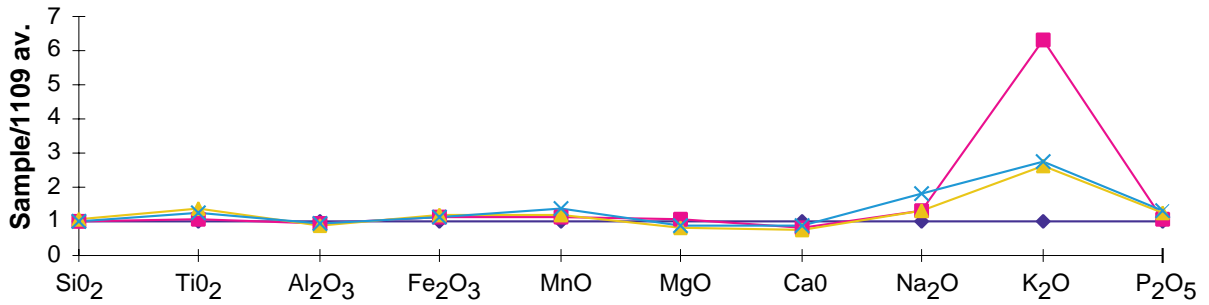
Trace Elements Normalized to Site 1109

Figure F31. Plot of major and trace element data for dolerite and metadolerite samples from talus at Sites 1108, 1111, and 1114 normalized to the average values for unaltered dolerite from Site 1109. Key: 1 = foliated, epidote-rich schist in Hole 1111A (Sample 180-1111A-16R-CC, 8–15 cm); 2 = metadolerite pebble in sediments of Hole 1108B (Sample 180-1108B-47R-CC, 1–3 cm); 3 = nonfoliated metadolerite in Hole 1114A (Sample 180-1114A-36R-2, 40–42 cm); 4 = foliated metadolerite pebble in Hole 1114A (Sample 180-1114A-36R-1, 70–72 cm).
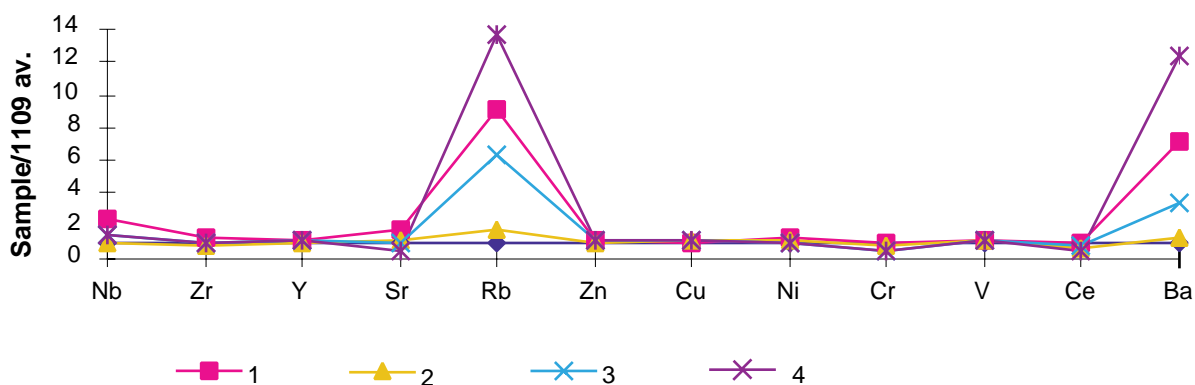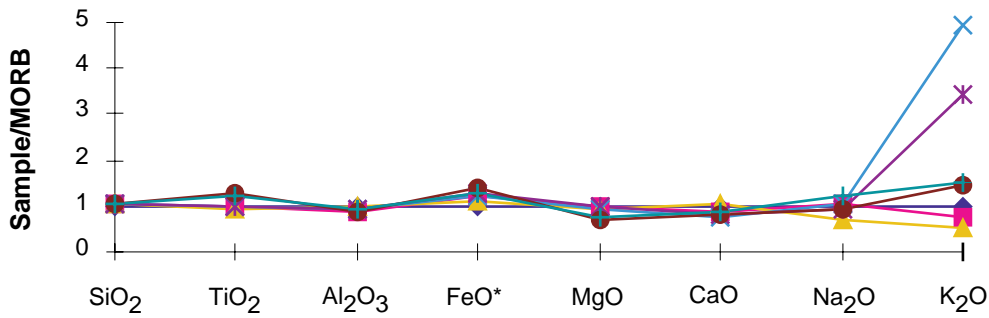
Figure F32. Plot of major and trace elements of dolerites and metadolerites from Sites 1108, 1109, 1111, 1114, 1117, and 1118 normalized to E-MORB using the values of Sun and McDonough (1989).
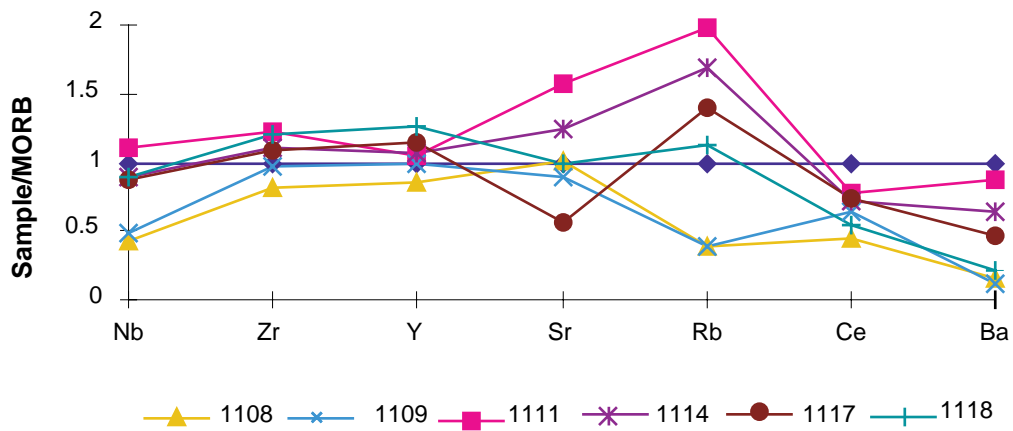
Figure F33. Schematic cross section showing the increasing proportion (in pie charts) of strike-slip and oblique-slip faults toward the Moresby Seamount. Note that oblique- and strike-slip faults at Sites 1109 and 1115 occur in the prerift sequence.
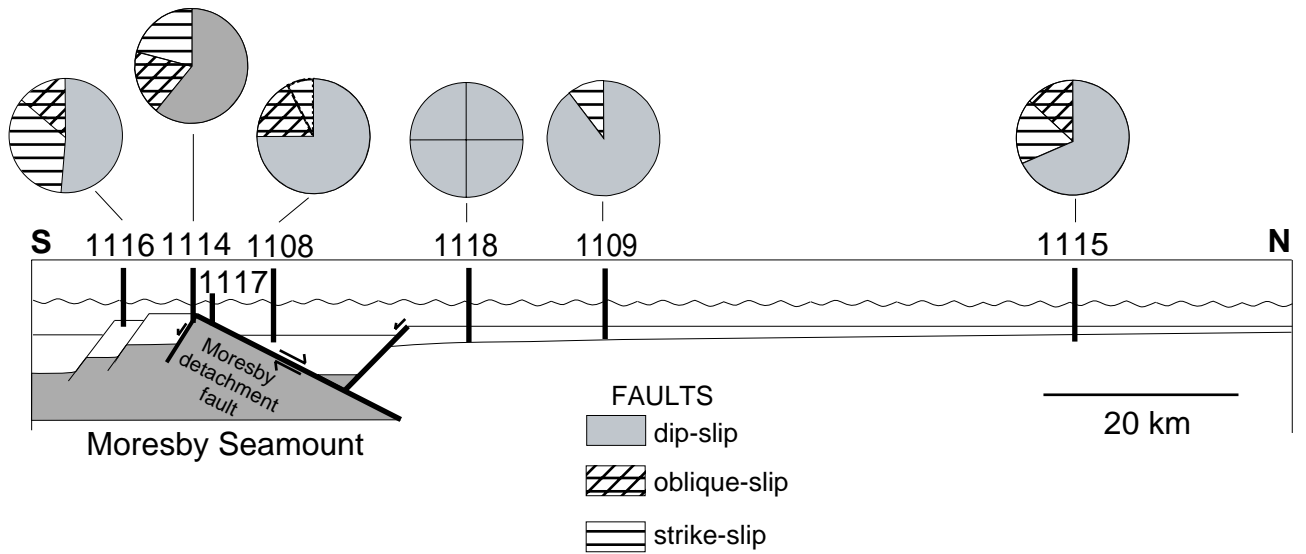
Figure F34. Estimated thermal gradients (in °C·km^{-1}) from Leg 180. Confidence in data is discussed in "Thermal Gradients," p. 24.
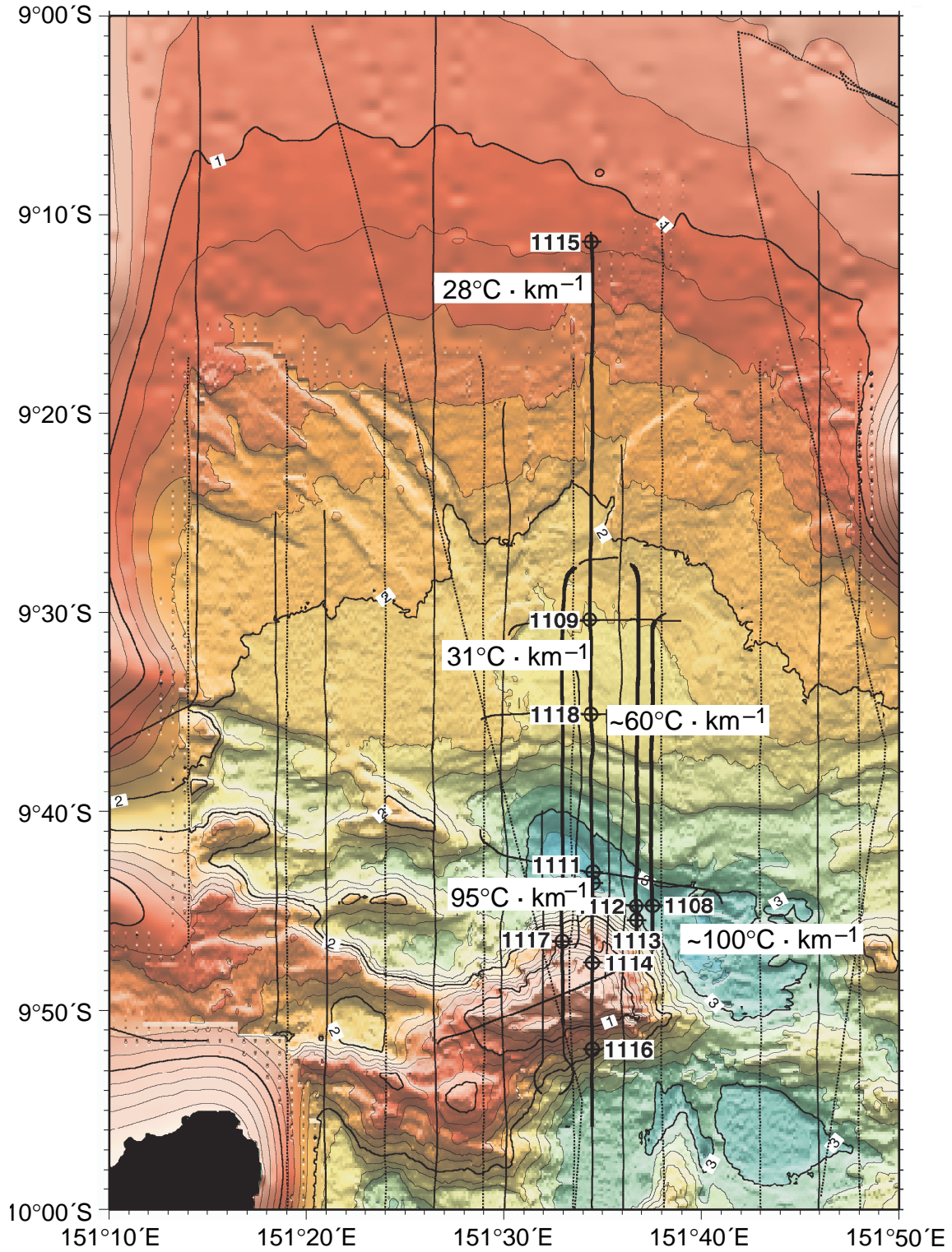
Figure F35. Natural gamma ray from the triple-combo runs in Holes 1114A, 1118A, 1109D, and 1115C.
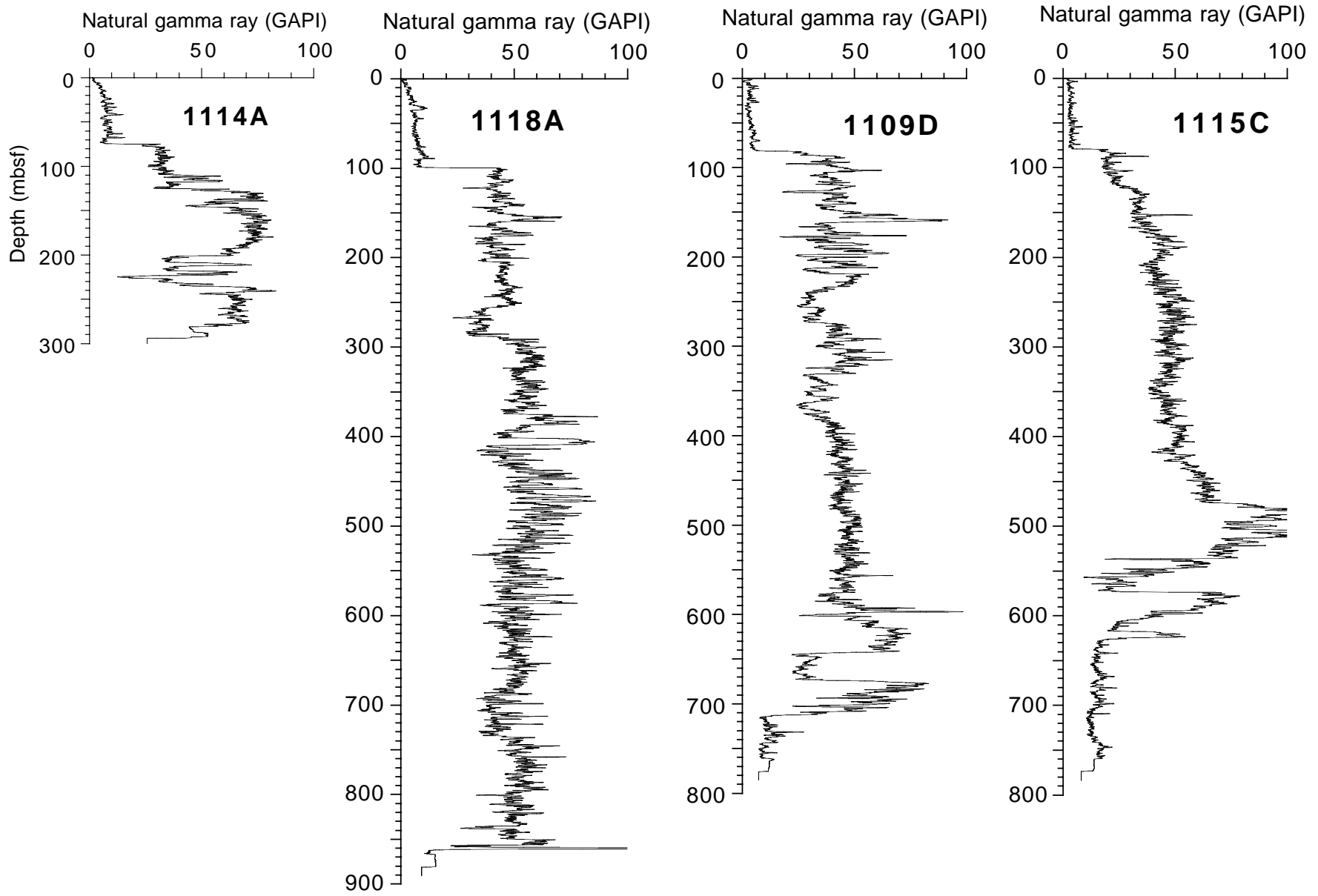
Figure F36. Neutron porosity and density porosity from the triple-combo runs in Holes 1114A, 1118A, 1109D, and 1115C.
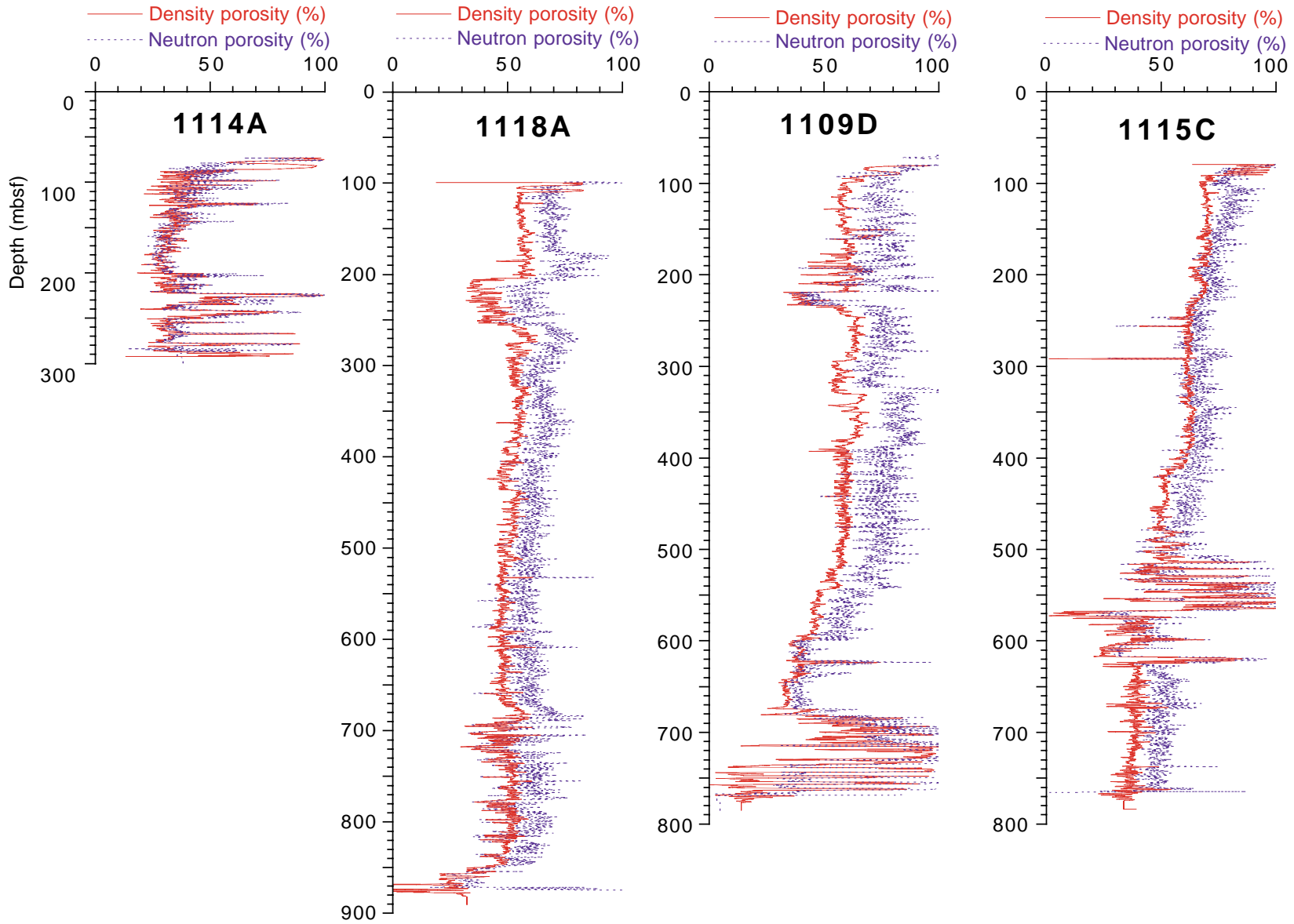
Figure F37. Photoelectric effect (PEFL) from the triple-combo runs in Holes 1114A, 1118A, 1109D, and 1115C.
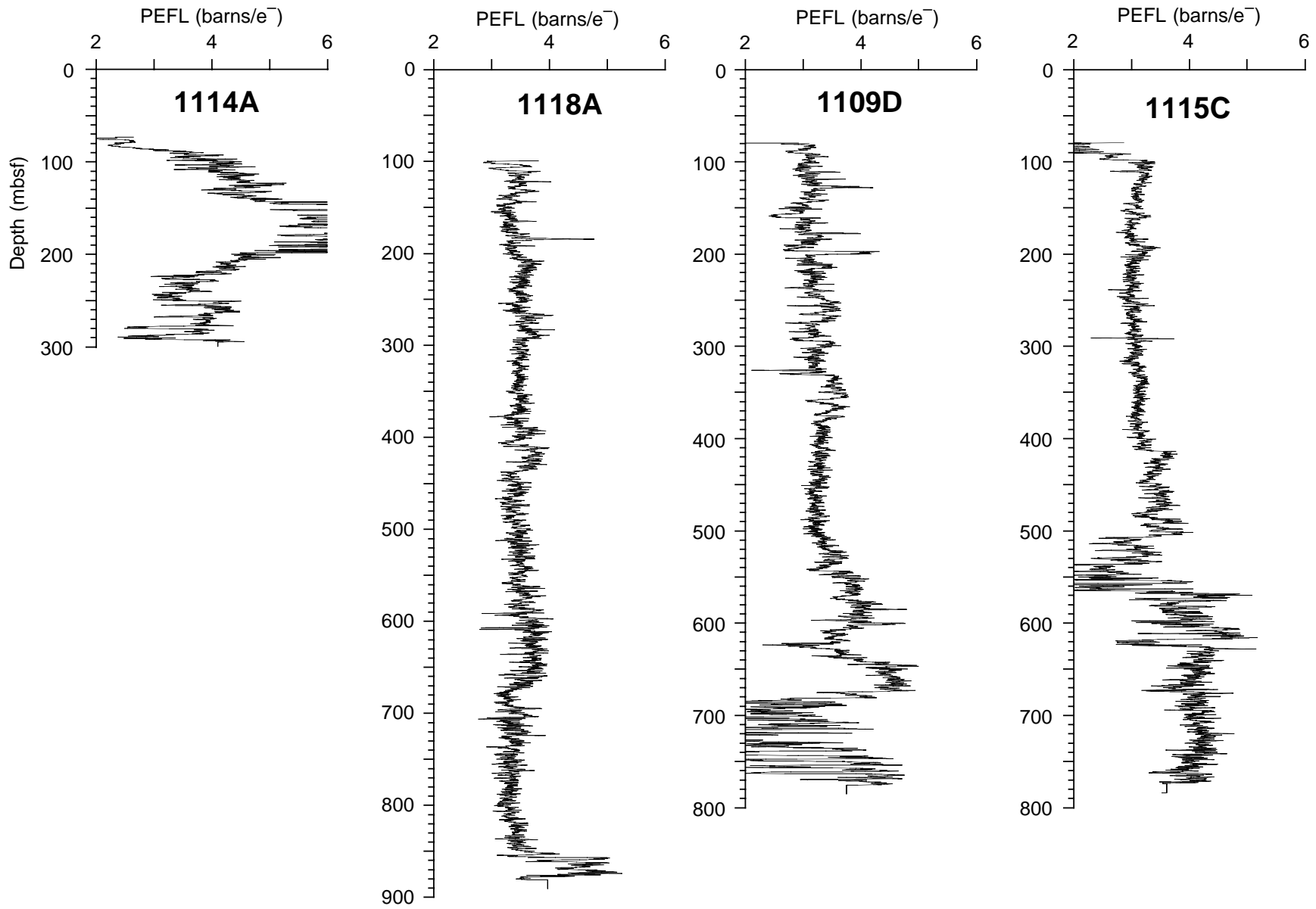
Figure F38. Sonic velocity (V_p) from the array sonic tool in Holes 1114A, 1118A, 1109D, and 1115C.
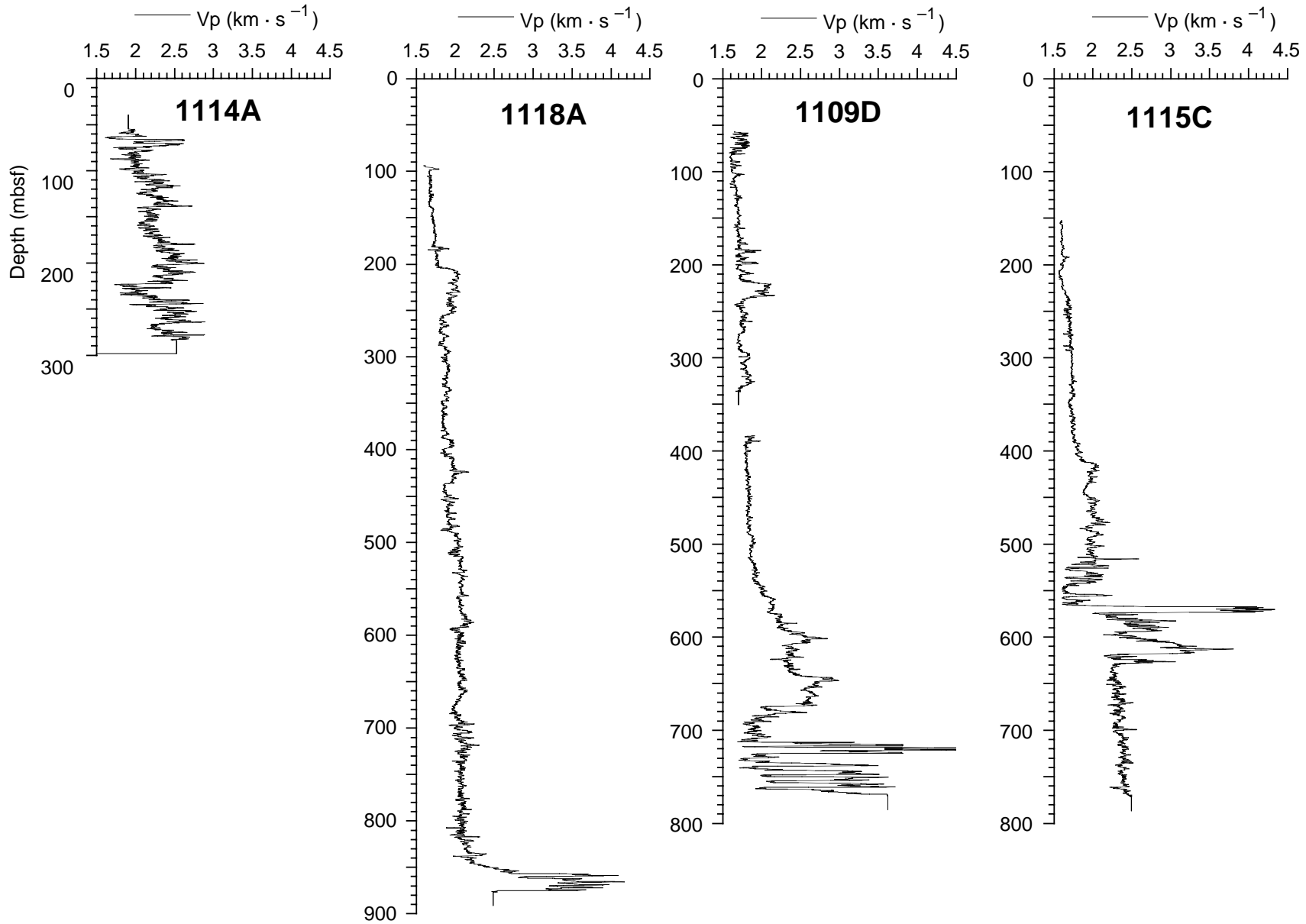
Figure F39. This dynamically normalized, double pass FMS image from Site 1115 shows well-defined, flat-lying, conductive clayey layers interbedded with thin (~10 cm), resistive sandy or carbonate-rich beds. Horizontal beds are characteristic of the stratigraphy observed in FMS images from each of the three northern sites (1109, 1115, and 1118). The vertical gray (green) lines mark the Pad 1 azimuth trace of each FMS pass. The FMS images are oriented from 0° to 360° from geographic north.

Figure F40. Statically normalized FMS image (left) and tadpole plot (right) from Site 1114. Sinusoidal fit to dipping beds (dashed) and fractures (solid) are used to measure dips and dip directions, which are shown on the tadpole plot. Dominant bed dips are ~30° oriented northwest, whereas dominant fracture dips are ~50° to ~60° oriented north within the same interval.

Table T1. Leg 180 drill-site locations and coring totals.

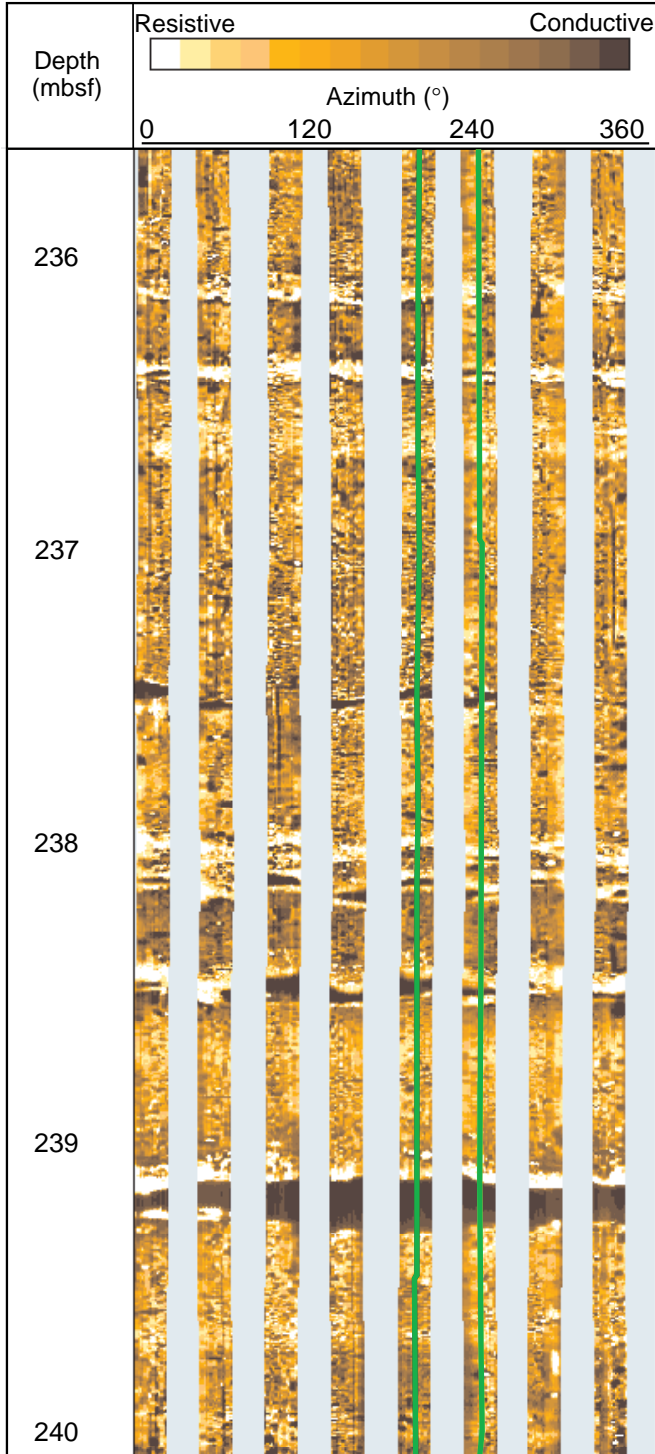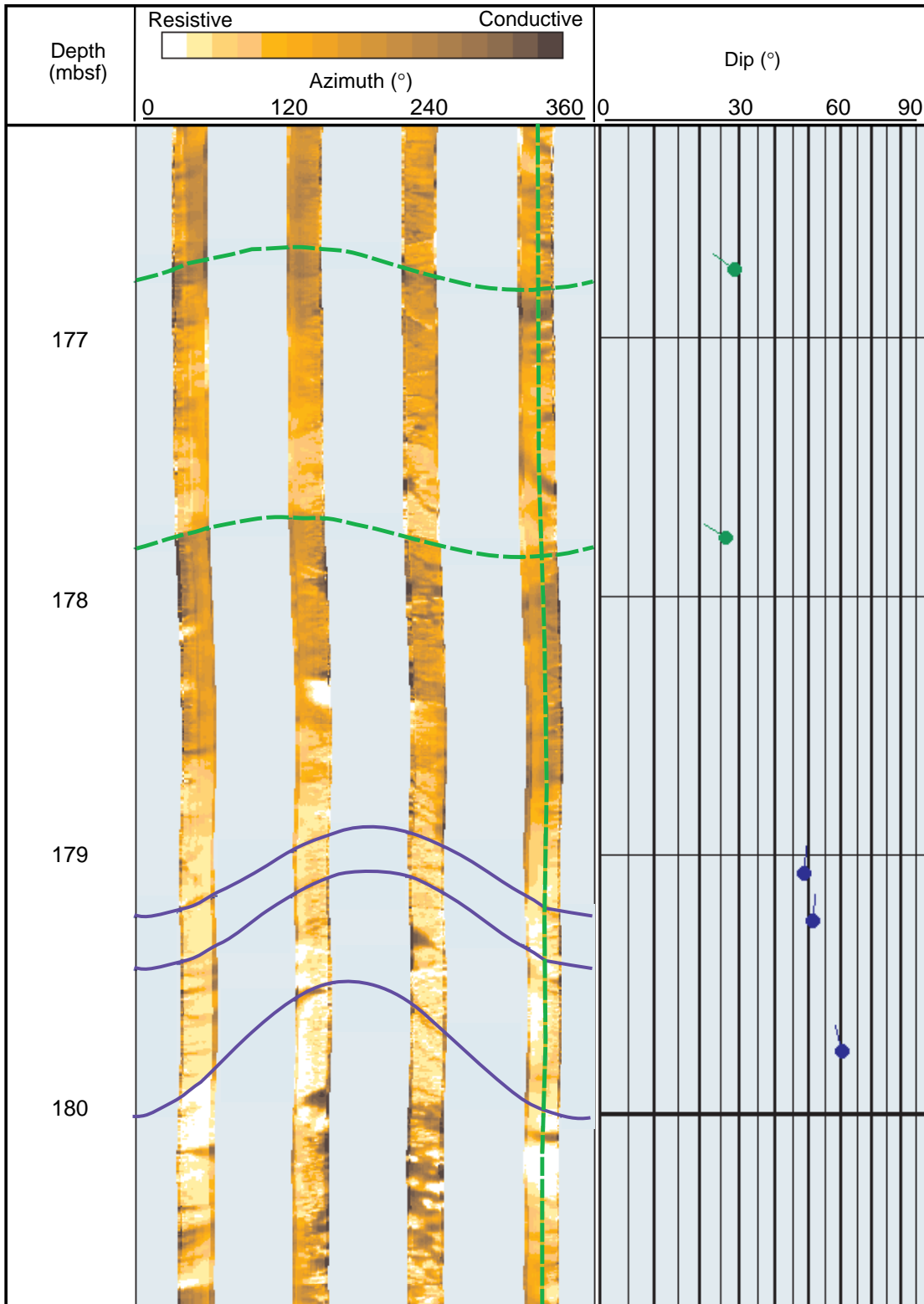| Hole	Latitude	Longitude	Water depth (mbsl)	Number of cores	Interval cored (m)	Core recovered (m)	Total recovered (%)	Drilled without coring (m)	Total penetration (mbsf)	Time on hole (days)
1108A	09°44.708′S	151°37.514′E	3162.7	NA	NA	NA	NA	16.3	16.3	0.6
1108B	09°44.724′S	151°37.543′E	3177.2	51	485.2	148.58	30.6	0.0	485.2	6.8
Site 1108 totals:				51	485.2	148.58	30.6	16.3	501.5	7.4
1109A	09°30.390′S	151°34.388′E	2210.9	1	9.5	9.96	104.8	0.0	9.5	0.3
1109B	09°30.396′S	151°34.391′E	2211.1	2	14.8	15.14	102.3	0.0	14.8	0.1
1109C	09°30.392′S	151°34.390′E	2211.0	41	375.7	323.11	86.0	0.0	375.7	2.6
1109D	09°30.380′S	151°34.355′E	2211.0	51	449.2	299.87	66.8	352.8	802.0	6.0
Site 1109 totals:				95	849.2	648.08	76.3	352.8	1202.0	9.0
1110A	09°43.599′S	151°34.511′E	3246.4	2	9.5	9.50	100.0	0.0	9.5	0.4
1110B	09°43.609′S	151°34.509′E	3246.3	3	22.3	5.37	24.1	0.0	22.3	0.5
1110C	09°43.599′S	151°34.498′E	3245.8	0	0.0	0.00	NA	15.0	15.0	0.6
1110D	09°43.588′S	151°34.526′E	3245.8	1	6.0	0.10	1.7	22.7	28.7	0.2
Site 1110 totals:				6	37.8	14.97	39.6	37.7	75.5	1.7
1111A	09°43.059′S	151°34.533′E	3200.7	18	173.7	15.19	8.7	0.0	173.7	1.4
Site 1111 totals:				18	173.7	15.19	8.7	0.0	173.7	1.4
1112A	09°44.749′S	151°36.721′E	3046.7	14	122.4	5.85	4.8	0.0	122.4	2.0
1112B	09°44.746′S	151°36.714′E	3046.6	4	38.5	1.49	3.9	126.1	164.6	
Site 1112 totals:				18	160.9	7.04	4.4	126.1	287.0	2.4
1113A	09°45.449′S	151°36.737′E	2915.6	3	25.2	0.44	1.7	0.0	25.2	1.3
Site 1113 totals:				3	25.2	0.44	1.7	0.0	25.2	1.3
1114A	09°47.613′S	151°34.504′E	406.5	37	352.8	43.78	12.4	0.0	352.8	3.5
Site 1114 totals:				37	352.8	43.78	12.4	0.0	352.8	3.5
1115A	09°11.389′S	151°34.450′E	1149.6	1	4.4	4.43	100.7	0.0	4.4	0.1
1115B	09°11.382′S	151°34.437′E	1148.8	31	293.1	286.84	97.9	0.0	293.1	1.0
1115C	09°11.383′S	151°34.422′E	1148.7	54	519.3	291.63	56.2	283.2	802.5	5.3
Site 1115 totals:				86	816.8	582.90	71.4	283.2	1100.0	6.4
1116A	09°51.934′S	151°34.508′E	1851.3	18	158.9	32.61	20.5	0.0	158.9	3.3
Site 1116 totals:				18	158.9	32.61	20.5	0.0	158.9	3.3
1117A	09°46.526′S	151°32.945′E	1163.2	14	111.1	6.42	5.8	0.0	111.1	1.7
1117B	09°46.527′S	151°32.951′E	1163.2	1.0	9.5	0.05	0.5	0.0	9.5	0.2
1117C	09°46.520′S	151°32.943′E	1163.2	1.0	9.5	1.05	11.1	0.0	9.5	0.3
Site 1117 totals:				16	130.1	6.57	5.0	0.0	130.1	2.2
1118A	09°35.110′S	151°34.421′E	2303.6	76	721.6	466.21	64.6	205.0	926.6	7.6
Site 1118 totals:				76	721.6	466.21	64.6	205.0	926.6	7.6
Leg 180 totals:				424	3912.2	1966.37	50.3	1021.1	4933.3	48.1

Notes: NA = not applicable. Sediment recovered in wash core barrels from intervals drilled without coring are not included in hole or site totals.

Table T2. Thickness of removed sediment at Sites 1108, 1114, and 1116, as estimated from exponential curves (Athy, 1930) and use of porosity data, Sites 1109, 1111, 1115, and 1118 for reference.

	Site 1108	Site 1114	Site 1116
Thickness of removed sediment, as calculated from exponential least-squares function (m):	~400	~220 to >400	~960
Thickness of removed sediment, as estimated from Leg 180 "reference sites" (m):	500–700	750	1000

Table T3. Leg 180 logged intervals in meters below seafloor.

Tool string		Hole 1108B	Hole 1109D	Hole 1114A	Hole 1115C	Hole 1118A
Triple combo						
In pipe	Top:	−20	−68	−27	−38	−67
	Bottom:	98	82	75	80	100
Open hole	Top:	98	82	75	80	100
	Bottom:	165	786	305	784	891
FMS-sonic						
In pipe	Top:			39	42	67
	Bottom:			75	80	98
Open hole	Top:		82	75	80	98
	Bottom:		351	298	787	892
In pipe	Top:		376			
	Bottom:		385			
Open hole	Top:		385			
	Bottom:		786			